Ultraminiature Piezoelectric Implantable Acoustic Transducers for Biomedical Applications

by

Chuming Zhao

A dissertation submitted in partial fulfillment
of the requirements for the degree of
Doctor of Philosophy
(Mechanical Engineering)
in The University of Michigan
2018

Doctoral Committee:

Professor Karl Grosh, Chair
Professor Yogesh Gianchandani
Associate Professor Kenn Oldham
Professor Bryan E. Pfingst
Professor Yehoash Raphael

Chuming Zhao

chumingz@umich.edu

ORCID iD: 0000-0001-8104-5902

To my family.

ACKNOWLEDGEMENTS

I would like to express my most sincere gratitude my advisor, Prof. Karl Grosh for his patience, guidance, and support throughout my PhD process. Karl has been a wonderful mentor and role model, and I've learned so much from him. I would also like to thank my committee members, Prof. Yogesh Gianchandani, Prof. Kenn Oldham, Prof. Bryan Pfingst, and Prof. Yehoash Raphael for their help and advice. I especially want to thank Prof. Pfingst and Prof. Raphael who were instrumental in the intracochlear sensors project from the beginning. I also want to thank the staff at the Kresge Hearing Research Institute, particularly Debbie Colesa, Karin Halsey, Chris Ellinger, and Lisa Kabara, for their guidance and expertise in performing the *in vivo* experiments. I would further like to acknowledge Prof. Khalil Najafi, Prof. David Dowling, Prof. Bogdan Popa, and Prof. Katuo Kurabayashi for the use of their lab instruments.

I want to thank all of the friends and staff in the Lurie Nanofabrication Facility (LNF), especially Katharine Beach, Kevin Owen, Pilar Herrera-Fierro, Rob Hower, Nadine Wang, Terre Briggs, Matt Oonk, Brian Armstrong, David Sebastian, and Tony Sebastian for all of their help and patience with my fabrication process. My conversations with students and staff in the LNF have helped me greatly throughout all these years, and I am grateful for the opportunity to work in the LNF.

I would like to thank Dr. Lichuan Ping from MAX BioE Inc. for his help and strong support to the diaphragm transducer project. It has been a wonderful experience to work with him. I also want to thank Dr. Robert Littrell and Dr. Wang-Kyung

Sung from Vesper Technologies for their help on the MEMS design and fabrication. I also want to thank the financial support from the Wright State University Foundation, the University of Michigan Center for Organogenesis, the University of Michigan MCubed grant program, and NIH grant P30 DC 005188.

I want to thank Katherine Knisely for her help, especially in the early stage of my PhD. I also want to thank my labmates in the Acoustic and Vibrations lab, Xiaochen Zhao, Alison Hake, Nate Geib, Aritra Salsma, Amir Nankali, Jongsoo Choi, Jinhong Qu, Yi Chen, Kendall Teichert, Mayur Birla, Lu Wang, Yuxin Zhai, Hung-suk Kwon, and Yeonjoon Cheong. I want to thank all my friends, past and present, who helped me through my PhD process.

Finally, I would like to thank my Mom and Dad for their boundless love for all my life. I could not have gone this far without their unconditional support.

TABLE OF CONTENTS

LIST OF FIGURES

Figure

LIST OF TABLES

Table

LIST OF ABBREVIATIONS

ABM artificial basilar membrane

FEA finite element analysis

AlN aluminum nitride

DRIE deep reactive ion etching

MEMS microelectromechanical systems

fPCB flexible printed circuit board

SPL sound pressure level

CI cochlear implant

DC direct current

PIAT piezoelectric implantable acoustic transducer

FICI fully implantable cochlear implant

CICI completely implantable cochlear implant

BHF buffered hydrofluoric acid

XRD X-ray diffraction

FWHM full width half maximum

TIKI totally implantable cochlear implant

IRN input referred noise

MDP minimal detectable pressure

CM cochlear microphonic

ABR auditory brainstem response

EABR electrically evoked auditory brain stem response

RF radio frequency

ASIC application-specific integrated circuit

LNF Lurie Nanofabrication Facility

LDV laser Doppler vibrometer

FOM figure of merit

ST scala tympani

SV scala vestibule

ABSTRACT

Miniature piezoelectric acoustic transducers have been developed for numerous applications. Compared to other transduction mechanisms like capacitive or piezoresistive, piezoelectric transducers do not need direct current (DC) bias voltage and can work directly exposed to fluid. Hence, they are good candidates for biomedical applications that often require the transducer to work in water based fluid. Among all piezoelectric materials, aluminum nitride (AlN) is a great choice for implantable sensors because of the high electrical resistance, low dielectric loss, and biocompatibility for *in vivo* study. This thesis presents the design, modeling, fabrication, and testing of the AlN acoustic transducers, miniaturized to be implantable for biomedical applications like hearing or cardiovascular devices.

To design and model the transducer in air and in water, a 3D finite element analysis (FEA) model was built to study the transducer in a viscous fluid environment. An array of AlN bimorph cantilevers were designed to create a multi-resonance transducer to increase the sensitivity in a broad band frequency range. A two-wafer process using microelectricalmechanical systems (MEMS) techniques was used to fabricate the xylophone transducer with flexible cable. Benchtop testing confirmed the transducer functionality and verified the FEA model experimentally.

The transducer was then implanted inside a living cochlea of a guinea pig and tested *in vivo*. The piezoelectric voltage output from the transducer was measured in response to 80-95 dB sound pressure level (SPL) sinusoidal excitation spanning 1-14 kHz. The phases showed clear acoustic delay. The measured voltage responses were linear and above the noise level. These results demonstrated that the transducer can

work as a sensor for a fully implantable cochlear implant.

The second generation device, an ultraminiature diaphragm transducer, was designed to be smaller, and yet with an even lower noise floor. The transducer was designed and optimized using a 2D axial-symmetric FEA model for a better figure of merit (FOM), which considered both minimal detectable pressure (MDP) and the diaphragm area. The low-frequency sensitivity was increased significantly, because of the encapsulated back cavity. Because of this merit, cardiovascular applications, which focus on low frequency signals, were also investigated. The diaphragm transducers were fabricated using MEMS techniques. Benchtop tests for both actuating and sensing confirmed the transducer functionality, and verified the design and model experimentally. The transducer had a better FOM than other existing piezoelectric diaphragm transducers, and it had a much lower MDP than the other intracochlear acoustic sensors.

CHAPTER I

Introduction

Acoustic transducers have been used widely in our life to provide an important interface between human and machine [1, 2, 3, 4, 5]. Billions of microphones and speakers are manufactured every year. With the recent development in micro fabrication, especially in microelectromechanical systems (MEMS), acoustic transducers are miniaturized to produce high performances while having a small form factor. This advances in the acoustic transducers have created many commercial successes in consumer electronics and breakthroughs in the development of biomedical devices. The miniaturization and the improvement in the device performance even enables the devices to be implanted inside the body, which opens up many more possibilities. This work aims to develop ultraminiature implantable acoustic transducers for biomedical applications. Such applications often require transducers to work in a fluid environment. Hence, piezoelectric transduction offers the unique advantages over capacitive or pieozoresistive transduction because it does not need direct current (DC) bias voltage and can work directly exposed to fluid. Among all piezoelectric materials, aluminum nitride (AlN) is a great choice for implantable sensors because of the high electrical resistance, low dielectric loss, and biocompatibility for *in vivo* study.

This thesis presents the design, modeling, fabrication, and testing of the AlN acoustic transducers, miniaturized to be implantable for biomedical applications, like

hearing and cardiovascular devices.

1.1 Cochlear Implants

According to estimates from the World Health Organization, 360 million people in the world had impaired hearing, as of 2011[6]. The cochlear implant (CI) provides an effective therapeutic solution for treating sensorineural hearing loss. As shown in Figure 1.1, most commercially available CIs have an external microphone/processing unit, a radio frequency (RF) inductive link, and intracochlear electrodes. Although the CIs enable speech recognition, they have major limitations including high cost, high power consumption (20-40 mW), cosmetic concerns, and safety issues associated with the external processing unit [7, 8, 9]. These limitations contribute to an international market penetration for CIs of approximately 0.7% [10]. The development of a fully implantable cochlear implant is attractive, because it would improve cosmetic and safety issues. Unlike the traditional CI, where external components must be removed for many activities including sleep and showering [11], a fully implantable CI could remain on at all times. Additionally, a fully implantable cochlear implant would eliminate the inductive link between the processor and CI electrode that causes 60% of the power drop [7] in the device, reducing power consumption [9].

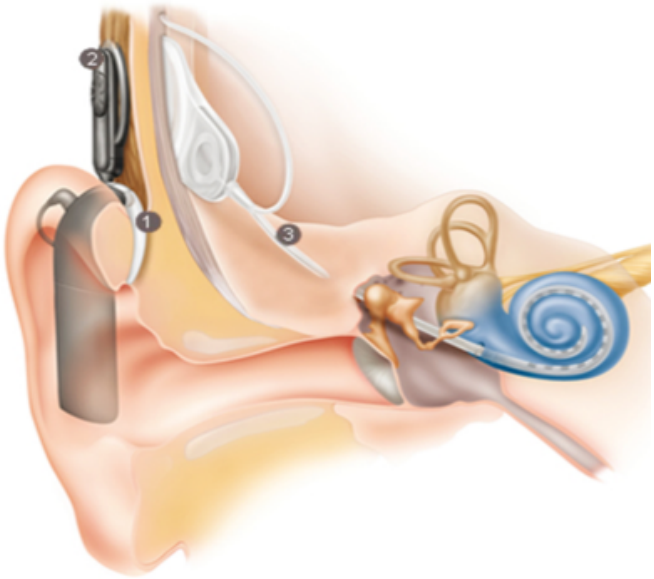

Figure 1.1: A typical traditional cochlear implant system, which contains (1) a microphone and a processor in the external unit behind the ear, (2) a RF link, and (3) an implanted electrode array. (www.cochlear.com).

There have been several attempts to build fully implantable cochlear implants [12, 13, 14, 15, 16, 17]. As summarized in Figure 1.2 [18], each FICI requires an internal microphone of some kind. For instance, Cochlear Corporation developed the totally implantable cochlear implant (TIKI), which used a subcutaneous microphone. In a clinical study of this device [15], subjects reported benefits from TIKI and had continued to use it on a daily basis because of cosmetic advantages and the ability to hear while showering, sleeping, and doing physical work. However, speech perception results were significantly lower when compared with the traditional CI because of the reduced sensitivity and increased body noise contamination of the subcutaneous microphone. The state of the art for implantable acoustic sensors for hearing devices is well-reviewed in [18] where they also present a trans-tympanic microphone to measure ear canal pressure for hearing aids or cochlear implants. This approach, while promising, also faces issues such as ventilation tube migration and liquid contamina-

tion which would reduce the effectiveness of the device [18].

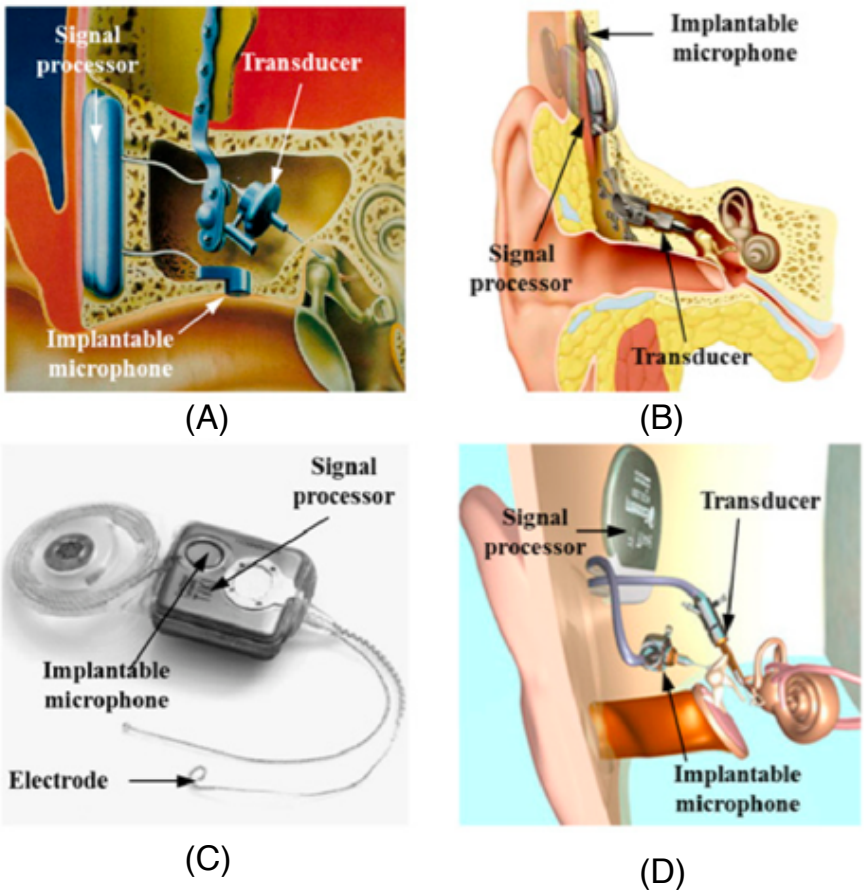

Figure 1.2: The fully implantable cochlear implants [18]. (A) TICA (Implex, Munich, Germany) [19]; (B) Carina (Cochlear, Sydney, Australia) [16]; (C) TIKI (Cochlear, Sydney, Australia) [15]; (D) Esteem (Envoy, Saint Paul, MN, USA) [16].

1.2 Implantable Acoustic Transducers

An intracochlear transducer is an attractive alternative for patients with a functioning middle ear, because the intracochlear acoustic pressure is typically higher than the ear canal pressure [20, 21, 22, 23]. Olson[20], using a fiber-optic probe with a polymer-gold membrane, and Dancer and Franke [23], using a Kulite piezoresistive

sensor coupled to a small silicone-filled probe tube, successfully measured the fluctuating pressures inside a living cochlea. These measurements serve as a reference for the pressures measured in the current study, although neither of these systems is robust or small enough for chronic use. The implantable acoustic transducer is miniaturized to fit in the scala tympani (ST) or scala vestibule (SV) in a cochlea, and it needs to be able to function in a fluid based environment, because the cochlea is filled with fluid. Creighton et al.[24] and Pfiffner et al.[25] implanted a miniature microphone in the cadaveric human temporal bone and measured intracochlear sound pressure in vitro. Recently a PVDF-based intracochlear microphone prototype was developed and used to measure sound in a living gerbil cochlea[26]. In the current study, we present the design and testing of an AlN MEMS implantable acoustic transducer, which we used in a living guinea pig to sense the voltage response due to external acoustic excitation.

1.3 Artificial Basilar Membrane

In part, our efforts to build the implantable transducer were informed by research on the piezoelectric artificial basilar membrane (ABM). Recent development of microfabrication techniques enabled the development of the life scale ABM models [27, 28, 29, 30] with tonotopicity (place-to-frequency mapping). Shintaku et al.[31] fabricated a piezoelectric ABM that had a frequency selective electrical response to acoustic stimuli. This transducer was then used as the *ex vivo* (external) front end of a cochlear implant to evoke auditory brain-stem responses[32]. In the same paper[32], these investigators fitted a piezoelectric transducer into an excised cochlea and measured the plate vibration in response to stapes excitation using an external laser vibrometer. Such an approach could not be applied to an *in vivo* experiment due to the use of the laser vibrometer and the large fenestra required for inserting the piezoelectric plate. A different approach to making an artificial cochlea is the

development of xylophone-like structures with arrays of cantilevers which resonate at different frequencies[33, 34, 35]. Jang, et al.[36, 37] coupled an *ex vivo* MEMS piezoelectric cantilever array transducer to signal processing hardware which generated biphasic current pulses. The output was connected to a deafened animal via a cochlear implant electrode array to successfully evoke auditory brainstem responses.

1.4 Cardiovascular Pressure Sensors

The ability to measure pressure in the living body is crucial in the biomedical applications and healthcare products, including cardiovascular and urologic diagnostic procedures, surgical procedures and hearing devices [38]. Intracardiac pressure sensor, in particular, is an interesting research topic because it is an important front end of the treatment of heart failures, which 23 million people worldwide are suffering from [39]. Most devices use catheters/fibers coupled to an external pressure transducer [40, 41]. The transducer itself is often bulky and not implantable, which hinders continuous chronic pressure monitoring. Recent studies on MEMS have enabled implantable piezoeresistive pressure sensors to be designed and optimized [42]. Some animal tests were also done using MEMS pressure sensors [43, 44]. Most recently, Zhao et al. [45] presented a MEMS implantable piezoelectric pressure sensor which sensed intracochlear pressure. Based on the technology, this study aims to further enhance the sensor and broaden the application by introducing a miniaturized high performance implantable piezoelectric pressure sensor. Compared with piezoresistive pressure sensor, this dynamic pressure sensor has the advantages of low noise, low power consumption, biocompatible and no DC bias requirement.

1.5 Thesis Overview

This thesis focuses on the design, model, fabrication, and testing of the ultra-miniature piezoelectric acoustic transducer for biomedical applications like hearing and cardiovascular applications. A brief overview of each chapter is described below.

Chapter 2 presents a multi-resonant xylophone acoustic transducer using AlN bimorph with a flexible parylene-gold cable connection. A two wafer fabrication process and a wire-epoxy bonding technique are introduced, which reduces the fabrication time and increases the yield. A finite element analysis (FEA) model is developed to study the frequency behavior for the piezoelectric cantilever transducer in a viscous fluid media, and this model can accurately predict the frequency response both in air and in water.

Chapter 3 shows an *in vivo* animal study using a piezoelectric implantable acoustic transducer (PIAT) (the xylophone transducer with Al_2O_3 and parylene coating). The PIAT was implanted in a living cochlea of a guinea pig. Piezoelectric voltage output in response to external acoustic stimuli is measured while the PIAT is implanted, which demonstrates the feasibility of using the transducer as a sensor for the fully implantable cochlear implants.

Chapter 4 demonstrates the second generation of the implantable acoustic transducer, a AlN unimorph diaphragm with a encapsulated back cavity. This diaphragm transducer has a much better low frequency performance. Hence, cardiovascular applications, which focus more on low frequency signals, are also investigated. This diaphragm transducer is smaller but with a higher figure of merit (FOM) than existing piezoelectric diaphragm sensors. It is smaller than the first generation device and other existing intracochlear acoustic sensors, but it has the lowest minimal detectable pressure (MDP).

Chapter 5 summaries the thesis and highlights the details about the contributions of this work.

CHAPTER II

AlN MEMS Multichannel Xylophone Transducer with Flexible Ribbon Cable Connection

In this chapter, we demonstrated a miniature multichannel xylophone transducer with flexible connection using piezoelectric material AlN. Miniature transducers have been developed using MEMS techniques. Some transducers, like microphones [46] or accelerometers [47], are designed to operate equally sensitive in the desired frequency range, resulting in an accurate representation of the original signal. Some other transducers like microspeakers [48, 49] or energy harvesters [50] have one or multiple resonances in the desired frequency band to enhance sensitivity and transduction efficiency. This multi-resonant transduction characteristic is also found in the cochlea, a naturally designed acoustic transducer [51]. Inside the cochlea, there is a structurally varying basilar membrane that resonances differently at different location, which creates an enhanced sensitivity over a broad frequency range [52].

In order to design and analyze such a transducer that often operates in a fluidic environment, a model is necessary to study the frequency behavior of the transducer. While the frequency response of a cantilever in vacuum can be easily solved by the Euler-Bernoulli equation [53], the response in a viscous fluid is relatively harder. Still, several authors have developed techniques to predict the response of cantilevers with rectangular cross-sections vibrating in viscous fluids analytically [54, 55, 56,

57]. The three-dimensional FEA models were developed to study the dynamics of a microcantilever in air [58] and in a viscous fluid [59], providing a direction to study the frequency behavior of cantilever underwater. Recently an FEA model for cantilever based piezoelectric transducer working both in air and underwater was developed [60], providing a direct link from electric signal to acoustic or vibration signals for transducers design.

In this chapter, we propose a method for the design and fabrication of a MEMS piezoelectric xylophone transducer with integrated flexible connection. The transducer is a miniaturized multi-resonance device that works in air and underwater. AlN was chosen as the piezoelectric material for this work because the low dielectric loss, compatibility to MEMS fabrication, and biocompatibility for *in vivo* study [46, 57, 61, 62, 63]. The FEA model, validated by experimental results, is used to design the piezoelectric MEMS transducer. Some preliminary results of the miniature xylophone transducer have been presented [60]. However, the device properties were compromised due to accidental overetch which created an unsymmetrical AlN bimorph. In this chapter, we fabricated a xylophone transducer with symmetric AlN bimorph. We further fabricated a MEMS based flexible connection with electrode base and incorporated it into the xylophone transducer, which enables continuous access to the transducer signals. The functionality of the device, including the xylophone transducer and the flexible connection was verified by the actuation testing and the FEA modeling results.

2.1 Design and Modeling of the Xylophone Transducer

A CAD drawing of the piezoelectric xylophone transducer with a flexible ribbon cable connection is shown in Figure 2.1. It consists of two parts: the transducer probe (shown in the close-up) and the flexible connection with an electrode base that is used to relay *in vivo* information from the cochlea to an external site for electrical

monitoring. The probe and cable are fabricated separately and bonded afterwards, as described in the Fabrication Process section. The transducer is a xylophone structure that has four 400 μm wide cantilevers with lengths that span 200-245 μm, spaced 100 μm apart. The lengths are chosen to tune the fluid-loaded resonances to be in the range of 20 - 40 kHz, the best frequencies of the basal turn of the guinea pig cochlea [64, 65], where the probe is designed to be implanted. The cantilevers are suspended along an etched silicon backbone that defines the structure of the probe. Each beam is a bimorph cantilever, consisting of two 1.5 μm thick AlN layers laminated by three 15/30 nm thick Ti/Pt electrode layers. The traces on the transducer are 20 μm wide in the implantable part (first 4 mm from the tip) and are widened to 40 μm in the base of shank, and extended to the bonding pads (100 μm wide and 300 μm long). A separate ribbon cable (see Figure 2.1) has 10 μm gold electrical traces spaced 200 μm laterally. At the end of each trace, there is a donut shaped pad with an inner diameter of 50 μm and outer diameter of 100 μm for bonding. The traces are encased in parylene and they extend 5 cm to an integrated electrode base that has larger pads for interfacing with external electrical monitoring equipment.

An FEA model using COMSOL Multiphysics 5.2a [66] was built to model the frequency behavior of the cantilever in air or water. The model calculated the deflection of the beam under voltage excitation while interacting with surrounding viscous fluid. Thermoacoustic, pressure acoustic, solid mechanics, and electrostatics modules were used for this model. The material properties (tabulated in Table 2.1) used for the AlN, air, and water were taken from COMSOL Material Library [66], except for the piezoelectric coupling coefficient d_{31} which was measured, as explained in the experimental method section. The length of each beam used in the model was modified by no more than 5% of the lengths as designed to fit the measured resonance measured in air to compensate for an undercut of up to 12 μm that occurred during the etching of the Si backbone, producing a variation in the fabricated cantilever lengths

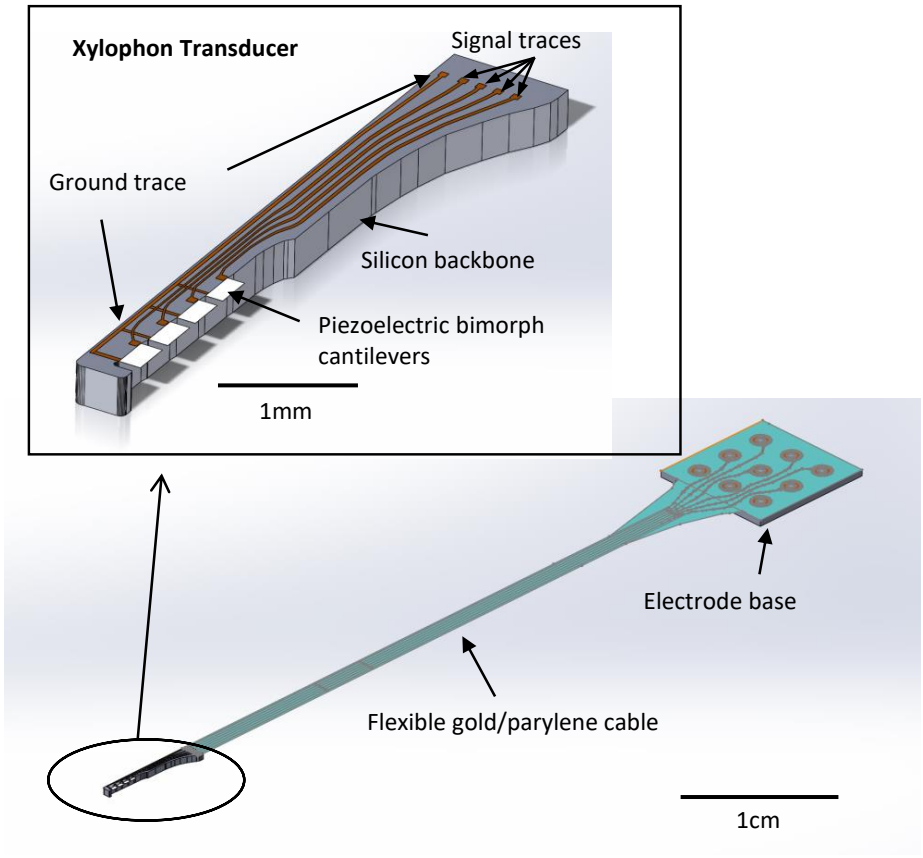

Figure 2.1: A 3D drawing of the piezoelectric xylophone transducer with the flexible parylene gold connection. The inset shows the details of the xylophone transducer.

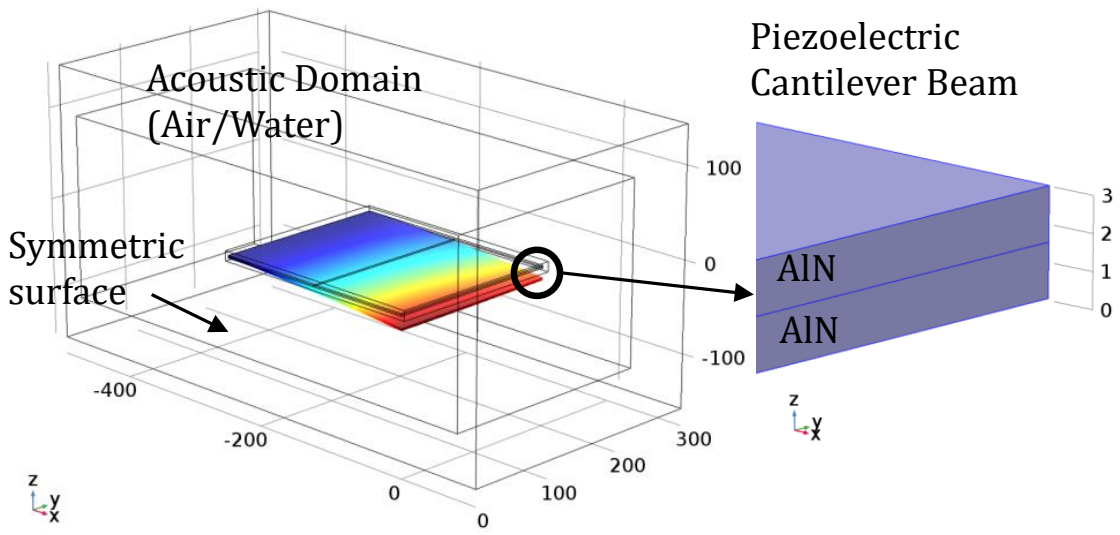

Figure 2.2: The modeling setup with a close-up shows the piezoelectric cantilever beam.

as compared to the lithographically defined cantilever lengths. These lengths (shown in Table 2.2) were maintained in the fluid-loaded model. The structural damping coefficient η_s was the dominant damping source in air. The η_s of each beam was chosen to fit the measured Q from actuation response (where the $Q = \frac{f_r}{\Delta f}$), f_r is the cantilever resonant frequency, and Δf is the full width at half maximum). While model parameters were fit to match the in-air response, no parameter adjustment is performed underwater other than changing the fluid material parameters from air to water. Figure 2.2 shows the geometry of the model setup, which consists of a piezoelectric cantilever beam in a viscous fluid (air or water). The close-up in Figure 2.2 shows the AlN bimorph with the thickness of Ti/Pt electrode layer neglected. Tetrahedral elements were used and refined near the beam. To maintain the accuracy of numerical computation, the mesh size around the cantilever beam was set to be 2 μm to ensure it was smaller than the viscous boundary layer $\delta_\nu = \sqrt{\frac{2\nu}{\omega}}$ (where ν is the kinematic viscosity of the fluid, and ω is the angular frequency). The mesh coarsened away from the beam.

Subject	Description	Parameter	Value
AlN	Density	ρ	3300 kg/m^3
	Compliance	s_{11}	2.86 x 10^{-12} m^2/N
	Relative permitivity	ϵ_r	10.26
	Piezoelectric coefficient	d_{31}	-1.9 pm/V
Air	Density	ρ	1.23 kg/m^3
	Dynamic viscosity	μ	1.82 x 10^{-5}Pa·s
	Speed of sound	c	343 m/s
Water	Density	ρ	1000 kg/m^3
	Dynamic viscosity	μ	1.82 x 10^{-5}Pa·s
	Speed of sound	c	1481 m/s

Table 2.1: Material properties of the FEA model for the cantilever in the fluid.

			Actuation in air				Actuation in Water			
			Measured		Modeled		Measured		Modeled	
	Length (μm)	Damping (η_s)	f_r (kHz)	Q	f_r (kHz)	Q	f_r (kHz)	Q	f_r (kHz)	Q
Beam 1	245	0.020	86.8	42.1	86.2	42.2	26.2	6.1	25.5	6.8
Beam 2	226	0.008	101.2	112.0	101.3	113.2	30.8	7.4	30.7	8.3
Beam 3	215	0.013	113.0	60.3	112.5	60.9	35.8	7.8	35.3	8.6
Beam 4	200	0.011	129.4	67.8	129.5	68.7	41.6	8.3	41.5	9.1

Table 2.2: Modeled and measured parameters.

2.2 Fabrication Process

The device is fabricated in the LNF with the process summarized in Figue 2.3. The fabrication process consists of three major steps, (1) xylophone transducer processing, (2) flexible connection processing, and (3) wire-epoxy bonding. Xylophone transducer processing started with a 4 inch p-type Si (100) substrate coated with 1 $\pm$ 0.1 μm of wet thermal oxide, step (1a). A five-layer stack consisting of two 1.5 μm AlN layers and three 15/30 nm Ti/Pt electrodes layers (Lab 18-2, Kurt J. Lesker Company, USA) were deposited next on the substrate, forming the bimorph cantilever transducers. The AlN layers were deposited using a dual cathode S-Gun magnetron AlN sputter tool (AMS 2004, Tegal OEM group, USA). The active area of the piezoelectric bimorph was limited to 45% of the distance from the root toward the tip of the cantilever to improve the input referred noise of the devices, as adding electrode area adds electronic noise in greater proportion than an increase in output signal [61]. In step (1b), the AlN cantilever patterning and contact to metal layers were defined using a combination of a Cl-based dry etch (9400, LAM Research Corporation, USA) and a heated (50 °C) KOH-based etch (AZ 400K, Clariant, USA). Finally, in step (1c), the top and bottom electrode layers were connected, and grounded. Sputtered Cr/Au formed the electrode pads for bonding. The probe backbone, which held the xylophone of AlN sensors, was then defined using a through-wafer deep reactive ion etching (DRIE) (STS Pegasus 4, SPTS Technologies Ltd., USA), followed by a buffered hydrofluoric acid (BHF) oxide etch to release the cantilevers.

In step (2a), the flexible parylene ribbon cable connection was fabricated in a separate wafer processing using a 20/400 nm sputtered, patterned Cr/Au layer (Lab 18-2, Kurt J. Lesker Company, USA) sandwiched between two 5 μm thick parylene layers (PDS 2035CR, Special Coating System, USA). A dry etch of the parylene layer is used to pattern the cable, as shown in step (2b). In step (2c), a DRIE was used to define the electrode base and release the cables. Next, BHF bath was used to

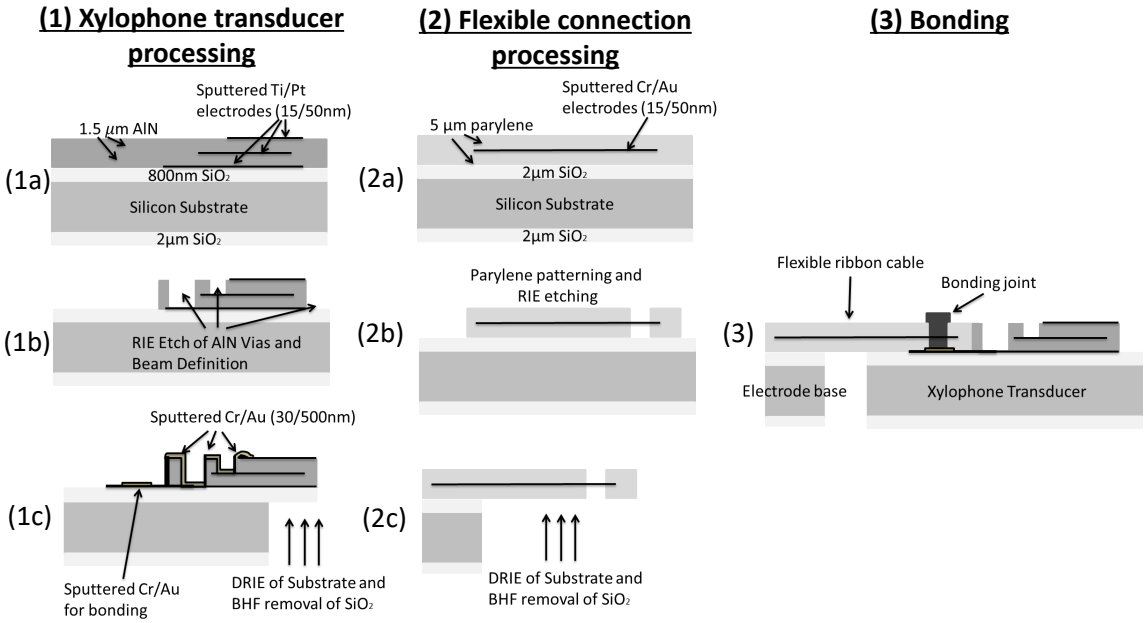

Figure 2.3: The fabrication process of the xylophone transducer with flexible connection, which consists of three major steps: (1) AlN xylophone transducer processing, (2) flexible connection processing, and (3) bonding.

release the structure. Finally, step (3) shows the bonding of the transducer and the flexible parylene cable connection, which is a challenging process. Meyer et al. [67] developed a rivet bonding process which bonds flexible ribbon cable to its desired substrate with the application of force and heating. However, when we applied this technique, the gold rivet pulled off the gold pads from the AlN layer and caused major failures. In conjunction with Protoconnect (Protoconnect LLC, MI, USA), we developed a customized wire-epoxy bonding technique specifically for the released transducer and flexible connection. Figure 2.4 shows the bonding process and the details of the bonding joints. A 25.4 μm thick Cu wire was first wire-bonded on the gold pads on the transducer as shown in Figure 2.4A. Then, the wire bonds were glued on the gold pad on the transducer using conductive epoxy (P1011, Epoxy Technology, USA), as shown in Figure 2.4B. The donut shaped pad with an inner diameter of 50 μm on the cable was aligned and put through the Cu wire, one at a time, as

shown in Figure 2.4C. Finally, conductive epoxy (P1011, Epoxy Technology, USA) was used to secure the connection, followed by nonconductive epoxy encapsulation sealing (353ND, Epoxy Technology, USA), with the silicone (Med-4011, NuSil Technology LLC, CA, USA) applied at the end for stress relief, as shown in Figure 2.4D. In this way, the process combines wire bonding and the use of conductive epoxy but does not require applying external force or heating. To simplify the bonding, three separate channels were created. The ground trace was a separate individual channel. Beams 1-2 were connected in parallel and shared a channel, while beams 3-4 were connected in parallel and shared a second signal channel.

The fabricated device is shown in Figure 2.5. A microscopic view of the xylophone transducer with four cantilever beams is shown in Figure 2.5A. The whole device with flexible cable and electrode base is shown in Figure 2.5B.

2.3 Experimental Methods

The θ-2θ and rocking curve X-ray diffraction (XRD) measurements were conducted to quantify the crystal quality of the AlN layers, using an attachment designed for full-wafer thin film XRD measurements (Ultima IV, Rigaku Corporation, Japan). The θ-2θ and rocking curve measurements were taken after the AlN depositions and the results are shown in Figure 2.6. The device impedance and dielectric loss ($\tan\delta$) were measured using a probe station (LA-150 DC, Semiprobe, USA) and an LCR meter Agilent 4284A (E4980A, Agilent, USA). Film thickness was measured using the spectroscopic reflectometer (NanoSpec 6100, Nanometrics, USA). Actuation tests were performed after the xylophone transducer was bonded with the flexible connection to show the functionality of both the transducer and the parylene-gold cable. A chirp voltage signal with an amplitude of 1V was generated using Labview 2009 controlled NI-6251 card (NI-6251, National Instruments, USA). The voltage was applied to the pads on the electrode base through tungsten needles (PTT-12/4-25,

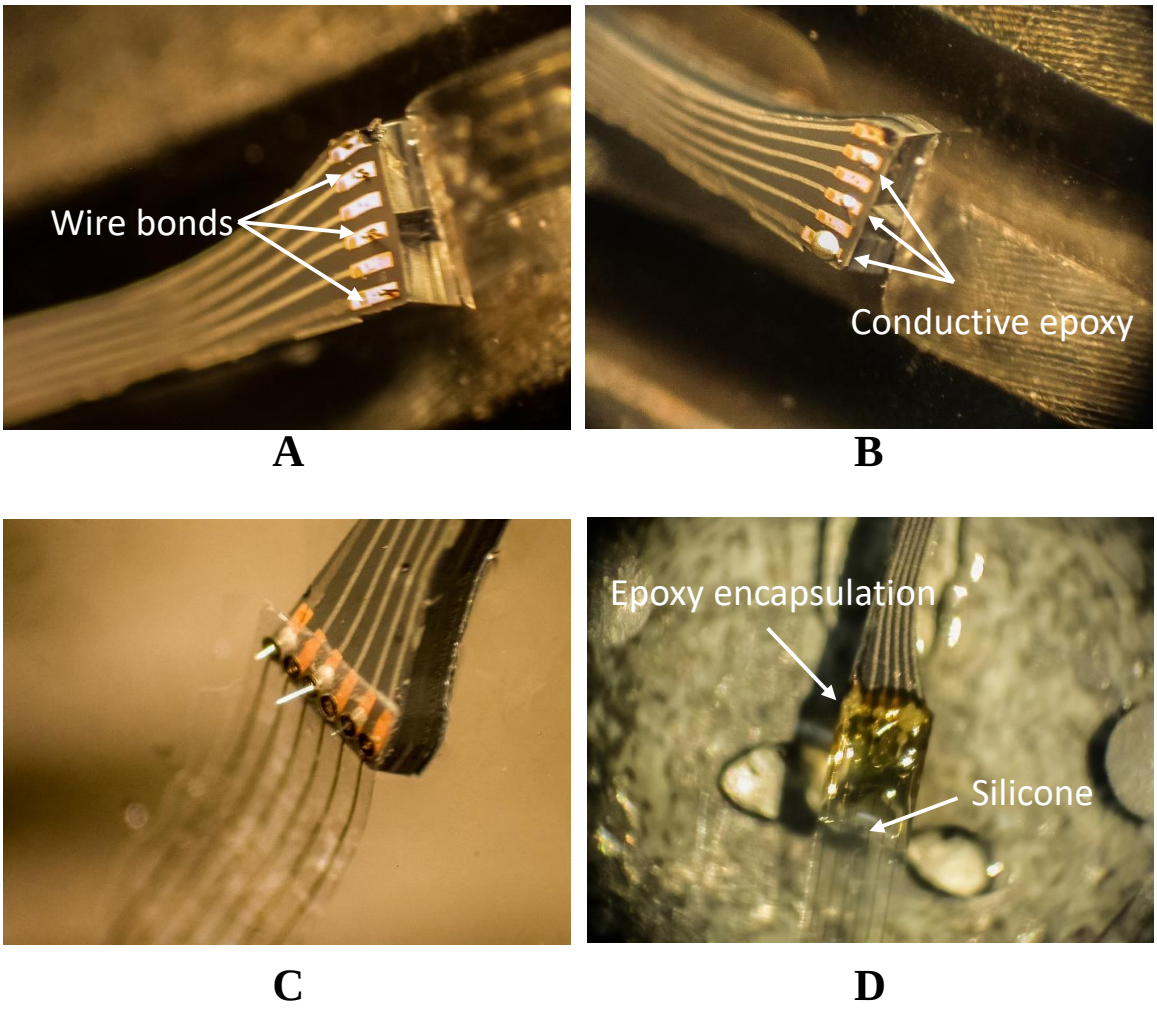

Figure 2.4: The wire-epoxy bonding process. (A) 25.4 μm thick Cu wire bonds were applied on the gold pads on the transducer. (B) The conductive epoxy was applied to secure the wire bonds. (C) The donut shaped gold pads on the parylene-gold cable were aligned and thread through the wire bonds. (D) Epoxy was applied to encapsulate the bonding joint, followed by silicone to relieve the stress.

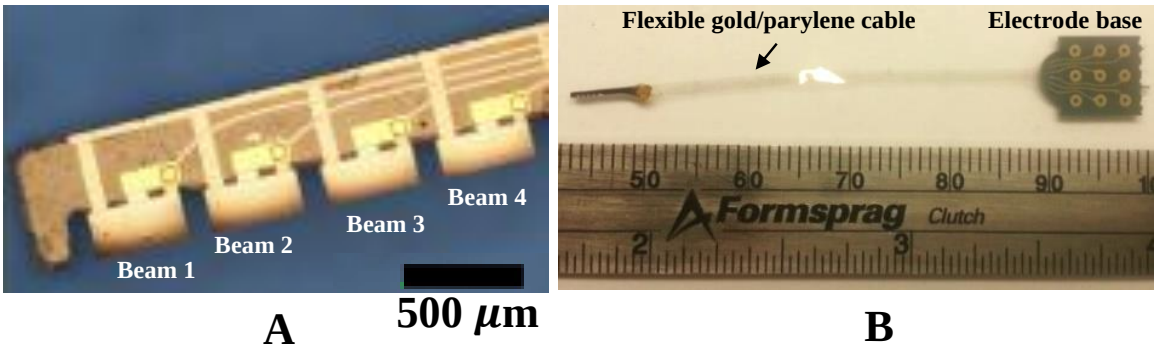

Figure 2.5: The fabricated xylophone transducer. (A) The xylophone transducer with four piezoelectric bimorph cantilever beams. (B) The xylophone with flexible gold/parylene cable and an electrode base.

Cascade Microtech Inc., USA), with the transducer probes mounting on the probe station (LA-150 DC, Semiprobe, USA). Out-of-plane vibration at the tip of each cantilever was measured using a laser Doppler vibrometer (LDV) with a laser spot size of approximately 30 μm (OFV-303, Polytec, USA). The AlN film piezoelectric coupling coefficient d_{31} was obtained by measuring the low-frequency curvature of the cantilever under an applied voltage; this technique is detailed in References [61, 68, 57]. A drop of water was carefully placed on the tip of the xylophone transducer using a syringe to test the transducer in a fluid environment, as shown schematically in Figure 2.6.

2.4 Results

2.4.1 Measured AlN Properties

The AlN thin film crystal quality was assessed by X-ray diffraction measurements. Figure 2.7A shows the θ-2θ curve. A strong peak at a 2θ angle of 36.2° and smaller peaks at angles corresponding to other AlN planes show the good quality of AlN films. Figure 2.7B shows a rocking curve of the AlN film. The rocking curve (Figure 2.7B) measured at the (002) peak of 36.2°, demonstrate a low (∼1.2°) full width

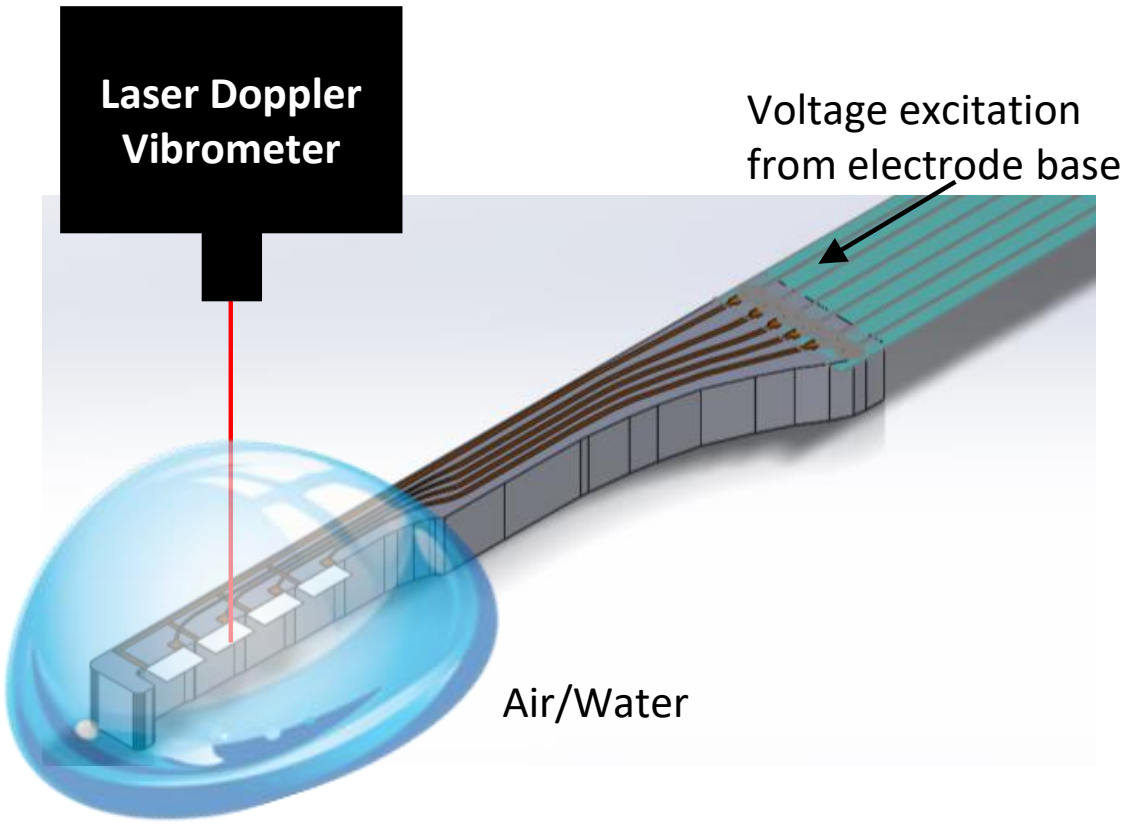

Figure 2.6: Experimental setup for the actuation testing. The transducer is actuated with voltage from the electrode base. The tip displacement of each cantilever beam (exposed to air or water) is measured by LDV.

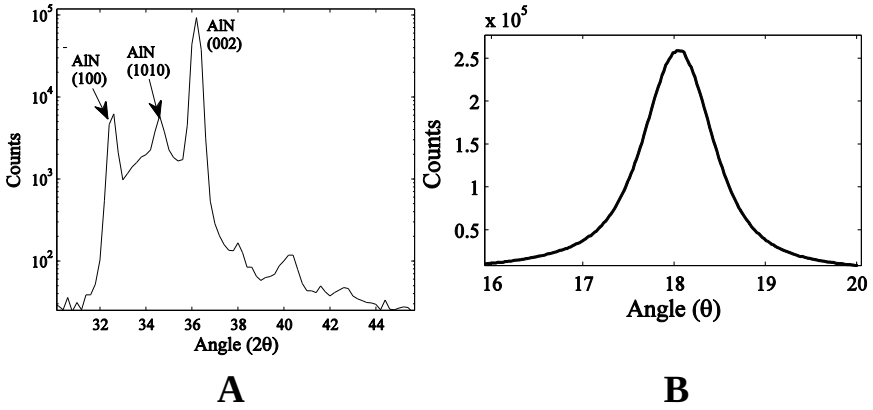

Figure 2.7: Measurements on the AlN film quality. (A) XRD $\theta - 2\theta$ pattern. (B) Rocking curve diffraction peak amplitude

half maximum (FWHM) value, which indicated good film quality [69, 70, 71, 72]. The capacitances of all four beams were measured at 1 kHz both before and after the bonding of parylene-gold cable. Before the integration of the parylene-gold cable, the capacitances of Beams 1-4 were measured as 6.7, 6.2, 5.9, and 5.5 pF, respectively, with a dielectric loss of 0.06. After the bonding, the capacitances became 13.3 pF (Beams 1 and 2) and 11.9 pF (Beams 3 and 4), with a dielectric loss of 0.08. Because Beams 1-2 were connected in parallel, and Beams 3-4 were connected in parallel, the new capacitance of each channel is the summation of the old capacitances of those two beams plus a stray capacitance of $\sim$0.5 pF. Once the probes were released from wafer, the piezoelectric coupling coefficient d_{31} was measured to be -1.9 pm/V, which is within the range of reported values of -0.9 to -2.8 pm/V [57, 68, 72, 73]. The measured d_{31} was further fed into the modeling calculation for the frequency response.

2.4.2 Actuation Testing in Air

To confirm the transducer functionality, actuation testing was done by measuring the deflection at the tip of each cantilever with a voltage chirp signal excitation with an amplitude of 1V. Figure 2.8 shows the modeled and measured frequency responses of the tip deflections of the cantilever beams. As one might expect, the modeled and

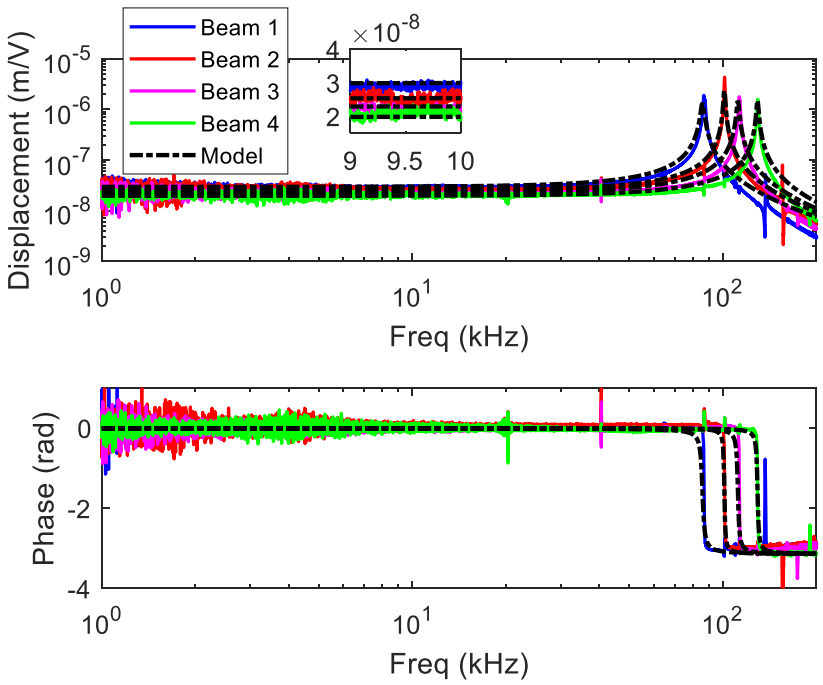

Figure 2.8: Frequency response of the tip displacement for each beam in air in response to voltage excitation. The inset shows the amplitude in a portion of the flat frequency region, from 9-10 kHz.

measured results match very well for both the amplitude and phase. Clear amplitude peaks and radian phase changes indicate the resonance of each cantilever beam at their respective, length-dependent resonance frequencies (f_r). The modeled and measured fr (tabulated in Table 2.2) values show a difference of less than 0.7%. The in-air quality factor Q is dominated by structural damping (η_s), as the acoustic losses were found negligible in the computation. The η_s values were fit to the experimentally measured Q values with a difference of less than 1.6%, as tabulated in Table 2.2. In addition, the model also shows a good fit in the flat low frequency region with a difference of less than 5%, as shown in the inset in Figure 2.8.

2.4.3 Actuation Testing in Water

Figure 2.9 shows the modeled and measured frequency responses of the tip deflections of cantilever beams, which are in excellent agreement. Just like the in-air

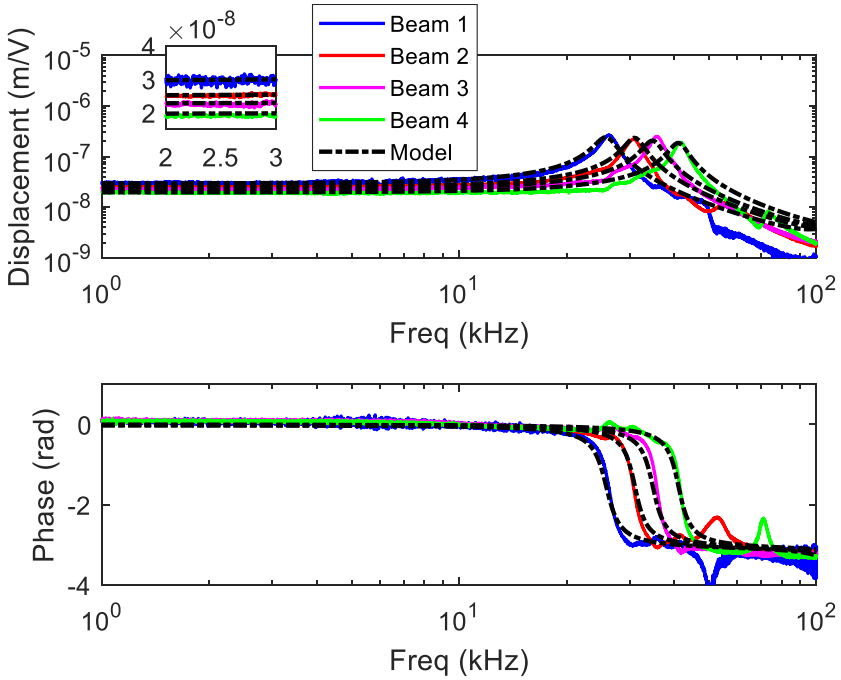

Figure 2.9: Frequency response of the tip displacement of each in water in response to voltage excitation. The inset shows the amplitude in a portion of the flat frequency region, from 2-3 kHz.

actuation results, the in-water actuation frequency response shows a clear peak in amplitude and a radian phase change at each resonance of the beam. Compared to the actuation in air, the fluid-loaded f_r shifted down by approximately 68-70% of the in-air value and the Q was decreased by 86-94%. As expected, the low frequency asymptote of the voltage response did not change. For actuation in water, the structural damping η_s is no longer the dominant damping source because the predicted Q was found to change less than 1% with the introduction of η_s. Instead, the viscosity of water becomes the main damping source and affects Q greatly. The modeled and measured f_s and Q showed a difference of less than 2.7% and 12.2%, respectively, as tabulated in Table 2.2. The modeled and measured low frequency asymptotes of the amplitude show a difference of less than 4%, as illustrated in the inset in Figure 2.9.

2.5 Discussion

Compared to the preliminary results of the AlN transducer [60], which had a 1.5 μm + 0.7 μm thick AlN layers due to unintentional overetch, the transducer in this paper had a symmetric 1.5 μm + 1.5 μm thick AlN layers. The lengths of the beams in this paper were chosen to tune the resonances to the best frequencies of the basal turn of the guinea pigs cochlea. Also, this paper made an advance by incorporating the xylophone transducer to a MEMS based parylene-gold cable, easing the remote access to the transducer and continuous monitoring for biomedical application. One might be tempted to adopt a monolithic process by combining the transducers and the flexible connection in one wafer [74, 57]. The monolithic fabrication process [74, 57], though it eliminates the bonding, is challenging for the following reasons. To begin with, compared to the current three-step fabrication process, the monolithic fabrication process takes much longer, because the xylophone transducer and flexible connection can be processed in parallel in the two-wafer process advocated in this paper. Additionally, monolithic process produces fewer probes per wafer because the cabling takes up a significant amount of wafer area and the yields in the three-step approach are higher. The initial fabrication using the monolithic process produced 11 probes on a 4 inch wafer, while the current process produced 60 AlN xylophone transducer probes and 15 cables on each 4 inch wafer. The wire-epoxy bonding technique is crucial for this three-step fabrication process. For our application, the wire-epoxy bonding technique is much more robust than the rivet bonding technique Meyer [67] developed because of the poor gold to AlN adhesion. As mentioned in the Introduction, this device can be used as an intracochlear transducer. Most recently, Zhao et al. [75] implanted such transducer inside a living guinea pig cochlea and sensed sound. With the recent development on the MEMS electrodes for cochlear implants [76, 77, 78], smaller electrodes can be fabricated using MEMS techniques and incorporated with the xylophone transducer to eliminate the external microphone of a CI. Also, the transducer

could be used as an intracochlear microspeaker to amplify sounds [79, 80]. In another application, such a transducer can also be used as a cardiovascular sensor to infer the blood flow or measure heart pressure fluctuations. Moreover, the multi-resonant characteristics enhance the sensitivity in a wide frequency range and could be used as a multi-resonant microphone or hydrophone, or even a broadband sound silencer [81, 82]. When attaching a proof mass to the end of the cantilever, it can work as a piezoelectric accelerometer [83, 84]. When scaled to operate at higher frequencies, this same architecture can also be used as a part of a ultrasound transducer [85] or a RF switch [86] or filter.

2.6 Conclusion

A miniaturized multichannel piezoelectric xylophone transducer with integrated flexible connection is fabricated using MEMS techniques. The transducer can work in both air and underwater, and is suitable for *in vivo* testing. The transducer consists of an array of AlN bimorph cantilevers with varied lengths whose resonances are tuned to a desired frequency range using FEA modeling. A wire-epoxy bonding technique is developed to electrically connect the xylophone transducer and flexible cabling, which are fabricated separately. Actuation tests are performed after the probes are released demonstrating the functionality of the xylophone transducer and the parylene-gold cable both in air and water. An FEA model is built to design and analyze the piezoelectric cantilever bimorph, and the model accurately represents the frequency behavior of the cantilever in a viscous fluid. Taken together, a method to design, model, fabricate and test a xylophone transducer with flexible cable connection was developed, providing a systematic way to develop a cantilever-based piezoelectric transducer for operation in air or underwater.

CHAPTER III

In Vivo Study of the Implantable AlN Xylophone Transducer Using in a Living Guinea Pig Cochlea

The ability to locally measure the voltage readout from a sensor inside the living cochlea holds the potential to improve cochlear implants and enable continuous monitoring of intracochlear pressure. This chapter presents a PIAT designed to sense the acoustic pressure while fully implanted inside a living guinea pig cochlea. The PIAT, fabricated using MEMS techniques, consisted of an array of four piezoelectric cantilevers with varying lengths to enhance sensitivity across a wide frequency bandwidth. Prior to implantation, benchtop tests were conducted to characterize the device performance in air and in water. When implanted in the cochlea of an anesthetized guinea pig, the *in vivo* voltage response from the PIAT was measured in response to 80-95 dB sound pressure level (SPL) sinusoidal acoustic excitation at the entrance of the guinea pigs ear canal, spanning 1-14 kHz. All sensed signals were above the noise floor and unaffected by crosstalk from the cochlear microphonic (CM) or external electrical interference. These results demonstrate that external acoustic stimulus can be sensed via the piezoelectric voltage response of the implanted MEMS transducer inside the living cochlea. We present the manufacturing and implantation methodologies that represent key steps along the critical path to developing intracochlear acoustic sensors with the potential to replace external or subcutaneous

microphones for sensing the acoustic signal in auditory prosthetics.

3.1 Methods

3.1.1 Fabrication Process of the PIAT

The probes were fabricated in the following manner, which is summarized in a schematic in Figure 3.2. A 102 mm diameter p-type (100) Si wafer substrate of 500 μm thickness was coated with 1 μm of wet thermal oxide. The transducers were comprised of a five-layer stack, consisting of two 1.5 μm of AlN layers laminated between three 15/30 nm Ti/Pt electrode layers. Alternating layers of metal layers and AlN layers were deposited. The Ti/Pt layers were sputtered (Lab 18-2, Kurt J. Lesker Company, USA), and patterned by photolithography using SPR 220 photoresist and CD 30 developer. The traces in the metal layers were 20 μm wide in the implantable part (first 4 mm from the tip) and were widened to 40 μm wide in the stern away from the tip. The AlN layers were deposited using a dual cathode S-Gun magnetron AlN sputter tool (AMS 2004, Tegal OEM group, USA) with bulk film stress targeted to 0 $\pm$ 150 MPa (Figure 3.2A). The active area of the piezoelectric bimorph was limited to 45% of the distance from the root toward the tip of the cantilever to improve the input referred noise of the devices (adding more electrode area adds electronic noise in greater proportion than the increase in output signal [61, 4]). The AlN cantilevers metal contacts were opened using an etch process that was a combination of Cl-based RIE (9400, LAM Research Corporation, USA) and heated (50°C) etchant (AZ 400K, Clariant, USA) etching, and the cantilever geometry was defined using Cl-based RIE etching.

The top layer of AlN was unintentionally overetched by 0.8 μm (leaving 0.7 μm on this layer) and a bimorph thickness of 2.2 μm. An asymmetrical AlN bimorph was created and the top surfaces were roughened (Figure 3.2B). We found that the

lowest noise sensor was created by using the non-roughened bottom layer and using roughened top layers as a structural layer only. The top and middle layer were connected and served as ground layer, and the bottom layer was connected to the signal trace. A layer of 20/400 nm of Cr/Au was sputtered (Lab 18-2, Kurt J. Lesker Company, USA) and formed the electrode pads (100 μm wide and 300 μm long) for bonding the Pt-Ir wire (Figure 3.2C). The probe backbone was then defined using a through-wafer DRIE (STS Pegasus 4, SPTS Technologies Ltd., USA), followed by a BHF oxide etch to release the cantilevers. Details of the fabrication can be found in Reference [74, 60, 57, 87]. Two 50 μm thick Pt-Ir wires with PFA insulation (776000, A-M system, USA) were bonded on the electrode pads. One wire was bonded on the ground trace and the other one was bonded on the pads where all signal traces were connected in parallel. The bonding was utilized conductive epoxy (H20E-FC, Epoxy Technology, USA) and was followed by Silicone sealing (3140 RTV Silicone, Dow Corning, USA). After the MEMS fabrication, the probe was coated with a combination of 50 nm of thermal atomic layer deposition (ALD) alumina (Oxford OpAL ALD, Oxford Instrument, UK) and 2 μm of parylene (PDS 2035CR, Special Coating System, USA) to enhance the long term reliability of the PIAT probe in an ionic fluid environment [88, 89] (Figure 3.2D). All probes were fabricated in the Lurie Nanomanufacturing Facility at the University of Michigan.

3.1.2 In Air and Underwater Actuation and Sensing Benchtop Testing

The PIAT was tested in air and in water. Figure 3.1A showed the actuation test setup. The actuation tests were performed using LabVIEW 2009 controlled NI-6251 card to apply voltage directly to the probe. The resulting tip deflections were measured using a laser Doppler vibrometer (LDV; OFV-303, Polytec, USA), with spot size 30 μm. The device was mounted on a probe station (LA-150 DC, Semiprobe, USA) with a 2D micropositioning stage. The water actuation test was done with

a drop of water delivered to the implantable portion of the PIAT probe, covering all cantilevers. A goniometer (123-2890, Optosigma, France) was used to adjust the angle of each cantilever beam for the best reflectiveness.

The sensing tests were done by applying acoustic excitation and measuring the voltage from the PIAT with a lock-in amplifier (SR830, Stanford Research System, USA), as illustrated in Figure 3.1B and Figure 3.1C. A custom-made amplifier (an instrumentation amplifier (MAX4462, Maxim Integrated, USA) and an operational amplifier (LT6233, Texas Instrument, USA)) were used to buffer and amplify the voltage signal. The amplifier gain of 100 was factored out of all the results presented here. Figure 3.1B shows the setup for the in-air sensing test. A 304.8 mm long plastic tube was placed in between the PIAT and a piezo speaker (15D841, Motorola, USA). Pure tone sinusoidal signals were sent into the speaker and swept through 40-80 kHz. A calibrated microphone (2520, Larson Davis, USA) was used at the same location to measure the sound pressure level. As shown in Fig 4C, underwater sensing tests were done by immersing the PIAT probe below the water surface of a tank with approximately 0.1 m^3 volume of tap water and playing sounds (120 kHz) with an underwater transmitter (ITC-1032, Channel Technologies Group, USA). A hydrophone (TC4013, Teledyne Reson, USA) was used to measure the sound pressure level at the same location. The tap water was connected to the ground to eliminate electrical interference.

3.1.3 Experimental Animal

The animal used in these acute experiments was an adult male specific pathogen free (SPF) pigmented guinea pig (600 g) bred and maintained by the Unit for Laboratory Animal Medicine at the University of Michigan. The animal-use protocol was reviewed and approved by the University of Michigan Institutional Animal Care and Use Committee. All experiments were performed in accordance with relevant guide-

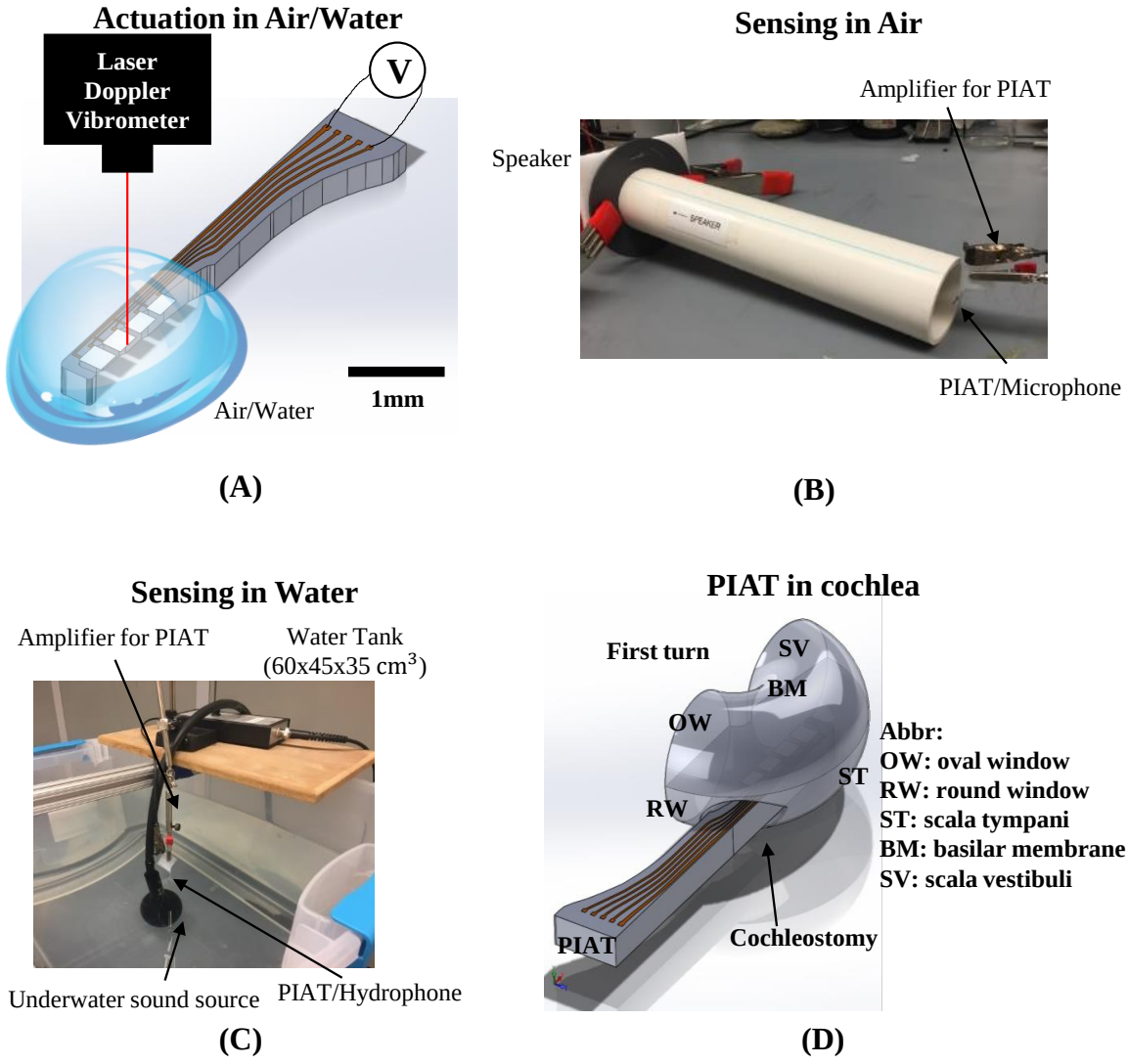

Figure 3.1: Schematics for the methods. (A) Benchtop actuation test setup. Voltage was used to actuate each of the cantilever beams in air and water. The deflection at the tip of each beam was measured using a LDV (B) Benchtop sensing test setup in air. Acoustic signals were generated by a piezo tweeter in air and passed through a 304.8 mm long PVC tube. The PIAT was placed at the end of the tube and the output was compared to that of a calibrated microphone. (C) Benchtop sensing test setup in air. Acoustic signals were generated by an underwater sound source in a water tank filled with tap water. The PIAT was placed near the water surface to sense the sound and compared with a calibrated hydrophone. (D) A CAD drawing illustrating the position of the PIAT as it passes through a cochleostomy into the scala tympani of a living cochlea.

lines and regulations. The PIAT was implanted in the right ear. After all testing was complete, the animal was euthanized and the cochlea was dissected for confirmation of implant location and integrity as detailed below.

3.1.4 Implantation Procedures

The animal was anesthetized with ketamine (40 mg/kg) and xylazine (10 mg/kg), given atropine (0.05 mg/kg) to help with respiration, and placed on a heating pad. A post-auricular incision was made, the temporal bone was exposed by blunt dissection, and the bulla was opened. After confirmation of a normal uninfected ear, the bulla was temporarily closed with a small cotton ball and the recording and electrode base (percutaneous connector) anchoring screws were placed on the skull. A midline incision was made on the skull, and the skin and pericranium were retracted for view of bregma. Screws were placed at three points around the bregma and these were used to secure a small inverted bolt, which could serve as a ground and/or anchor for the electrode base. This bolt was secured permanently with methyl methacrylate. Additional screws were placed at the midline, 1 cm caudal to bregma, and one 1cm from the midline and slightly behind bregma on the implant side.

Once all hardware was secured, the cotton ball sealing the bulla was removed and a portion of the lateral wall of the basal turn of the scala tympani of the cochlea was removed with a small diamond bur until the basilar membrane and first turn could be seen clearly and there was room for insertion of all beams of the PIAT. Perilymph was wicked out with a cotton pledget for viewing of the cochlear structures and a dummy implant was used to gage opening size and angle before insertion of a functional implant. Once the opening was large enough, the electrode base was temporarily affixed to the skull surface and anchor screws with Durelon cement. Then, the implant was gripped with forceps and inserted into the scala tympani to the depth of the first turn following the lateral edge of the scala tympani and angled such that the beams

were parallel with the basilar membrane surface. Figure 3.6C and Fig 4D showed the location where the PIAT was implanted. A small muscle plug was placed on top of the implant and into the cochleostomy opening in an attempt to seal the opening and prevent leakage of perilymph. With Durelon cement, the implant was secured to the bulla and the bulla opening sealed. For grounding purposes, a flamed 5T platinum iridium ground ball electrode was tucked into the neck muscle overlying the temporal bone. The skin incision was closed over the implant and ground wires and the implant was tested for functionality, as detailed below. Once functionality was confirmed, the electrode base was permanently secured to the skull and the anchor screws with methyl methacrylate and the animal was moved to a sound-attenuating booth for the remainder of the testing. Supplemental doses of the ketamine, xylazine and atropine anesthesia regime listed above were given throughout testing to maintain a consistent depth of anesthesia to perform the electrophysiology and implant recordings.

3.1.5 Hearing Condition for the Tested Animal

As discussed in the Results, the PIAT was not affected by the CM. Therefore, the device can work in both deafened and not deafened animals. In the test presented in this paper, the guinea pig was not deafened. However, the hearing threshold was elevated significantly. To evaluate the hearing condition of the ear after PIAT implantation, The auditory brainstem response (ABR) was recorded and the hearing threshold for multiple frequencies determined. The thresholds for the frequencies tested were 100 dB (2 kHz), 80 dB (4 kHz), 70 dB (8 kHz), 60 dB (10 kHz), 85 dB (12 kHz), and 75 dB (16 kHz) SPL. These were considerably elevated compared to normal thresholds. These results showed the hearing was impaired, and that the CM should be fairly small; smaller than 1 mV as has been measured in healthy animals [90]. During the ABR test, the animal was kept anesthetized and placed on a heating blanket in a sound attenuating booth. Needle electrodes were positioned

subcutaneously at the vertex and bilaterally underneath the pinna. An acoustic transducer with a speculum was placed just inside the tragus and pointed toward the tympanic membrane. Tone bursts were presented and responses were recorded using a Tucker Davis Technology System 3 BioSig32 system.

3.1.6 *In vivo* Measurement of Voltage Output of the PIAT inside the Cochlea of a Live Guinea Pig

Figure 3.6C and Figure 3.1D illustrate the location where the PIAT was implanted. After implantation, a speaker (ES 1, Tucker-Davis Technologies, USA) was directed at the tympanic membrane via a speculum to the ear canal and a series of frequencies ranging from 1-14 kHz at levels from 80-95 dB SPL were played. While playing these acoustic excitations, a lock-in amplifier (SR830, Stanford Research System, USA) was used to measure the voltage output of the PIAT located inside the cochlea. Just like in the benchtop testing, the custom-made amplifier was used to buffer and amplify the PIAT voltage response. This amplification gain was again factored out. *In vivo* noise was obtained by playing sound in air, with the speaker pointing away from animal and the ear canal occluded. Electrical impedance of the PIAT was measured with an LCR meter (E4980A, Agilent, USA) before the implantation and every 30 minutes during the *in vivo* experiment to continuously monitor the condition of the device.

3.1.7 Post Mortem Cochlear Dissection and *Ex Vivo* Actuation in Air

At the completion of testing, the animal was euthanized and stored in a freezer. Two days later, the implanted cochlea was dissected to assess implant insertion location and the status of the implants beams (Figure 3.6C and 3D). The cochlea was approached by removing the ear canal and the outer wall of the otic capsule. The cochlea was then scored on the surface with a scalpel blade and starting at the apex

the outer boney wall was gently removed with a pair of fine forceps exposing the coils of the cochlear spiral, basilar membrane, and modiolus. Each cochlear turn was inspected for damage caused by the implant and the angle and general location of the implant. Once the basal most turn was exposed, the status of each beam was assessed. Figure 3.6D shows the assessment and status of each beam. Finally, the modiolus was removed for complete visualization of the implant in the basal turn and for gentle removal of the implant for functionality testing post-removal. The PIAT probe was actuated by voltage and tip deflection of the beams was measured by an LDV.

3.2 Results

3.2.1 Realization of the PIAT Using AlN Cantilever Arrays

The PIAT probes were fabricated [74, 60, 45] using the process described in the Methods section, and summarized in Figure 3.2. Briefly, the PIAT probe consists of four 400 μm wide piezoelectric cantilevers of different lengths that span 300 μm to 443 μm, as given in Table 3.1. The resonant frequencies of the cantilevers are spaced such that the sensor has enhanced sensitivity over an extended frequency bandwidth that corresponds, in the water-based fluid environment of the cochlea, to a frequency range of 5.6 to 13.5 kHz. A 3D rendering for the design of the PIAT is pictured in Figure 3.2A. Once the probes were released from the wafer, they were coated with 50 nm atomic layer deposition (ALD) alumina and 2 μm parylene to increase the durability of the waterproofing. The electrical insulation of the PIAT from the environment was confirmed by measuring the electrical impedance of the PIAT using an impedance analyzer at 1 kHz both in air and under submersion in saline. The measured electrical impedance was the same both in air and in saline, and the impedance was measured as a capacitor $C_d = 38$ pF, with a parasitic parallel

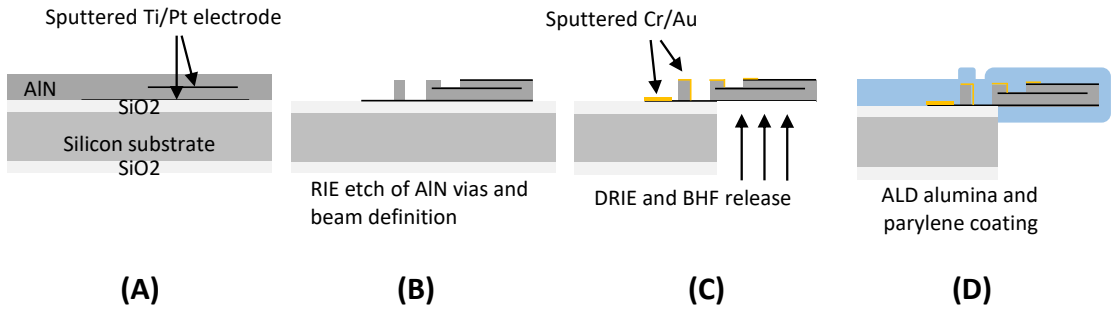

Figure 3.2: PIAT MEMS fabrication process. (A) AlN deposition and Ti/Pt electrode layer deposition and patterning. (B) RIE etch of the AlN layers to define beam dimensions and create vias to the middle and bottom electrode layers. The top AlN layer was overetched as described in the Methods. (C) Cr/Au deposition for circuit layout connection, followed by DRIE and BHF release. (D) Waterproof coating that consists of ALD alumina and parylene conformal coating after device release.

resistance $R_p = 81$ MΩ. This impedance remained unchanged through a 5 hour submersion in saline, demonstrating the effectiveness of the coating. Figure 3.2B shows the cross section of the multilayer AlN cantilever beam. The sensing portion of the released probe is shown in Figure 3.2C. The signal and ground traces of the PIAT probes were bonded to Pt-Ir wires are shown in Figure 3.2D, as described in the Methods section. Using previously reported techniques [61], the piezoelectric coupling coefficient d_{31} of the AlN was determined to be -1.0 pm/V. This value is on the low end of the range measured by others (-0.9 to -2.8 pm/V) [61, 72, 57, 73].

		In air		In Water	
	Length (μm)	f_r (kHz)	Q	f_r (kHz)	Q
Beam 1	443	18.8	90	5.6	3.5
Beam 2	397	23.8	47	7.1	3.9
Beam 3	345	31.6	53	9.9	4.4
Beam 4	300	40.8	56	13.5	4.7

Table 3.1: PIAT parameters after the alumina/parylene coating, which include beam length, resonant frequencies f_r, and quality factors Q in air and in water.

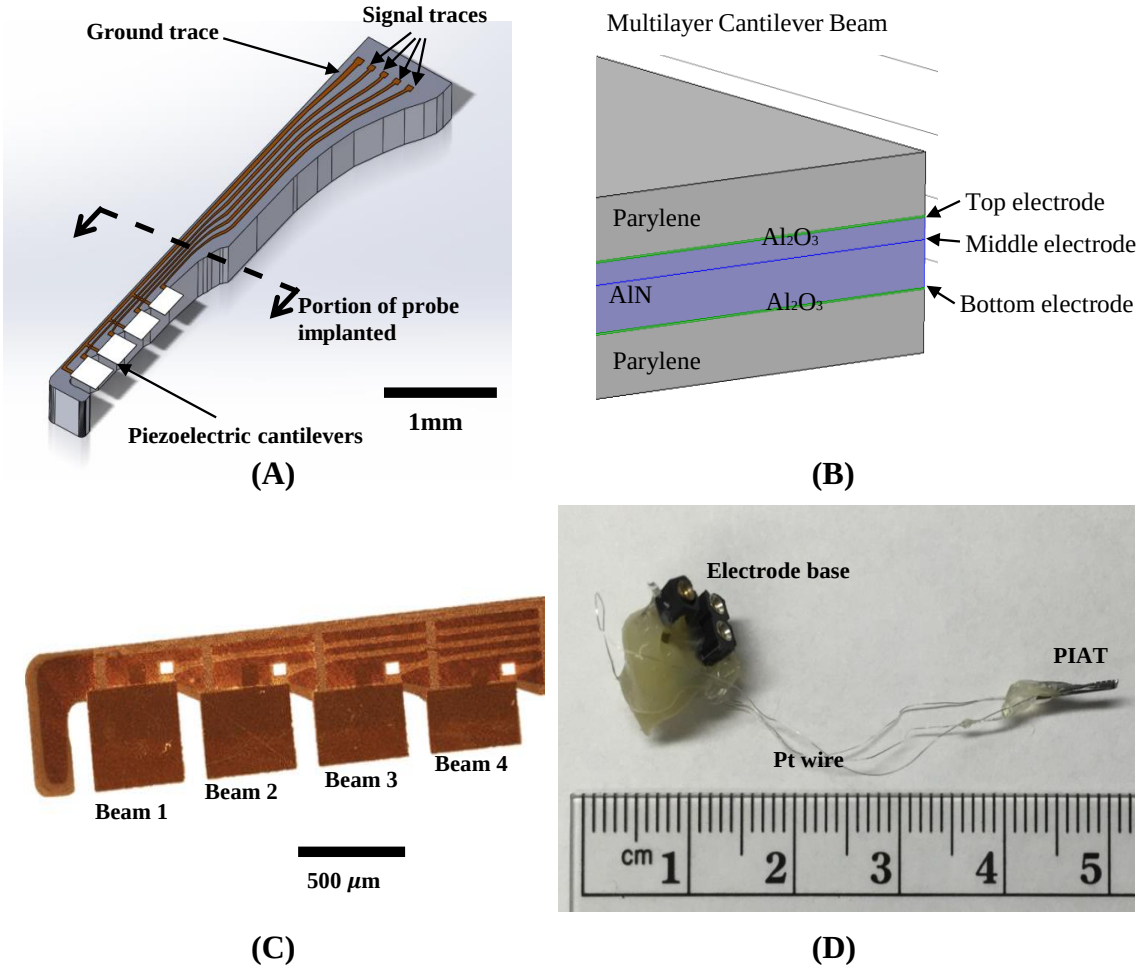

Figure 3.3: The designed and fabricated PIAT. (A) A 3D drawing of the PIAT, which consists of four piezoelectric cantilevers with variable lengths on a silicon shank. (B) A cross-section view of the multilayer cantilever beam. (C) A micrograph of the implantable portion of a fabricated probe. (D) A fabricated PIAT bonded with Pt wires and an electrode base (percutaneous connector).

3.2.2 Benchtop Actuation Testing

In order to verify the device functionality and determine the input-output characteristics, the PIAT probes were tested on the benchtop both in air and in water. In the actuation testing, the vibration of the beams in the PIAT was measured when the PIAT was actuated with voltage. The testing results are shown in Figure 3.4A and Figure 3.4B. The measured resonance frequency (f_r) and quality factor Q (where the $Q = \frac{f_r}{\Delta f}$), and Δf is the full width at half maximum) of the cantilevers, in air and water, are summarized in Table 3.1.

In Figure 3.4A, the in-air displacement of the tip of each beam, in response to voltage input and as a function of frequency, is plotted, showing clear peaks at each of the beam resonances. Before the parylene/alumina coating was applied (upper panel in Figure 3.4A), resonance frequencies of 18.9, 23.7, 31.5, and 41.0 kHz were measured in air, and the maximum tip displacements ranged from 1-4 μm at resonance. The frequency response of the beams coated with ALD alumina and parylene C is shown in the lower panel. After the coating, the peak displacements were reduced to 0.4-1 μm and the measured resonances shifted about 2%. This small change in the resonance was due to the balancing of the added mass-loading effect of the compliant parylene coating and the stiffening caused by the ALD alumina coating. The stiffening effect was mainly due to the residual stress (with very high residual stresses for thin layers) [91, 92, 93, 94].

The frequency responses of the electrically excited beams submerged in water are shown in Figure 3.4B. The measured frequency responses without the alumina/parylene coating are shown in the upper panel, and the fluid-loaded resonance frequencies are shown in the lower panel. The resonance frequencies (shown in Table 3.1) were reduced to approximately 65-75% of the in air values, and the Q (shown in Table 3.1) was decreased significantly. The largest peak displacement at resonance was reduced to 0.2 μm underwater. The low frequency displacement of each beam, however, was

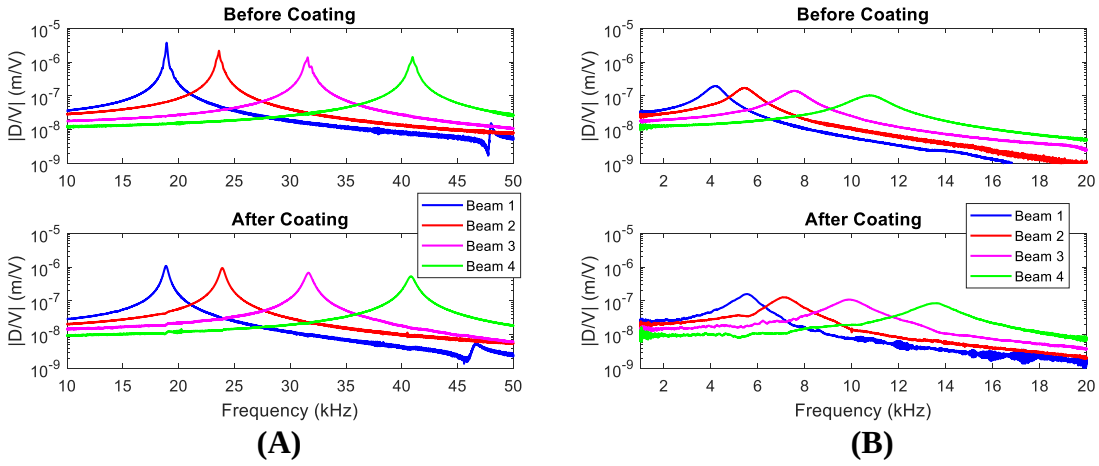

Figure 3.4: Benchtop actuation tests. (A) Actuation test in air. The beam tip displacement in air in response to voltage actuation (|D/V|) before (upper) and after (lower) alumina/parylene coating. (B) Actuation test in water. The beam tip displacement in water in response to voltage actuation before (upper) and after (lower) alumina/parylene coating.

unchanged from the in-air value. After the alumina/parylene coating was applied, as shown in the lower panel in Figure 3.4B, the resonances increased as much as 31% in water. When the PIAT was submerged in water, the mass-loading effect of the water dominated over that of the parylene coating, resulting in little change to the mass-loading of the system, whereas the stiffening was significantly increased by the addition of the ALD alumina coating, resulting in an increased resonant frequency in water.

3.2.3 Benchtop Sensing Testing

The benchtop sensing testing was conducted after the actuation testing to further confirm the device functionality as a sensor. The piezoelectric voltage output from the PIAT was measured when the PIAT was excited by acoustic signals both in air and in water. The results are shown in Figure 3.5A and Figure 3.5B. In-air acoustic sensing tests were conducted after the alumina/parylene coating was applied, as detailed in

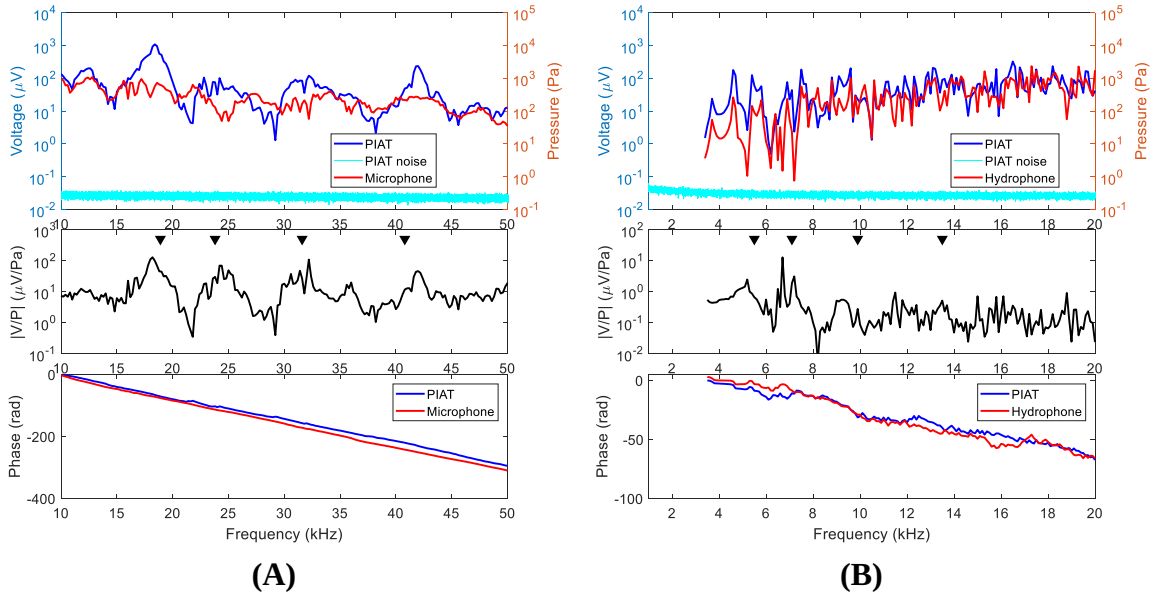

Figure 3.5: Benchtop sensing tests. (A) Sensing test in air. The upper panel shows the voltage output from the PIAT (blue line with units on the left axis), the device noise floor (cyan line with units on the left axis), and the acoustic pressure measured by microphone (red line with units on the right axis). The middle panel shows the transfer function (|V/P|) of the measured voltage from the PIAT and the measured pressure from the microphone. The resonances of the beams in air from actuation tests are shown as black triangles for comparison. The phase plot in the lower panel shows the phase difference between the speaker-driving voltage and the measured signal by the PIAT (blue line) or microphone (red line). (B) Sensing test in water. The upper panel shows the voltage output from the PIAT (blue line with units on the left axis), the device noise floor (cyan line with units on the left axis), and the acoustic pressure measured by hydrophone (red line with units on the right axis). The middle panel shows the transfer function of the measured voltage from the PIAT and the measured pressure from the hydrophone. The resonances of the beams in water from actuation tests are shown as black triangles for comparison. The phase plot in the lower panel shows the phase difference between the speaker driving voltage and the measured signal by the PIAT (blue line) or hydrophone (red line).

the Methods. The piezoelectric voltage output in response to pure tone pressure excitation in air for frequencies from ranging 10-50 kHz is shown in Figure 3.5A. The upper panel in Figure 3.5A shows the piezoelectric voltage output from PIAT (blue line) and the device noise floor (cyan line) with the axis and label on the left. The measured voltage was clearly above the noise floor with a signal to noise ratio (SNR) of at least 35 dB. The acoustic pressure measured by microphone (red line) is also shown with axis and label on the right. The transfer function between the measured voltage output from the PIAT and the pressure from the microphone is shown in the middle panel of Figure 3.5A. The frequencies of the amplitude peaks matched well with the voltage actuated resonances (shown as black triangles). The voltage minima between the resonance frequencies were due to the out-of-phase summation of currents generated by higher and lower frequency modes of adjacent beams. The lower panel shows the phase of the voltage from the pressure sensor (for either the PIAT or the microphone) relative to the drive voltage sent to the speaker (note that this is not the phase of the sensitivity). This phase was dominated by the acoustic delay from the speaker to the sensor. We used the slope of the phase to determine a delay of 1.14 $\pm$ 0.002 ms as measured by the PIAT and 1.19 $\pm$ 0.003 ms as measured by microphone. These delays corresponded to distances of 0.39 $\pm$ 0.0007 m and 0.41 $\pm$ 0.001 m for sound travelling in air as measured by microphone and the PIAT, respectively. Because the delay of the PIAT output corresponded to the appropriate acoustic delay and the resonant amplitudes match the driven resonant frequencies of the probe, we are confident that the response was not contaminated with cross talk from the drive signal to the loudspeaker.

Sensing in water was tested for frequencies ranging from 3.5-20 kHz with the results shown in Figure 3.5B. Just like Fig.2C, the upper panel shows the voltage output from the PIAT (blue line) and the device noise floor (cyan line) with their axis on the left, as well as the acoustic pressure measured by hydrophone (red line)

with the axis on the right. The measured voltage was at least 15 times higher than the noise floor (SNR was at least 23 dB). Unlike sensing in air, both the voltage response and pressure response show large fluctuations through the measured frequency range, because of the reflections of the water tank. The fine-structure peaks in the voltage response (blue) align very well with the peaks in the pressure response (red) because the hydrophone was replaced at the same location as the PIAT. The middle panel shows the transfer function of the measured voltage from the PIAT and the measured pressure from hydrophone. Compared to sensing in air in Figure 3.5A, the transfer function amplitude peaks due to beam resonances were less prominent because of the damping of the fluid (as seen in Figure 3.4B) and the reflection of the water tank (as seen in the upper panel in Figure 3.5B). However, the peaks around 5.6 kHz and 7.1 kHz were observed, which corresponded to the fluid-loaded resonances of Beams 1 and 2 measured under direct electrical stimulation (the voltage-actuated resonances are shown as black triangles). The peaks corresponding to the resonances of Beams 3 and 4 were less pronounced, because the beams were located closer to the air-water interface where acoustic pressure was smaller. We confirmed this by moving the probe 1 cm closer to the water surface and found that the PIAT voltage output was reduced by 50%. The sensor phase relative to the driving voltage (for the PIAT or hydrophone) is shown in the lower panel. In the 8-20 kHz range, a delay of 0.62 $\pm$ 0.03 ms was measured by the PIAT and a 0.64 $\pm$ 0.02 ms delay was measured by the hydrophone. The difference in the delays were within the measurement accuracy.

3.2.4 *In Vivo* Response

The PIAT was implanted in the cochlea of the anesthetized guinea pig, as described in the Methods. After the implantation surgery, the transducer impedance was measured (as described in the Methods) and compared to the impedance measured before the surgery, in order to check the electrical integrity of the device. A

parasitic parallel capacitance $C_p = 3$ pF was measured in addition to the device capacitance $C_d = 38$ pF. The parasitic parallel resistance R_p decreased from 81 MΩ to 10 MΩ. This change in impedance decreased the device sensitivity by no more than 10%. These results indicate the PIAT was successfully implanted with some minor compromise on the device performance.

After confirming the device was properly implanted and functioning, the *in vivo* voltage response was measured. The pure tone acoustic excitation was applied in the ear. The acoustic signal traveled through the ear drum and the middle ear to the cochlea, where the PIAT was implanted. The voltage output of the implanted PIAT in response to external acoustic excitation was measured, as shown in Figure 3.6A. The external acoustic excitation spanned from 1-14 kHz and ranged from 80-95 dB sound pressure level (SPL) with a 5 dB difference of each step. The voltage output of the PIAT in response to the 80-95 dB SPL input was linear to input pressure, because the active processes responsible for cochlear nonlinearity were rendered inoperable or certainly made less efficient by the invasive nature of this surgery [95]. Besides, the input-output relations of the cochlea to a pure tone at relatively high SPL were also typically nearly linear [95]. Voltage outputs of 1.3-79.7 μV from the PIAT with an SNR that varied from 17 dB to 70 dB were measured in response to a 95 dB SPL input stimuli over frequencies of 1-14 kHz. The PIAT showed a higher response around 2-9 kHz, near to the fluid-loaded resonances of Beams 1 and 2. The phase showed an accumulation consistent with the delay associated with the travel time from the speaker to the cochlea, as shown in the lower panel of Figure 3.6A, which indicated that the signal collected was not noise or crosstalk (e.g., crosstalk would typically have a constant phase value). The voltages of 1.3-79.7 μV in response to the 95 dB SPL input (or 1.2-70.9 μV/Pa) measured *in vivo* in the cochlea were much higher than 0.05-12.6 μV/Pa as measured outside the cochlea in a water tank to an excitation with the same acoustic pressure level. (The *in vivo* results were compared to sensing

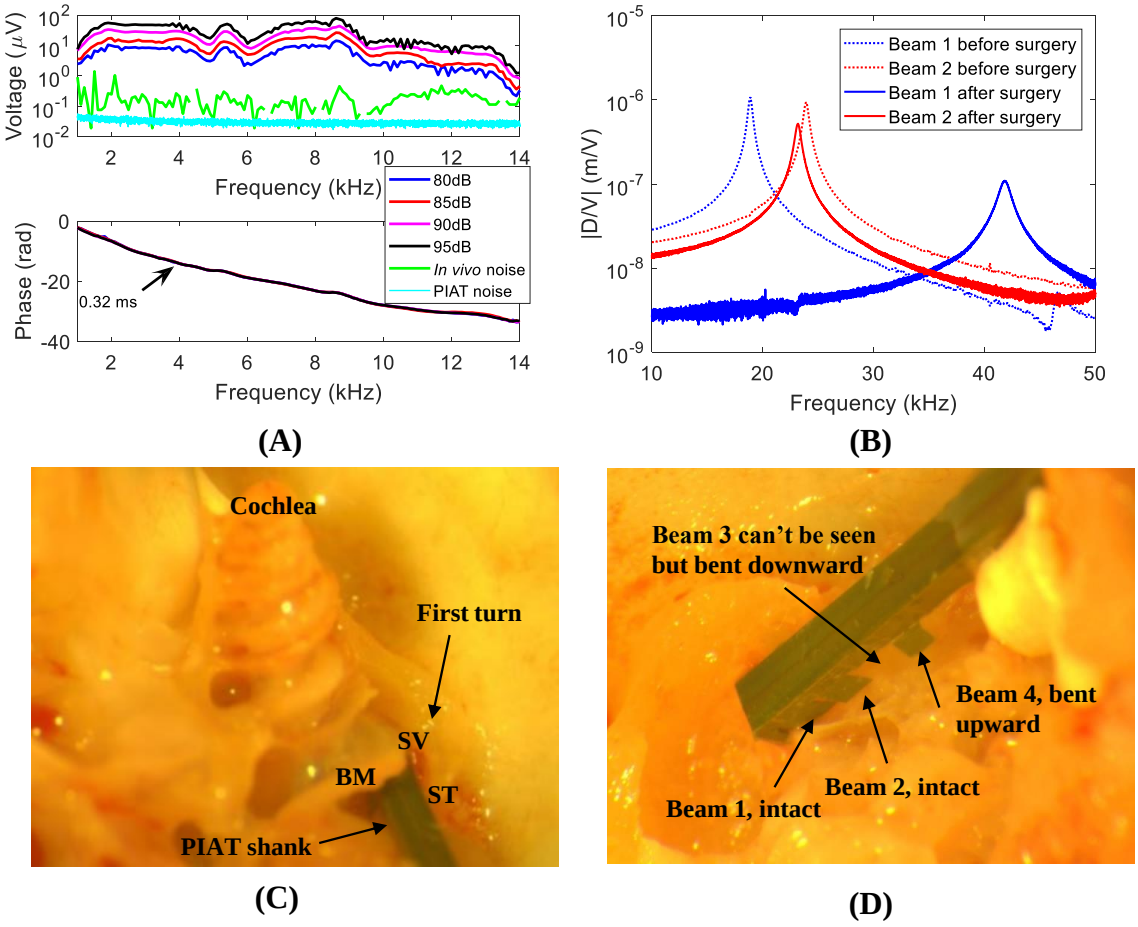

Figure 3.6: *In vivo* testing results. (A) The *in vivo* frequency response with different SPL inputs, in vivo noise and intrinsic PIAT noise floor measured in a closed sound attenuating chamber. A 0.32 ms delay, derived from the phase slope, agrees with the acoustic delay from the speaker to the PIAT. (B) A picture showing the location of the PIAT probe placed inside the guinea pig cochlea. (C) A picture showing the four beams after dissecting the cochlea in *post mortem* analysis (into the paper refers to the downward direction). (D) Comparison of in-air actuation transfer functions for Beams 1 and 2 before implantation surgery and after retrieval from the cochlea. (|D/V| means the amplitude of the measured displacement/input voltage)

in water because the scala tympani was filled with watery fluid perilymph). This gain (∼15-40 dB) was due to the acoustic environment inside the cochlea being different than the water tank. More importantly, a higher output *in vivo* was expected since the middle ear gain measured in rodents previously was found to be as high as 38 dB inside the living cochlea of a guinea pig [23] or 10-50 dB pressure for a gerbil [21, 22].

The measured *in vivo* voltages were also compared to the noise levels of the sensor system and experimental test configuration. The *in vivo* noise was measured by recording the lock-in amplifier output from the implanted PIAT with no input to the speaker. The *in vivo* noise was due to the combination of electric noise of the testing system, intrinsic device noise, the cochlear ambient environment, and the amplifier noise. As seen in Figure 3.6A, the *in vivo* noise level was below the sensed signal (0.2 μV in the 2-10 kHz range, and around 0.3 μV in the 10-14 kHz range, with 80 dB SPL input). The intrinsic PIAT noise floor was measured in a sound isolation chamber prior to the surgery. The intrinsic device noise floor was the even smaller than *in vivo* noise and was 0.03-0.04 μV in the 1-14 kHz range as shown in Figure 3.6A. Overall, all measured voltages were clearly greater than any noise in the system.

After the *in vivo* sensing tests, the guinea pig was sacrificed, and the cochlea was dissected to examine the condition of the PIAT. Then, the PIAT was retrieved from the cochlea. Cochlea dissection was a highly destructive procedure. Remarkably, the excised PIAT was still partially functioning as a transducer with Beams 1 and 2 operational, as confirmed by *ex vivo* in-air voltage actuation tests, demonstrating the robustness of this sensor design. In Figure 3.6B, the tip displacement of the excised probe in response to voltage excitation (as in Figure 3.4A) is presented and compared to the results prior to implantation. *Ex vivo* actuation responses indicated that Beam 2 was still fully functional, while the resonant frequency of Beam 1 was shifted to a higher frequency. After pulling the PIAT out from the guinea pig, Beam 1 was slightly bent and was found partially covered with tissue at the base of the

cantilever, which was likely the cause for the resonance shift. Beams 3 and 4 were still attached but not functional. Figure 3.6C and Figure 3.6D reveal more details on the *post mortem* analysis and the retrieved device. In Figure 3.6C, the location of the implanted probe during the cochlear dissection is shown. Figure 3.6D illustrates the condition of the PIAT right after the cochlea dissection. In Figure 3.6D, it shows that Beams 1 and 2 were intact while Beams 3 and 4 were significantly bent. Beam 4 was found buried in the muscle plug used to seal the cochleostomy. The *ex vivo* test and *post mortem* analysis revealed that Beam 1 and 2 were certainly operational during the entire *in vivo* test. This is in line with the elevated measured voltage response near the resonances of Beams 1 and 2. It is, however, unclear when Beams 3 and 4 were damaged.

We considered the possibility that the CM could potentially contaminate the measured *in vivo* voltage, but further measurements indicated the PIAT was not affected by the CM. Fridberger et al.[90] found that the electrical potential in the organ of Corti in the base of a very healthy animal could be as high as around 1 mV (7-22 kHz) in response to a 80 dB input stimulus. Our CM levels should be lower because of the damage to the cochlea from the implant surgery (Auditory Brainstem Responses confirmed the hearing threshold was elevated, as shown in Supplementary Materials). To test for CM contamination, we performed *in vitro* experiments and tested the response of the PIAT when a pure tone sinusoidal signal of 1 mV (1-10 kHz) was applied to an electrode submerged in a saline-filled dish 5 cm away from the PIAT. The output from the PIAT was recorded using the same lock-in amplifier as in the *in vivo* experiments. The largest signal detected due to this contamination signal was 0.3 μV, which was near the *in vivo* noise level (0.2 μV in the 1-10 kHz frequency range), but below the sensed signals (2.8-79.7 μV in the 1-10 kHz frequency range). Therefore, the sensed signal was unaffected by the CM.

3.2.5 Additional *In Vivo* Tests

In additional to the in vivo test presented above, three other tests were conducted. These four probes were labeled as Probe 1, 2, 3, and 4 based on the implantation dates. Just like the one that was demonstrated above (Probe 3), the functionality of the PIAT probes were tested in the benchtop via actuation tests before the implantation. While implanted in the living cochleae of guinea pigs, the *in vivo* sensed voltage readouts from PIATs were recorded in response to acoustic stimuli. The output voltages recorded from all four *in vivo* experiments were normalized to the levels expected due to the 110 dB SPL excitation and reported in the Figure 3.2.5. These four probes have different geometries, resonance frequencies, and *in vivo* impedance as noted in Table 3.2. Therefore, these probes were expected to have different responses *in vivo*. Generally, a lower parallel parasitic capacitance and a higher parallel parasitic resistance would produce a higher sensitivity. With such a trend, we would expect the test presented above (Probe 3) to have the highest overall response in Probe 1 to have the lowest. The measured *in vivo* frequency responses follow the expectation. The acoustic delay derived from phase slope all agrees with the acoustic delay from speaker to the PIAT. Probe 1 is from a pilot study [57] and does not show prominent peaks. Probe 2 has peaks between 8-14 kHz and 15-18 kHz, corresponding to the underwater resonance frequencies of Beams 1, 3, and 4. As reported in the previous sections in detail, Probe 3 has peaks between 1-9 kHz, corresponding to the underwater resonance frequencies of Beams 1 and 2. Probe 4 has peaks between 11-14 kHz and 15-20 kHz, corresponding to the underwater resonant frequencies of Beams 1 and 2.

The detailed tests of the Probe 1 is reported in [57]. Like Probe 3 reported previously, Probe 2 and Probe 4 have four 0.7 μm + 1.5 μm AlN bimorph cantilevers with the coating conditions detailed in Table 3.2. The in-air and in-water benchtop actuation tests and *in vivo* tests of the Probe 2 are shown in Figure 3.2.5. The animal used for Probe 2 was not deafened and the Probe 2 was implanted in the left

	In-water resonances f_r (kHz)	In vivo device and parasitic impedance @ 1kHz	Coating condition
Probe 1	24, 25, 30, 36	C_d=40 pF, C_p=110 pF, R_p =0.1 MΩ	Not coated
Probe 2	16, 19, 22, 25	C_d=28 pF, C_p=72 pF, R_p =2 MΩ	2 μm parylene, 50nm Al2O3
Probe 3	6, 7, 10, 14	C_d=38 pF, C_p=3 pF, R_p=10 MΩ	2 μm parylene, 50nm Al2O3
Probe 4	12, 14, 16, 18	C_d=28 pF, C_p=100 pF, R_p=3 MΩ	1 μm parylene, no Al2O3

Table 3.2: PIAT probes parameters for all four *in vivo* experiments, including in-water resonant frequencies, *in vivo* device impedance measured at 1 kHz, and water-proof coating condition.

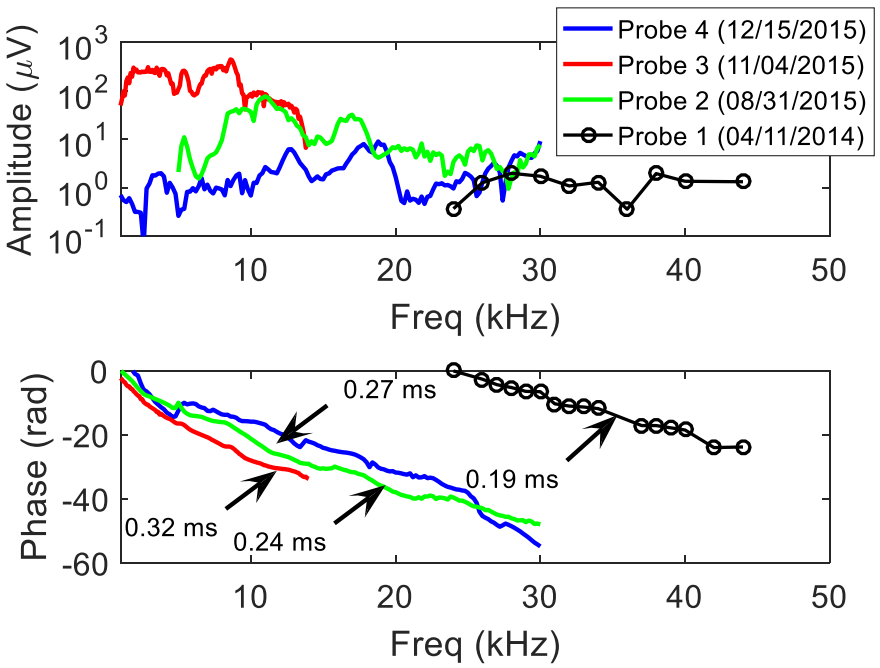

Figure 3.7: All four *in vivo* frequency responses with input normalized to 110 dB SPL. Each response is above the measurement noise of the experiment.

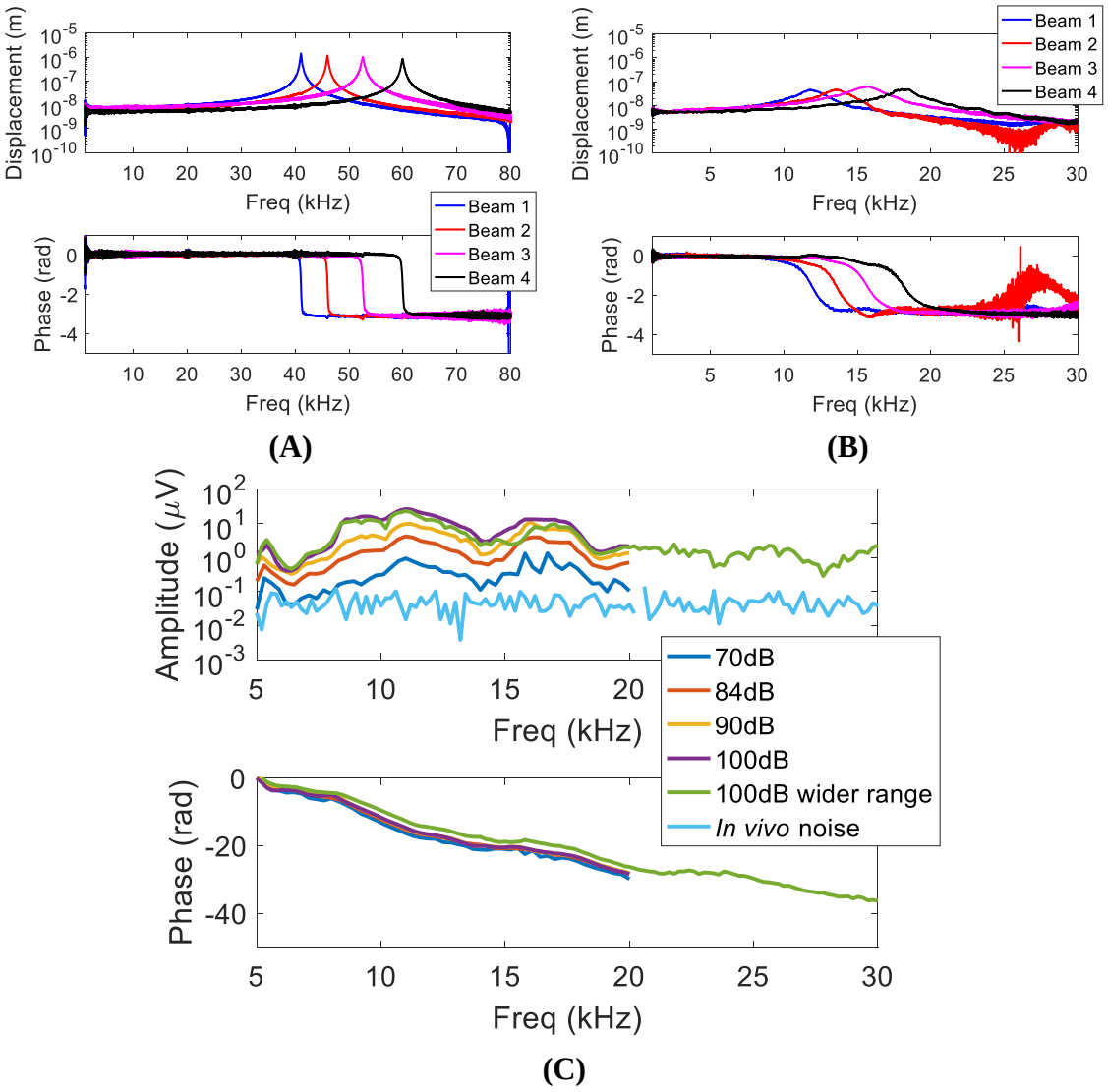

Figure 3.8: Additional *in vivo* testing results (Probe 2) (A) In air actuation testing. (B) In water actuation testing. (C) In vivo sensing response with 70 100 dB SPL external acoustic input.

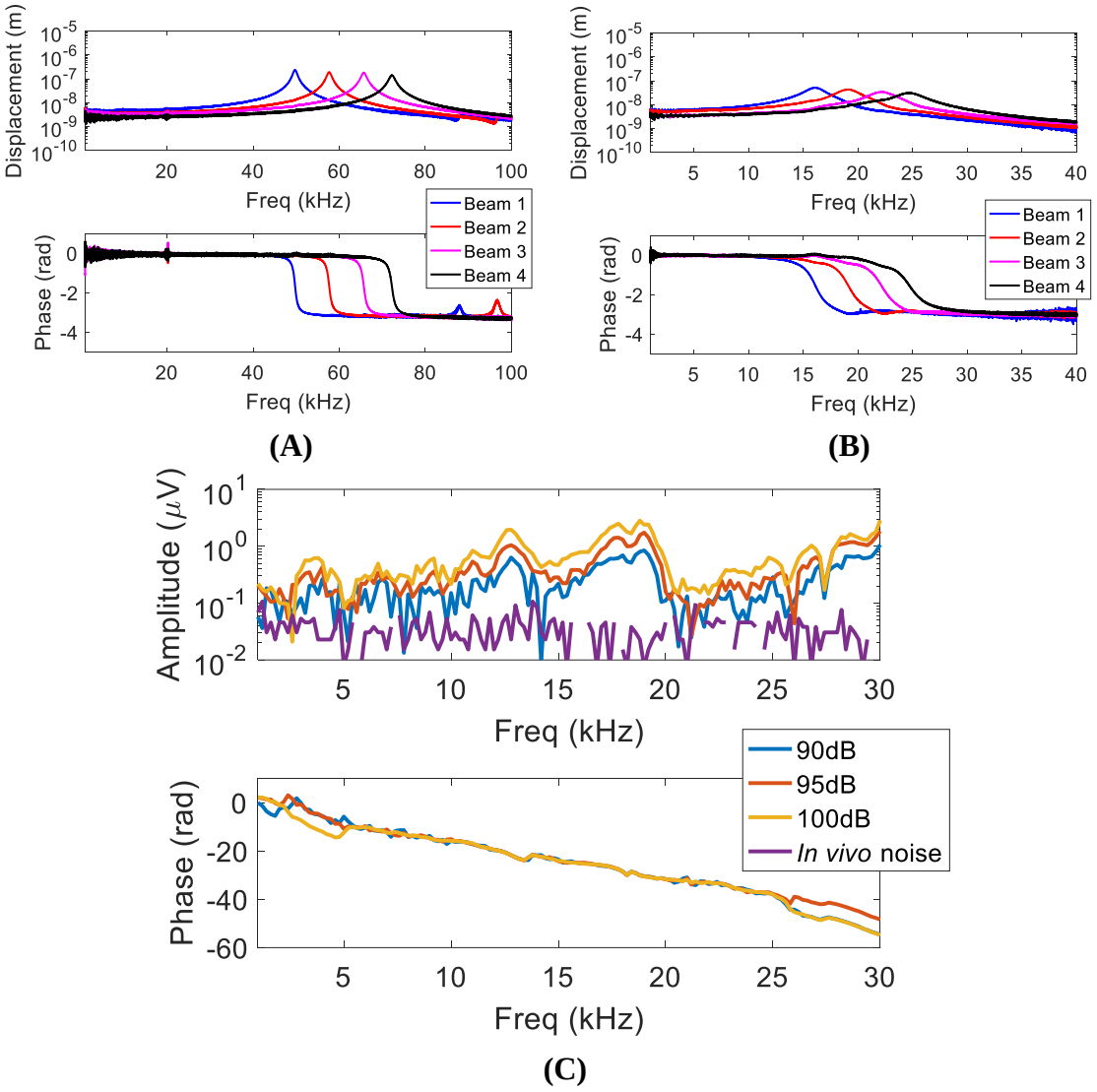

Figure 3.9: Additional *in vivo* testing results (Probe 4). (A) In air actuation testing. (B) In water actuation testing. (C) In vivo sensing response with 90 100 dB SPL external acoustic input.

ear. The voltage readouts in response to 70-100 dB SPL were recorded and shown in Figure 3.2.5C. The in-air and in-water benchtop actuation tests and *in vivo* tests of the Probe 4 are shown in Figure 3.2.5. For Probe 4, a combination of furosemide and kanamycin was used to deafen both ears and a PIAT was implanted in the left ear 8 days later. The voltage readouts in response to 90-100 dB SPL were recorded and shown in Figure 3.2.5C. For this Probe 4, a 50 μm diameter Pt wire was attached to the Probe and anchored at the tip of the probe with conductive epoxy, forming a electrode. After the *in vivo* sensing tests, While still implanted in the cochlea, a monophasic 25 μs single pulse stimuli with varying current amplitude was sent to the Electrode through a Pt wire attached to the Probe 4. The electrically evoked auditory brain stem response (EABR) was recorded. The EABR threshold (defined as the lowest level at which there was a repeatable positive (P) wave with a P-N difference of 0.25 μA) of 220 μA was recognized. It shows that we can incorporate the stimulating electrode with the sound sensor all inside a living cochlea. This is presented in [75]. In the future, we can use the sensed signal to stimulating the nerve directly all *in vivo*.

3.3 Discussion

We have shown that a fully implantable PIAT that has the capability to read out the voltage in a living cochlea in response to external acoustic excitation can be fabricated using MEMS technology. Because the intracochlear pressure signals are expected to be higher than those outside the ear [21, 22, 23] and certainly higher than those reaching a subcutaneous microphone, the PIAT has the potential to improve a fully implantable cochlear implant. We found that the transfer function between the applied ear canal acoustic pressure and the voltage output from the PIAT measured in the living cochlea fell in the range 1.2-71.0 μV/Pa (computed from results presented in Figure 3.6D) while the PIAT voltage to pressure ratio measured during

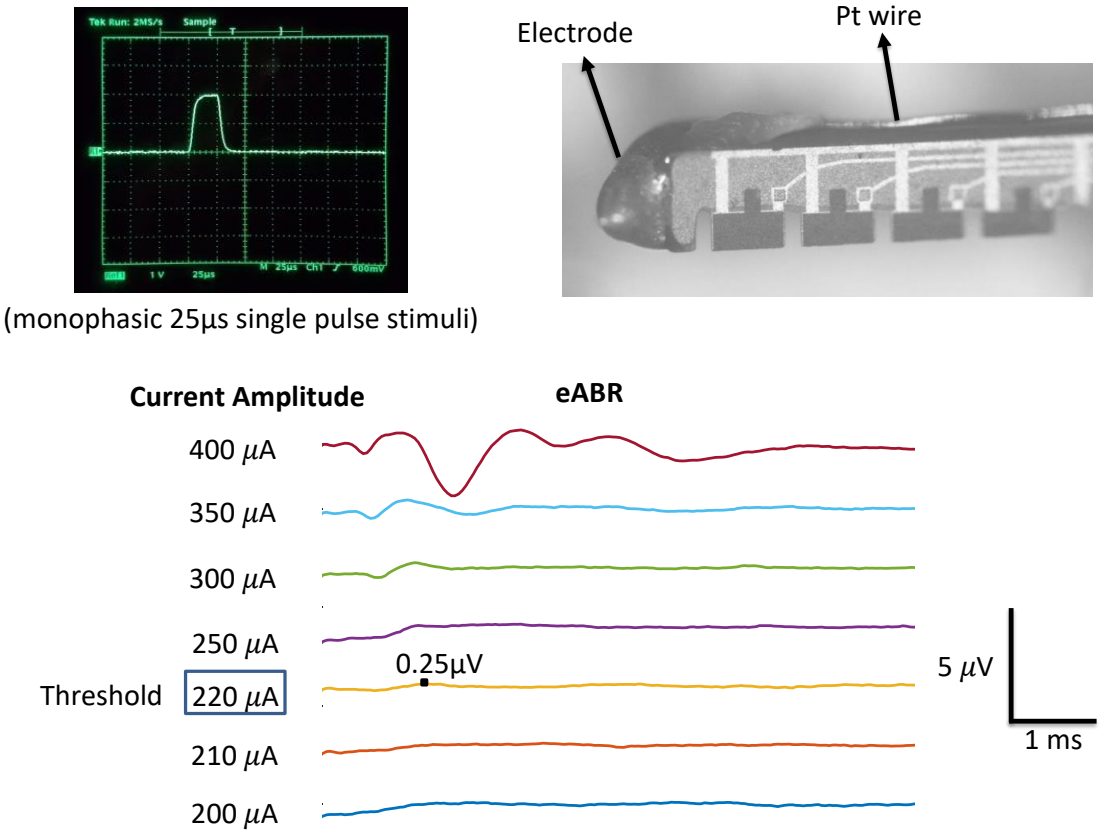

Figure 3.10: EABR testing for Probe 4. A monophasic 25 μs single pulse stimuli with varying current amplitude was sent to the Electrode through a Pt wire attached to the Probe 4. The EABR was recorded. The EABR threshold of 220 μA was recognized.

the benchtop experiment ranged from 0.05-12.6 μV/Pa (from Figure 3.4B). This result indicates that the acoustic pressure inside the cochlea is higher than outside the cochlea. This result is in line with previous measurements [21, 22, 23]. All recorded *in vivo* voltage responses were above the noise and unaffected by the crosstalk from the loudspeaker, electrical interference, or the cochlear microphonic. The ex vivo actuation test confirmed that the PIAT probe was still partially functional after the in vivo testing. This indicates the robustness of the PIAT in spite of the potentially destructive surgeries. Taken as a whole, we successfully measured voltage readout with the PIAT implanted in the living cochlea and have provided important steps (for both manufacture and implantation) towards utilizing the intracochlear acoustic signal for future fully implantable cochlear implant (FICI).

Potential uses for the technology developed in this paper include the use as a sensor inside the cochlea. For patients with functioning middle ears, a PIAT could eliminate the need for an external microphone as in a traditional CI. An internal sensor would enhance the ease of use, improve the appearance, and leverage the $\sim$20 dB increase in the intracochlear versus extracochlear pressure (depending on the PIAT location and stimulus frequency [22, 96, 97]). Besides, subcutaneous microphones tend to pick up more noises (such as users scratching their heads), compared to intracochlear transducers. Because of these potential advantages, such an approach has been proposed and pursued by other groups (e.g., Inaoka et al.[32], Jang et al.[37], and Mukherjee et al.[98]). Because we have demonstrated the functionality of the PIAT as an actuator in the actuation tests, another prosthetic application of this technology includes the use of the piezoelectric MEMS transducer in reverse as a receiver/actuator (intracochlear speaker) for a hearing aid or as a hybrid electro-acoustic stimulator for a cochlear implant. Presently, the simulation is extracochlear, either outside the tympanic membrane or in the middle ear [99, 100]. The piezoelectric bimorph technology developed here (modified to improve its radiation efficiency)

could be placed inside the cochlea to generate sound. Luo et al.[79, 80] recently developed an intracochlear PZT actuator that can evoke auditory brainstem response by generating acoustic signals inside a cochlea, an exciting proof-of-concept for this approach. Compared to Luo et al. design, the PIAT is lead-free, smaller, and produces a larger displacement. Finally, the PIAT can be used either as a sensor or as a generator of sound for inner ear mechanics measurements for basic science study [22]. In actuator mode, these devices could be used to produce a well-defined, focal disturbance inside the cochlea. Such a controlled source, in combination with cochlear mechanics response measurement techniques (e.g., laser vibrometry, optical coherence tomography [101, 102] or otoacoustic measurements [103]) could lead to a better understanding of the genesis of different types of otoacoustic emissions and their relation to cochlear function. Other potential applications of this technology include sensing and actuation for many biomedical applications such as cardiovascular and urological diagnostic procedures, surgical procedures and monitoring of invasive treatments. Moreover, the multi-resonant characteristics could also be used as a multi-resonant microphone or hydrophone, or even a broadband sound silencer [81, 82].

Since the PIAT is completely implantable, it could improve issues traditional CI have including high power consumption, as well as cosmetic and safety issues. In addition, because the PIAT uses the MEMS techniques, which could enable mass production, it would reduce costs [76]. The PIAT has the potential to provide a better and more affordable front end of a completely implantable cochlear implant. With a better design of the amplifier circuit and an optimization of the MEMS sensor, potential improvements can still be made. In particular, acoustically shielding the back of the plates should improve sensitivity significantly, especially in a fluid environment. In the meantime, decreasing the distance to the amplifier would reduce the parasitics. In addition, the rigid straight silicon backbone, which prevents deeper insertion of the PIAT into the cochlea, could be made smaller and flexible. Future

generations of these devices could resolve these issues. In addition, Zhao et al.[75] incorporated an intracochlear electrode with the PIAT and elicited EABR in the guinea pig. With a better PIAT, the sensed signal should be able to evoke the auditory brainstem responses directly, thus achieving the completely implantable cochlear prosthesis.

CHAPTER IV

Ultraminiature Diaphragm Transducer Designed for Intracochlear and Cadiovascular Applications

The AlN xylophone transducer described in the previous chapters works well as multi-resonance sensors and actuators around their resonances. However, if we choose to use it as a sensor, the sensitivity is significantly decreased in the low frequency because the acoustic pressure diffracts around the cantilever and cancels out the excitation. To solve this issue and improve the device performance, the ultraminiature AlN diaphragm transducer with a back cavity is presented. The transducer consists of a unimorph diaphragm with the electrode size optimized to achieve the MDP or input referred noise (IRN), which is defined as IRN = $20\log_{10}(\frac{\text{MDP}}{20\ \mu\text{Pa}})$. The back cavity is encapsulated and filled with air at atmosphere pressure. In this way, there would be no pressure cancellation due to diffraction to reduce the sensitivity. Compared to the xylophone transducer or PIAT, the diaphragm transducer is even smaller, and at the same time, they has a lower MDP. The transducer is designed to be able function directly exposed to air or water based fluid. Because of these advantages, it can be used as an intracochlear microphone, or cardiovascular dynamic pressure sensor.

4.1 Existing miniature acoustic sensor

4.1.1 Intracochlear acoustic sensor

Recently, a PVDF based fully implantable intracochlear microphone [26] and an intracochlear acoustic receiver developed using a implanted microtube coupled to a MEMS microphone [25] provided promising paths to achieve fully implanted cochlear implants. The xylophone transducer described in the previous chapters used AlN as the sensing material, introducing a potentially better method to develop the implantable sensors for the fully implantable cochlear implants. In this study, we develop a diaphragm transducer backed with a air cavity to improve the sensitivity and lower the IRN. The IRN and MDP are developed to be much smaller than the existing intracochlear acoustic sensors [25, 26], while using a smaller diaphragm area.

4.1.2 Miniature piezoelectric acoustic sensors

Several piezoelectric diaphragm microphones or hydrophones have been developed in the past [104, 105, 46, 106]. These sensors are optimized to achieve a high sensitivity and low MDP. However, they are too large to be implanted. In this study, we are using similar design concept. We are reducing the diaphragm areas and MEMS chip size, while targeting to achieve similar and potentially smaller MDP. FEA model was used to help with the design. Details of the design, modeling, and optimization are discussed in the following section.

4.1.3 MEMS cardiovascular pressure sensors

Because the diaphragm sensor has high performance even in the low frequency, it can also be used for cardiovascular applications. For cardiovascular applications, the frequency of interests usually is less than 200 Hz, the pressure range is 6.7-24 kPa (50-180 mmHg), and the pressure resolution is about 133 Pa (1 mmHg) [107]. These

are different than hearing applications. Nonetheless, the design of the diaphragm transducer is targeted to also meet these requirements. Cardiovascular pressure sensors were developed using MEMS technologies in the past [43, 108, 109, 107, 110]. More recently, there are even some MEMS pressure sensors incorporated in heart monitoring systems that have been clinical proven (like CardioMEMS (CardioMEMS HF system, St. Jude Medical, USA)). Unlike most MEMS cardiovascular pressure sensor that are capacitive, this diaphragm is piezoelectric. As discussed before, the advantages include no DC bias required, can work directly exposed to fluid, and low noise, which would provide an interesting different approach for cardiovascular applications.

4.2 Design and Modeling

4.2.1 Design Figure of Merit

This diaphragm acoustic transducer consists of a deformable piezoelectric diaphragm, backed up by a cavity filled with air. We aim to achieve a low MDP or IRN, while using a small area. Using the equivalent lumped-circuit model method for the acoustic transducer [111, 61, 63], the MDP is described as below [63]

$$\mathrm{MDP}^2 = \frac{(\frac{1}{C_{ad}} + \frac{1}{C_{ab}})}{\Phi^2} \cdot C_{eb} \cdot \frac{4k_bT\tan\delta}{\omega} \tag{4.1}$$

where C_{ad} is the acoustical compliance of deformable structure, C_{ab} is the acoustical compliance of back cavity volume, Φ is the transformer ratio, C_{eb} is the device capacitance, k_b is the Boltzmann constant, T is the temperature, $\tan\delta$ is the dielectric loss tangent of the piezoelectric material, and ω is the angular frequency. With the coupling coefficient $k^2 = \Phi^2\frac{C_{ad}}{C_{eb}}$ and the ratio r defined as $r = \frac{C_{ad}}{C_{ab}}$, Equation 4.1 can be rearranged to be

$$\text{MDP}^2 = \frac{4k_bT\tan\delta(r+1)^2}{\omega k^2 C_{ad}} \tag{4.2}$$

In Equation 4.2, k_b, T, and $\tan\delta$ are constants, and k only depends on dimensionless geometric design and material properties [63]. Therefore, with a given acoustical compliance of the deformable structure, MDP is the lowest when r is approaching 0 ($C_{ab} \gg C_{ad}$). This means the back cavity is either very compliant [104, 46, 112] or vacuum sealed [106]. With the target size and material used in this study, C_{ab} is $\sim$ 100 times higher than C_{ad} or more.

4.2.2 Design and Optimization

Figure 4.1 illustrates the concept of the diaphragm transducer. Figure 4.1A shows the transducer consists of a diaphragm with an encapsulated back cavity filled with air. The electrode pads next to the diaphragm are for external electrical access and

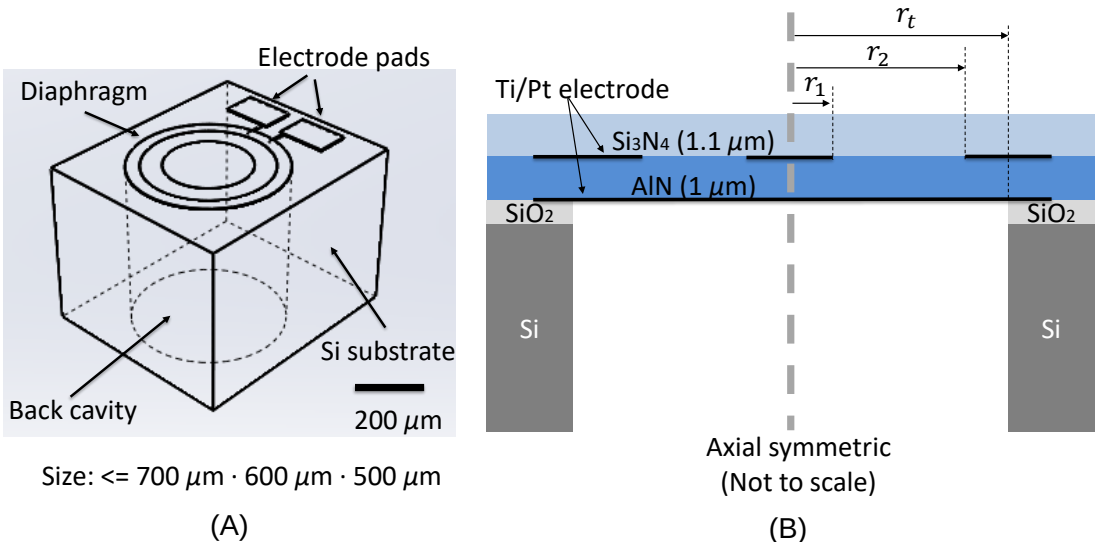

Figure 4.1: The diaphragm transducer design concept. (A) The 3D design shows the transducer consists of a diaphragm and an encapsulated back cavity. (B) The side view of the unimorph diaphragm, consisting of the AlN and Si_3N_4. r_1 is the radius of the inner circle, r_1 is the inner radius of the outer ring, and r_t is the total radius.

wire-bonding. The whole transducer has a size of less than 700·600·500 μm^3 (or 0.21 mm^3). When the acoustic pressure deflects the diaphragm, the piezoelectric voltages created in the the center region and the outer ring region are in the opposite signs for the first mode. To avoid the voltage canceling, the electrode must be broken in the middle, forming an inner circle and an outer ring. The sizes of the electrode lengths are optimized using a 2D axisymmetrical FEA model using COMSOL Multiphysics to achieve the lowest MDP. The material properties are chosen from the COMSOL material library [66], except d_{31}= -2.51 pm/V from Xu et al. [106] The thicknesses of AlN and Si_3N_4 are chosen to be 1 μm and 1.1 μm respectively to set the neutral axis of this unimorph at the AlN/Si_3N_4 interface for maximum voltage output. The side view of the diaphragm is shown in Figure 4.1B. Radius range in 100-275 μm for both one-electrode design (only uses the outer ring region), and two-electrode design (uses both the center and outer region with the polarity flipped) are designed using the FEA model.

The larger the diaphragm diameter is, the lower the IRN of the senor is. But the diaphragm is more susceptible to break due to external loading or AlN residual stress. In this work, the diaphragm radius is set to be within 100-275 μm for a reasonable SNR and also to make sure the diaphragm would not break due to residual stress or normal external loading. Because the total radius r_t is fixed, the best SNR can be optimized by changing the radius of the inner circle r_1, and outer ring radius r_2. The sensitivity is also calculated to make sure the level is within a reasonable range that can be pick up by electronics. An example of the optimization calculation for the sensitivity and the IRN with $r_t = 200$ μm is shown in Figure 4.2.

FEA simulation suggests the outer ring is more efficient to produce a lower IRN sensor than the inner circle. Therefore, a second design with only the outer ring is also designed. By dropping the inner circle, the IRN would be increased by $\sim$5 dB, and the sensitivity will be decreased by a factor of $\sim$2, as suggested by simulation

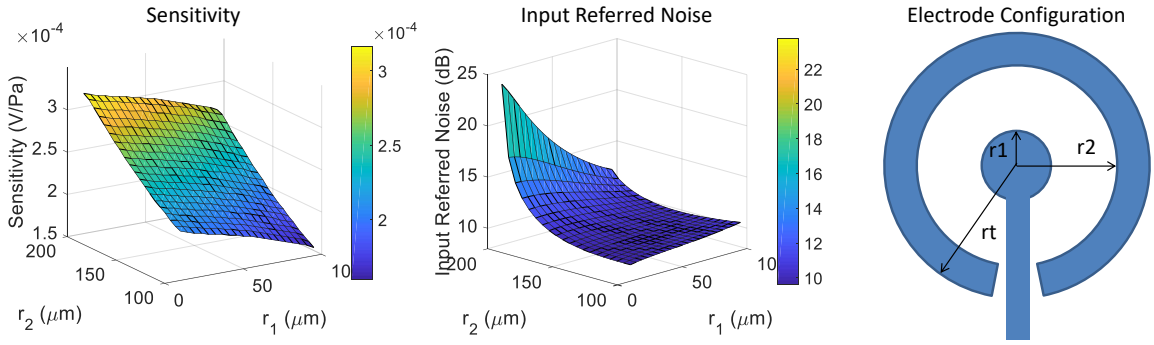

Figure 4.2: An example of the optimization calculation for the sensitivity and IRN for a $r_t = 200$ μm transducer with two-electrode design.

results. However, the routing and waterproofing is easier, because the polarity does not need to be flipped. An example of the optimization calculation of this design with $r_t = 200$ μm is shown in Figure 4.3.

With the same diaphragm area, one can design a single large diaphragm or several smaller diaphragms connected in series or parallel. It has been show that having N (N is the number of diaphragms) diaphragms (each has a MDP_1) in parallel or series, the $MDP_N = N^{-\frac{1}{2}} \cdot MDP_1$ [61], while having one diaphragm $Area_N = N \cdot Area_1$, Equation 4.2 indicates that $MDP'_N = N^{-\frac{3}{2}} \cdot MDP_1$. Therefore, it is more efficient to have one large diaphragm than having several smaller diaphragms connected in parallel or series.

After the optimization, the frequency response of the transducer is calculated, which would determine the sensitivity, IRN, and resonance frequency f_r both in air and in water. The complete specifications for these two designs are tabulated in Table 4.1 and Table 4.2. This design was also discussed in [112].

The residual stress in the AlN would impact the device performance and could even potentially break the device. Therefore, it needs to be considered. FEA model using COMSOL is built to study the residual stress's effect on sensitivity and input

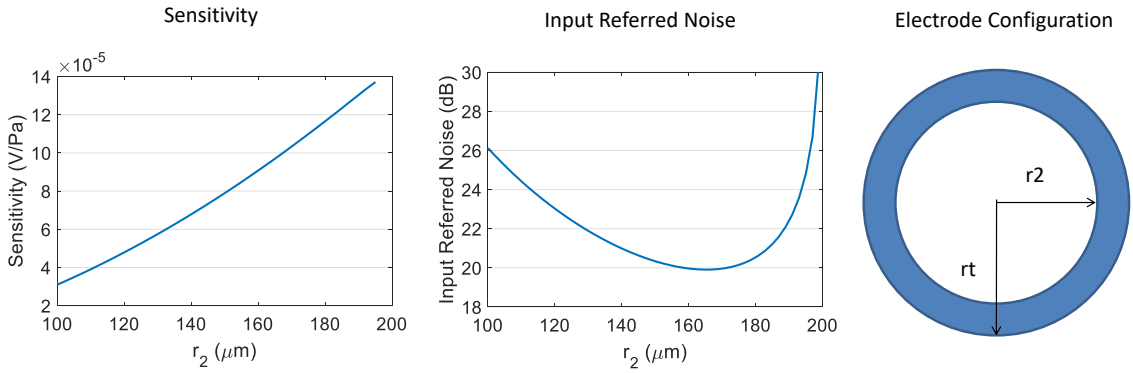

Figure 4.3: An example of the optimization calculation for the sensitivity and IRN for a $r_t = 200$ μm transducer with one-electrode design.

Total radius r_t	r_1	r_2	Sensitivity	MDP (100 Hz)	MDP (1 kHz)	f_r in air	f_r in water
100 μm	57 μm	83 μm	53 (μV/Pa)	3.30 mPa	1.04 mPa	979 kHz	300 kHz
125 μm	70 μm	103 μm	58 (μV/Pa)	1.68 mPa	0.53 mPa	627 kHz	197 kHz
150 μm	80 μm	125 μm	120 (μV/Pa)	0.98 mPa	0.31 mPa	435 kHz	128 kHz
175 μm	95 μm	145 μm	160 (μV/Pa)	0.61 mPa	0.19 mPa	320 kHz	90 kHz
200 μm	110 μm	165 μm	205 (μV/Pa)	0.41 mPa	0.13 mPa	244 kHz	66 kHz
225 μm	125 μm	185 μm	267 (μV/Pa)	0.29 mPa	0.09 mPa	193 kHz	51 kHz
250 μm	140 μm	205 μm	322 (μV/Pa)	0.21 mPa	0.07 mPa	157 kHz	33 kHz
275 μm	115 μm	225 μm	396 (μV/Pa)	0.16 mPa	0.05 mPa	129 kHz	26 kHz

Table 4.1: Design specifications for the diaphragm transducer with two-electrode design.

Total radius r_t	r_2	Sensitivity	MDP (100 Hz)	MDP (1 kHz)	f_r in air	f_r in water
100 μm	83 μm	24 (μV/Pa)	5.09 mPa	1.61 mPa	979 kHz	300 kHz
125 μm	103 μm	37 (μV/Pa)	2.59 mPa	0.82 mPa	627 kHz	197 kHz
150 μm	125 μm	56 (μV/Pa)	1.49 mPa	0.47 mPa	435 kHz	128 kHz
175 μm	145 μm	74 (μV/Pa)	0.94 mPa	0.30 mPa	320 kHz	90 kHz
200 μm	165 μm	98 (μV/Pa)	0.63 mPa	0.20 mPa	244 kHz	66 kHz
225 μm	185 μm	175 (μV/Pa)	0.44 mPa	0.14 mPa	193 kHz	51 kHz
250 μm	205 μm	150 (μV/Pa)	0.32 mPa	0.10 mPa	157 kHz	33 kHz
275 μm	225 μm	180 (μV/Pa)	0.24 mPa	0.08 mPa	129 kHz	26 kHz

Table 4.2: Design specifications for the diaphragm transducer with one-electrode design.

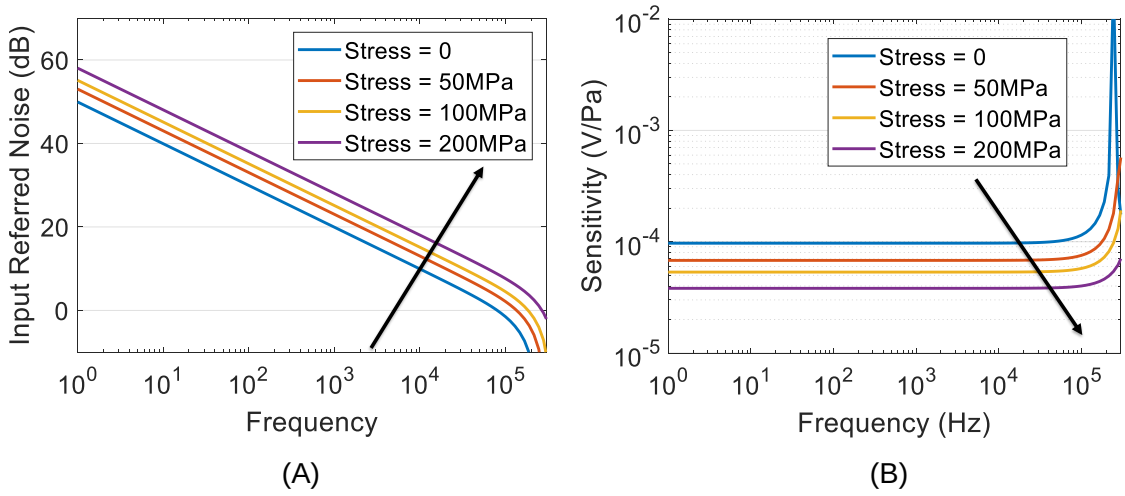

Figure 4.4: AlN residual stress's effect on the (A) IRN and (B) the sensitivity. The arrow indicates the trend of the increasing stress.

referred noise. As can be seen in Figure 4.4, with the residual stress increases, the IRN increases and the sensitivity decreases. A ∼200 MPa residual stress would make the device ∼ 10 dB worse.

4.3 Fabrication

The device was fabricated using the MEMS process summarized in Figure 4.5. (A) It started with a 4 inch p-type Si (100) substrate coated with 2 μm of wet thermal oxide. 15/50 nm Ti/Pt bottom electrode layer (Lab 18-2, Kurt J. Lesker Company, USA) was deposited and patterned. Then, 1 μm AlN was deposited at OEM Group Inc. (OEM Group Inc, USA). The wafer-level residual stress of the AlN was measured and modeled to be ∼350 MPa. (B) A second 15/50 nm Ti/Pt electrode layer (Lab 18-2, Kurt J. Lesker Company, USA) was deposited and patterned. A low stress PECVD Si_3N_4 was then deposited at 200 °C using GSI PECVD tool. The vias to the middle and bottom electrode was etched using plasma etch (9400, LAM Research Corporation, USA) for Si_3N_4, and a combination of a Cl-based dry etch

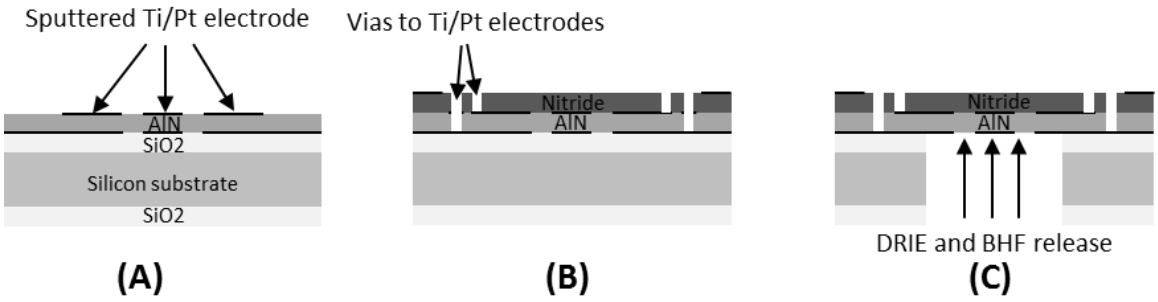

Figure 4.5: MEMS fabrication process for the diaphragm transducer.

(9400, LAM Research Corporation, USA) and a heated (50 °C) KOH-based etch (AZ 400K, Clariant, USA). (C) Finally, sputtered Cr/Au formed the electrode pads for bonding. The back cavity defined using a through-wafer deep reactive ion etch (DRIE) (STS Pegasus 4, SPTS Technologies Ltd., USA), followed by a plasma oxide etch (glass etcher, SPTS Technologies Ltd., USA) to release the cantilevers.

The fabricated devices are shown in Figure 4.6. Once the devices were fabricated, impedance was checked using LCR meter (E4980A, Agilent, USA). The transducer was then mounted on a printed circuit board (PCB) with double-sided tape (3M, scotch double sided tape, USA), followed by krazy glue (Krazy Glue, USA) to seal the back cavity. Wire-bonding was performed at Protoconnect (Protoconnect LLC, USA). Silicone was used to encapsulate the bond pads, wires, and bonding joints to make the device waterproof. A picture of the wire-bonded, silicone-encapsulated device is shown in Figure 4.7.

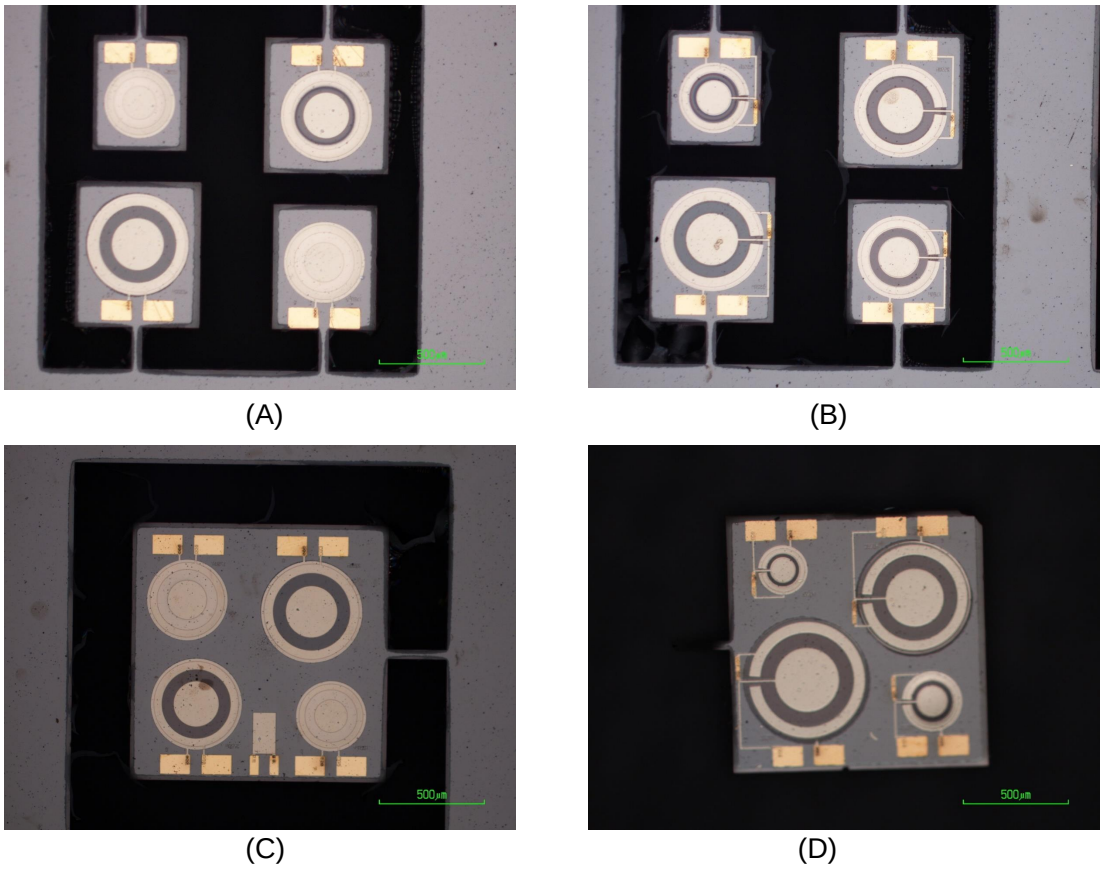

Figure 4.6: Fabricated diaphragm transducers. (A) The ring design (one electrode) transducer on a individual MEMS die (size $<$ 700·600·500 μm^3). (B) The flipped-polarity design (two electrodes) transducer on a individual MEMS die (size $<$ 700·600·500 μm^3). (C) Four ring design transducers on a MEMS die (size = 1200·1200·500 μm^3). (D) Four flipped-polarity design transducers on a MEMS die (size = 1200·1200·500 μm^3).

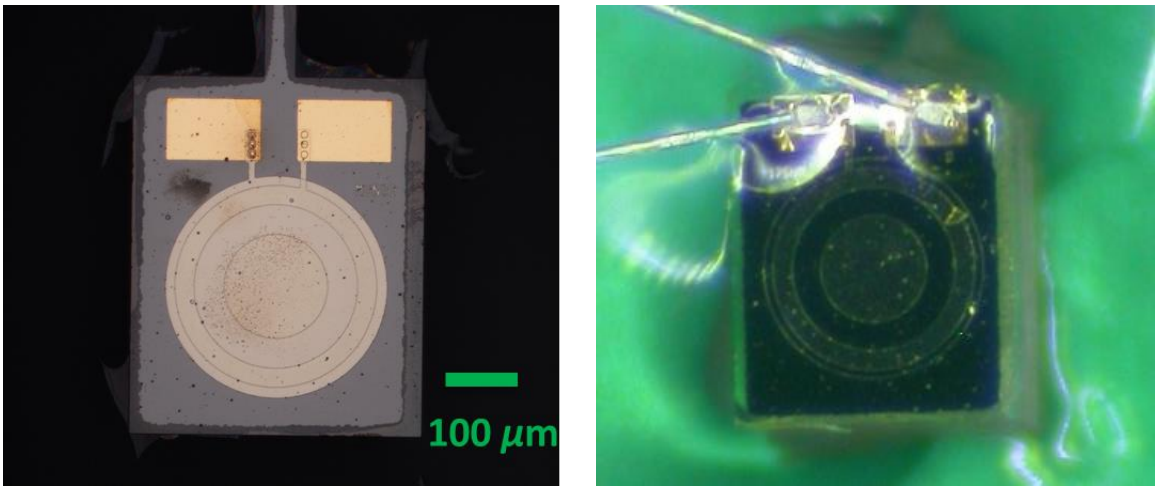

Figure 4.7: The fabricated diaphragm ring design transducer before and after the silicone encapsulation. The transducer has a radius of 175 μm on a individual MEMS die (size = 400·500·500 μm^3) was wire-bonded on a PCB. The bond pads (150·100 μm^2) and wires were encapsulated with silicone, and the diaphragm was exposed.

4.4 In-air and in-water actuation test

To demonstrate the functionality of the transducer, a ring design transducer with a radius of 175 μm on a individual MEMS die (size = 400·500·500 μm^3) was tested. Once the transducer was wire-bonded, the actuation tests were performed using the methods detailed in the previous chapters. In short, the voltage was applied at the pads on the PCB using a probe station (LA-150 DC, Semiprobe, USA) with a goniometer (123-2890, Optosigma, France) to adjust the reflectiveness. A laser Doppler vibrometer (LDV; OFV-303, Polytec, USA) was used to measure the vibration at the center of the diaphragm. A pure tone sinusoidal 1 V signal was sent to the diaphragm transducer, with the frequency swept through 300-600 kHz to find the in-air resonances of the transducer. Then, a frequency response of the diaphragm vibration was measured by playing a 1 V chirp signal in 1-200 kHz. A drop of water was applied on the transducer for the in-water frequency response.

To fully understand the frequency behavior of the device, a FEA model was built

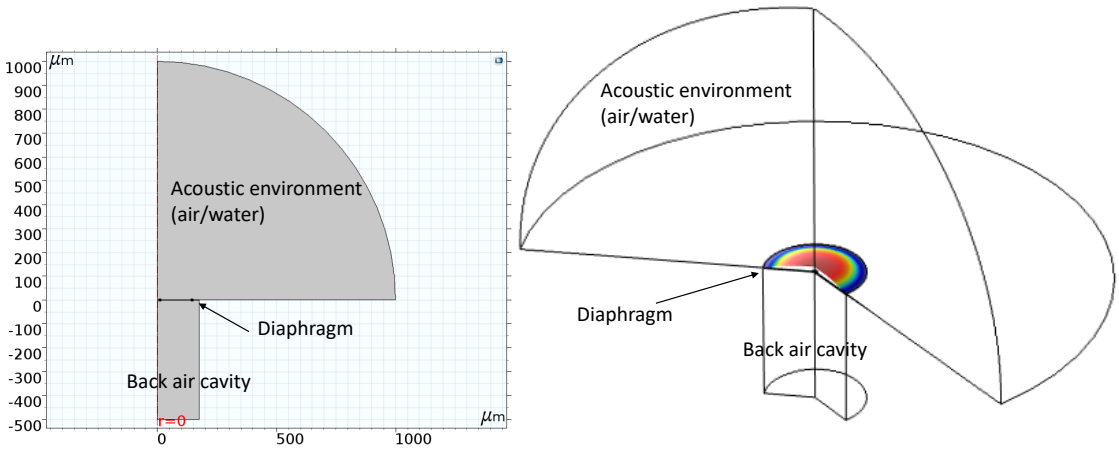

Figure 4.8: The FEA model geometry for the diaphragm transducer in air/water.

to analyze the actuation tests both in air and in water, using the methods detailed in the previous chapters. Figure 4.8 shows the geometry of the FEA model for this diaphragm transducer.

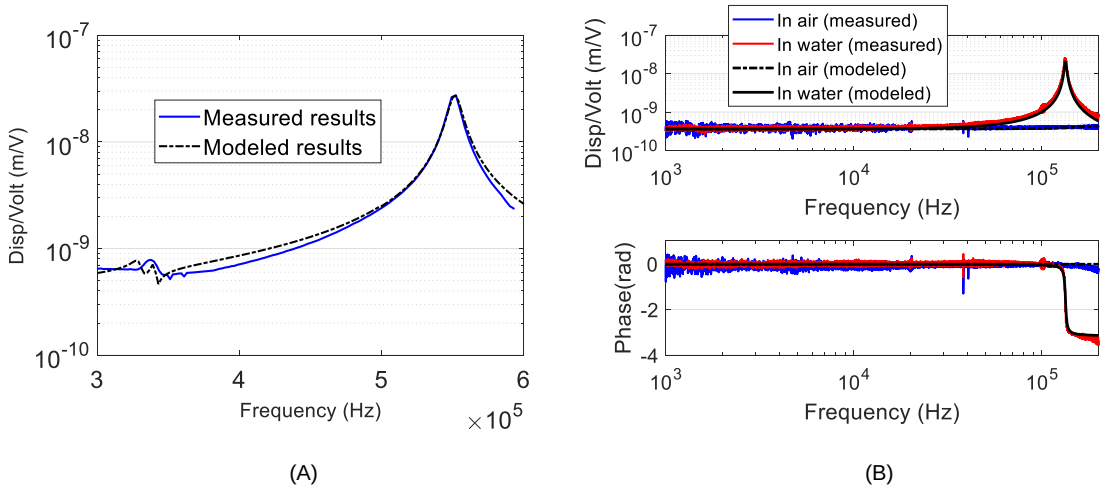

Figure 4.9: Diaphragm transducer actuation results. (A) Modeled and measured frequency sweep of the transducer in air in 300-600 kHz. (B) Modeled and measured frequency response of the transducer both in air and in water in 1-200 kHz.

The modeled and measured actuation results are shown in Figure 4.9. The modeling parameters d_{31} and residual stress of the AlN film was adjusted to compare with the measured in-air frequency sweep results reported in Figure 4.9A. With a d_{31} = -0.75 pm/V and a residual stress of 255 MPa, the modeling results and measured frequency sweep show a good match. The d_{31} was on the relatively low because of the low film quality. The modeling residual stress (255 MPa) is similar to the measured wafer-level residual stress (∼350 MPa), and the difference is understandable, because the local residual stress varies through the wafer. A small fluctuation around 343 kHz showed on both the measured and modeled results. This fluctuation was from the acoustic resonance of the back cavity, which indicated a good acoustic seal. Figure 4.9B shows the modeled and measured actuation frequency response both in air and

in water. In the FEA model, the diaphragm transducer parameters were kept the same, and only the acoustic properties were changed, based on the surrounding fluid media (air or water). The modeled results and measured results match very well for both the low frequency response (0.36 nm/V), and the in-water resonance frequency (133 kHz).

4.5 In-air sensing test

After verifying the transducer functionality using actuation results, sensing tests were conducted. An amplifier circuit was soldered on the PCB to buffer and amplify the signals using the JFET (2SK3372, Panasonic, Japan) and the operational amplifier (AD8655, Analog Devices Inc., USA). The amplification gain (42.25) was normalized and factored out for all the measurement and calculation reported in this study. Because the transducer had a higher noise in the low frequency range, in other words the transducer had a worse performance in low frequency range, this sensing test chose to focus on this low frequency bandwidth (10-1000 Hz) to demonstrate the functionality.

In-air sensing test was conducted by play the chirp acoustic excitation using a woofer (4" woofer 40-1022B, Radio Shack, USA) coupled to a one end of a 12 inch long (304.8 mm) PVC tube with closed end condition. The tube had an inner diameter of 2 inch (50.8 mm). A cap was 3D-printed to create a closed end boundary condition to boost the SPL output in the low frequency range. The cap had a hole for the reference microphone (2520, Larson Davis, USA), and a slot for the transducer on the PCB. The in-air sensing test setup was shown in Figure 4.10.

The modeled and measured in-air sensing testing results are shown in Figure 4.11. Figure 4.11A shows the frequency response (the transfer function between the MEMS transducer voltage output and the reference microphone pressure output). The measured sensitivity shows a flat sensitivity of -111 dBV/Pa (2.78 μV/Pa) in

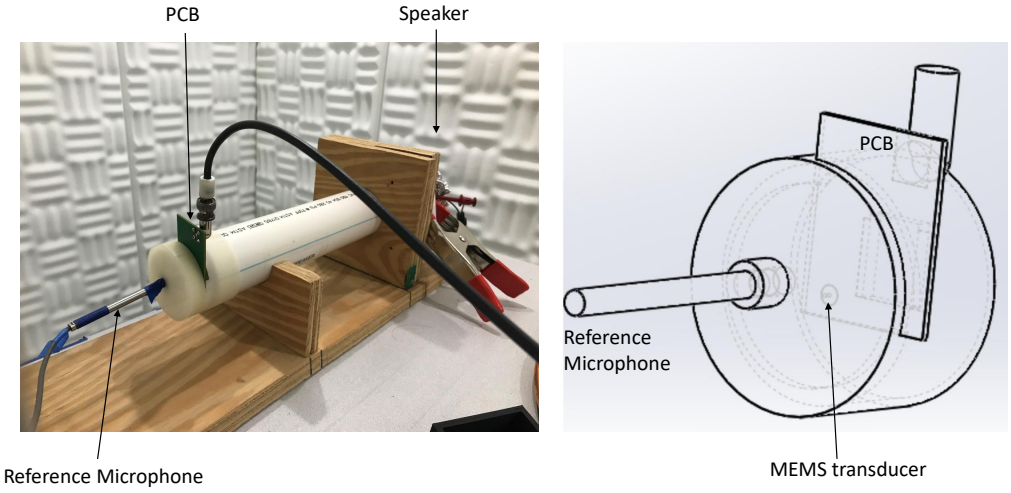

Figure 4.10: In-air sensing test setup.

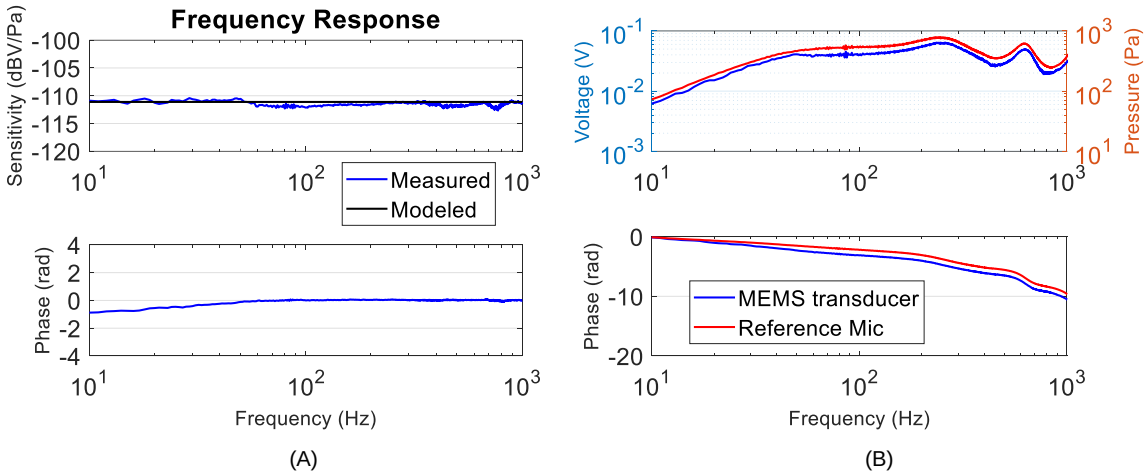

Figure 4.11: Modeled and measured sensing tests. (A) The frequency response of the MEMS transducer. The modeled sensitivity is -111 dBV/Pa (or 2.78 μV/Pa). (B) The measured MEMS transducer voltage output (blue), and the reference microphone pressure (red).

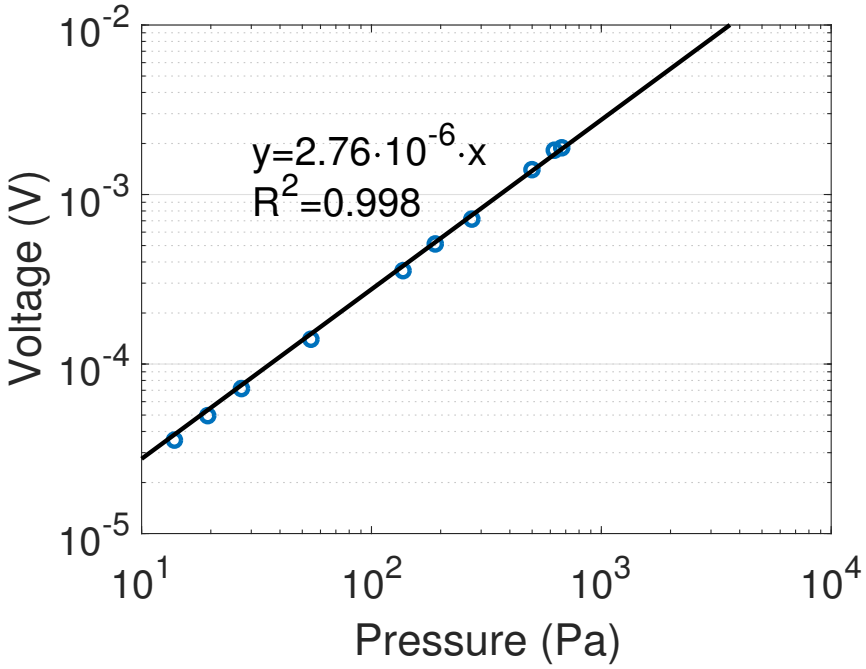

Figure 4.12: In-air linearity test at 1kHz.

10-1000 Hz, and it shows a great match with the modeling expectation within 1 dB. Figure 4.11B shows as measured voltage response (blue, left axis) from the MEMS transducer and the pressure response (red, right axis) from the MEMS reference microphone in this speaker/tube system.

In-air linearity test was conducted (Figure 4.12) by changing the input speaker voltage at 1 kHz to create different SPL input to the diaphragm transducer. The results showed a good linearity within 14-630 Pa. A slope of 2.76 μV/Pa with high $R^2 = 0.998$ was obtained by the linear curve fitting, which agrees with the sensitivity as measured from frequency response within an error of 1%.

4.6 In-water sensing test

Sensing test in water was conducted using a vibrating column of water method described in [113]. A 3 mL syringe (3mL Global Easy Glide Disposable Syringe, Dispense All, USA) was cut using a band saw, and glued on the PCB to create a

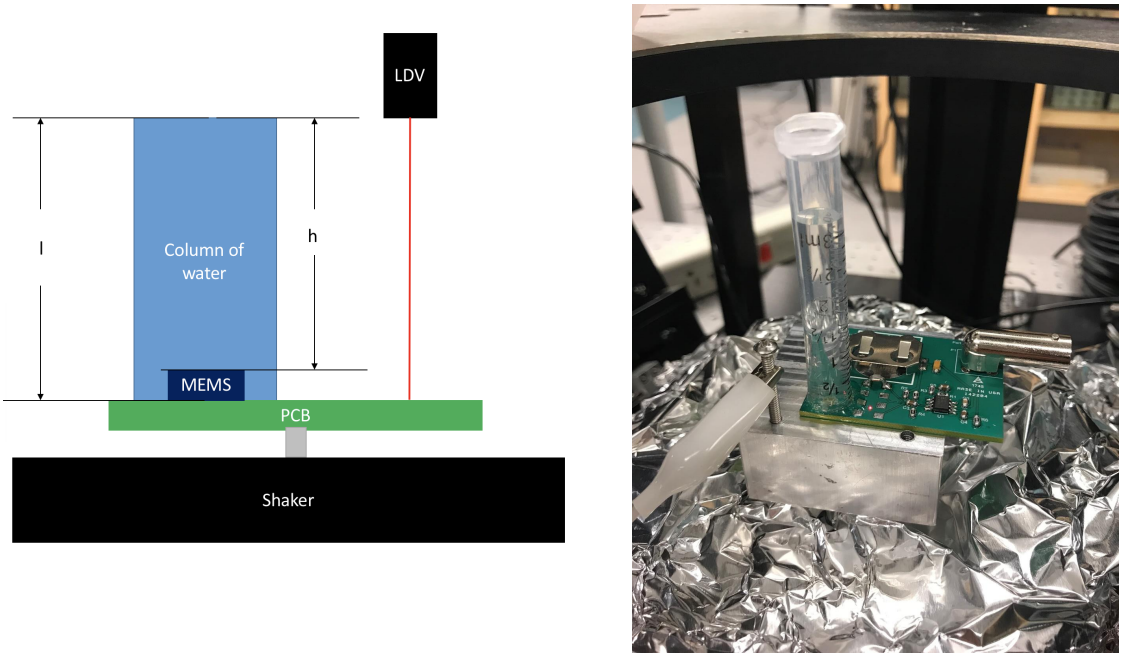

Figure 4.13: In-water sensing test setup.

column of water. Then the PCB was mounted on a aluminum cube coupled to a shaker. Aluminum foil was used to cover the shaker to shield the electromagnetic interference. LDV was used to measure the vibration of the PCB to calculate the pressure excitation on the transducer diaphragm. Figure 4.13 shows the in-water sensing setup.

Pressure excitation at the transducer was calculated using the equation $p_h = \rho h \ddot{x} \frac{sin(\omega h/c)}{(\omega h/c)cos(\omega l/c)}$ [113], where p_h is the pressure at the transducer, ρ is the density of the water, h is the distance from the water surface to the transducer, l is the total water column height, $\ddot{x}$ is the acceleration of the transducer (measured by LDV), and c is the sound speed in water.

The modeled and measured in-water sensing tests are shown in Figure 4.14. Both measured and modeled in-water sensitivity was the same as the in-air sensitivity even down to an ultra low frequency (10 Hz). It should be noted that the 10 Hz was limited by the testing setup (the shaker), not the diaphragm transducer. In reality,

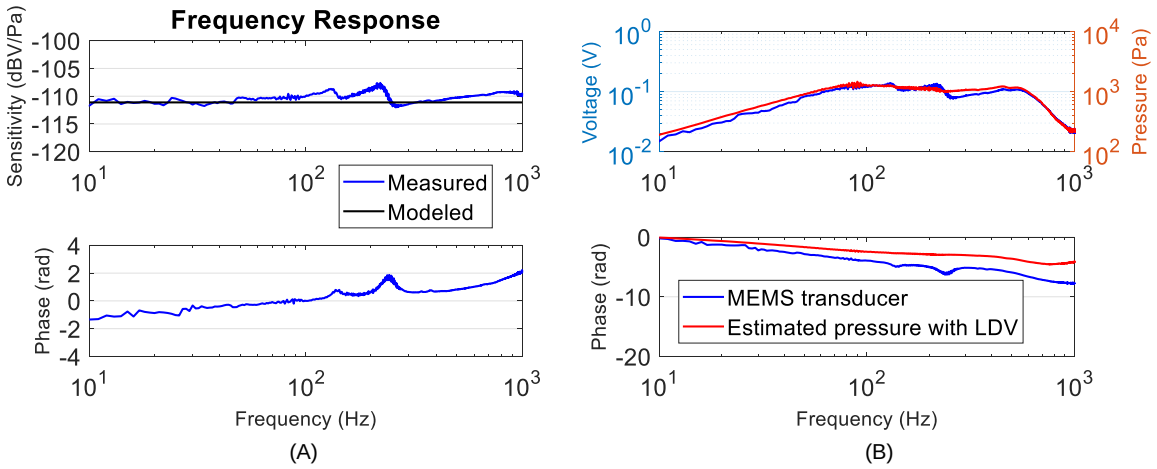

Figure 4.14: In-water sensing test. (A) Frequency response of the MEMS transducer. The modeled sensitivity is the same as in-air sensitivity (-111 dBV/Pa or 2.78 μV/Pa). (B) MEMS transducer voltage output (blue) and estimated pressure using LDV (red).

the transducer should work even below 10 Hz. The measured sensitivity match the modeling expectation very well for in air and in water in 10-1000 Hz. Higher than 1000 Hz in water, the slow wave in the syringe-water coupled structure started to affect the calibration. Around 200 Hz in in-water sensing, there was a resonance which was caused by the cantilevered syringe resonance, leaving an calibration error of $\sim$3 dB.

In-water linearity test at 1kHz was conducted and shown in Figure 4.15. The results showed a good linearity (slope of 2.89 μV/Pa with high $R^2 = 0.999$) within 57-9382 Pa. This pressure range is limited by the output of the shaker and not the dynamic range of the MEMS transducer. Simulation results suggests the diaphragm transducer will be not break within 200 kPa excitation even with a 255 MPa residual stress.

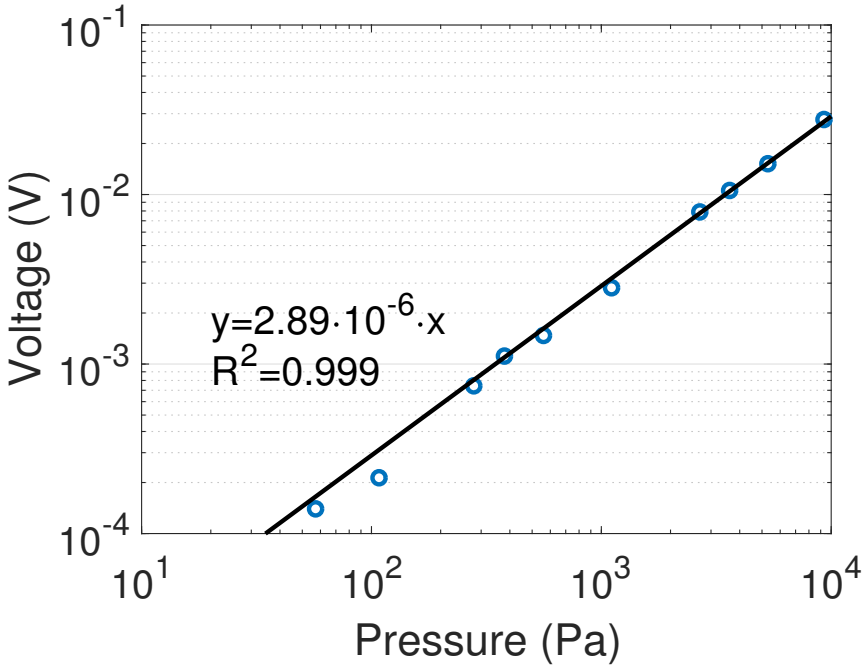

Figure 4.15: In-water linearity test at 1kHz.

4.7 Noise and FOM

The noise was measured by putting the transducer in a metal box (connected to the ground) in the acoustic chamber. The noise spectrum was measured and plotted in Figure 4.16A. The expected tanδ noise was calculated and plotted on the same figure. The measured noise was higher than the expected noise, because the noise was basically from the JFET and the op-amp. The MDP was calculated by dividing the measured noise and the sensitivity, and is shown in Figure 4.16B. At 1 kHz, the MDP is 0.75 mPa, and at 100 Hz, the MDP is 0.24 mPa.

To compare this transducer with other existing piezoelectric diaphragm transducers, a summary of the MDP at 100 Hz and the area of this transducer is shown in Figure 4.17A. Compared to other transducers [104, 114, 46, 106], this work (red cross) uses a much smaller diaphragm area to produce a slightly higher MDP at 100 Hz, due to poor AlN film quality. With a better AlN film quality, the performance of the unimorph diaphragm ring design transducers can achieve the design limit (blue cross),

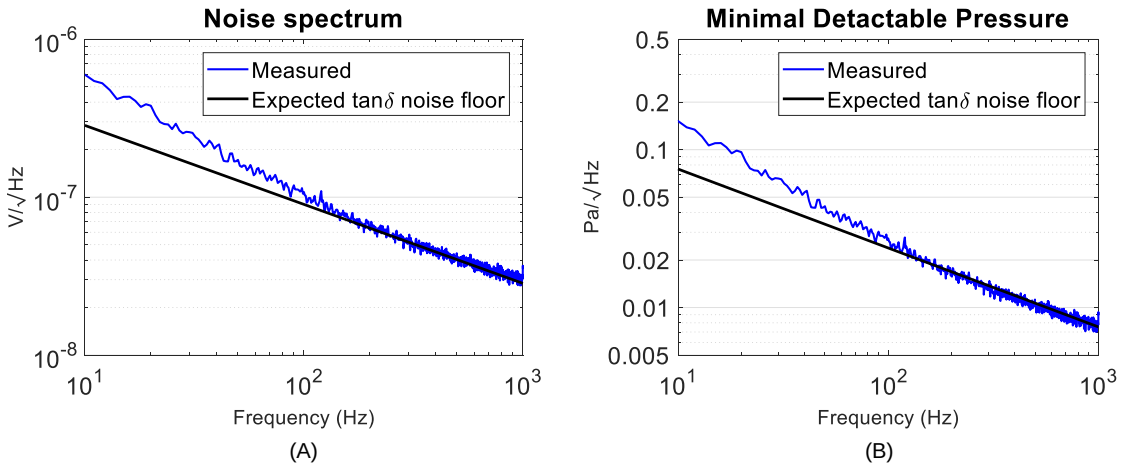

Figure 4.16: Measured and modeled noise spectrum. (A) Noise spectrum. (B) Minimal detectable pressure.

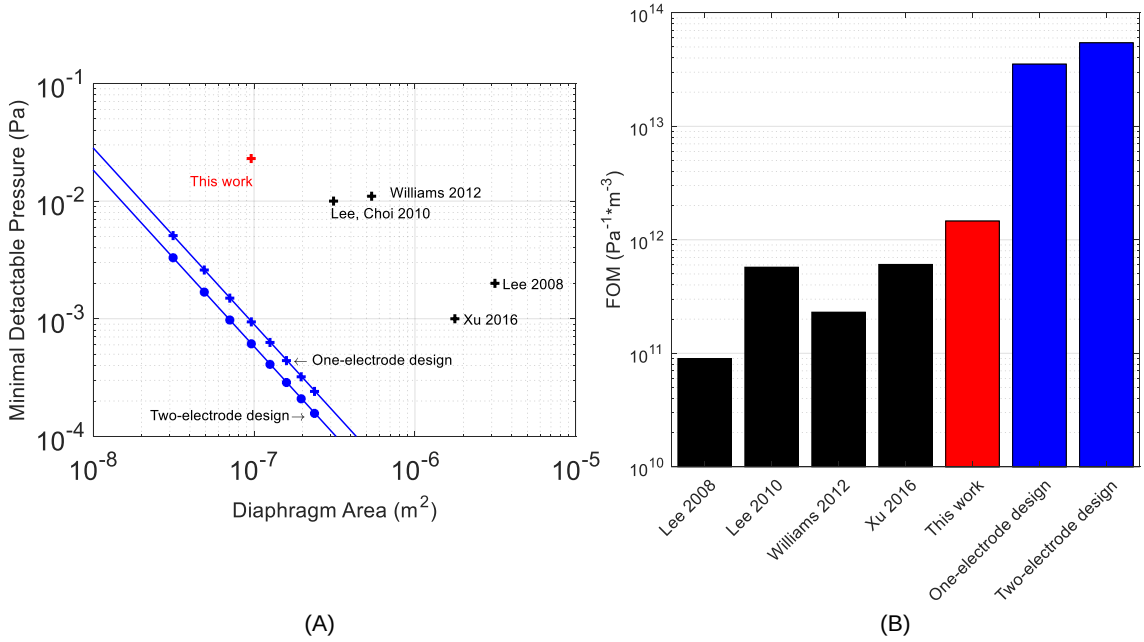

Figure 4.17: MDP and FOM for the piezoelectric diaphragm sensors, estimated at 100Hz. (A) MDP for the piezoelectric diaphragm sensors, estimated at 100 Hz. (B)Figure of Merit (FOM = $\frac{1}{\text{MDP}\cdot\text{Area}^{1.5}}$)

calculated by FEA model under no residual stress, and a d_{31} = -2.51 pm/V from Xu et al. [106]. The design limit follows a blue trend line, which is proportional to the Diaphragm Area$^{-1.5}$. This is because MDP is proportional to $C_{ad}^{-\frac{1}{2}}$ (from Equation 4.2), and C_{ad} is proportional to Diaphragm Area^3. Hence, for a given design, MDP should change proportional to Diaphragm Area$^{-1.5}$. To compare transducers with different diaphragm area fairly, we propose a FOM defined below.

$$\text{FOM} = \frac{1}{\text{MDP} \cdot \text{Area}^{1.5}} \tag{4.3}$$

This FOM provides a useful evaluation metric, especially for the 2D MEMS design when the planar area size requirement is more strict than the thickness of the back cavity. A higher FOM indicates a better design as a sensor.

Figure 4.17 shows a summary of the MPD and the area of this transducer and other existing piezoelectric diaphragm transducers. This work (red cross) is the diaphragm transducer with a radius of 175 μm with 255 MPa residual stress and a low d_{31} = -0.75 pm/V, demonstrated in this chapter. Blue crosses are the design limit of the ring design (one electrode) under no residual stress, a normal d_{31} = -1.75 pm/V and a tanδ = 0.2% discussed in Section 4.2. Blue stars are the design limit of the flipped-polarity (two electrodes) design limit. The design limit can be achieved by depositing a better AlN film to reduce the residual stress and improve d_{31}. Further improvements can also be made on the design limit by increasing the d_{31} and lowering tanδ. Compared to other low noise piezoelectric diaphragm transducers with larger diaphragm areas, this one-electrode design transducer (radius of 175 μm with 255 MPa residual stress and a low d_{31} = -0.75 pm/V) shows a slightly higher minimal detectable pressure at 100 Hz, as shown in Figure 4.17A. However, both one-electrode and two-electrode design limit indicates a lower MDP, which could be easily achieved with a better film quality and less residual stress. The FOM shown in Figure 4.17B

indicates that this 175 μm radius one-electrode design transducer already has a higher FOM than other piezoelectric diaphragm transducers (Lee 2008 [104], Lee 2010 [114], Williams 2012 [46], and Xu 2016 [106]). This is due to we are using AlN unimorph, and AlN is a better sensing material than PZT or ZnO [61]. Xu et al. [106] have similar design using AlN, but our design is better for the following reasons. First, our diaphragm is thinner, which has a larger structural compliance with the same radius, and hence a smaller MDP (MDP is proportional to $C_{ad}^{-\frac{1}{2}}$). Second, we are using a single diaphragm, and Xu et al. is using 25 diaphragms in parallel. As discussed in Section 4.2.2, compared to connecting 25 smaller diaphragms in parallel, it is more efficient to have one larger diaphragm with the same total diaphragm area. Under the same condition (same total diaphragm area, same piezoelectric parameters, and same structural parameters), having one larger diaphragm would produce a MDP that is only 4% of the MDP that would achieved by connecting 25 smaller diaphragms in parallel.

4.8 Discussion

In this chapter, the design, fabrication, and testing of an ultraminiature diaphragm transducer was demonstrated. The transducer works in air and in water with the same sensitivity and for a wide frequency range. This transducer uses a small area to achieve a very low noise floor. It has been demonstrated that this design has a better FOM, compared to other piezoelectric diaphragm acoustic transducers. In addition, this diaphragm sensor has a much smaller IRN while using a smaller diaphragm, compared to the intracochlear acoustic sensors. It can be seen in Fig 4.18 that the diaphragm transducer demonstrated in this section used a much smaller diaphragm area to achieve a much lower IRN. This work provides a promising high performance intracochlear acoustic transducer to make a better completely implantable cochlear implant.

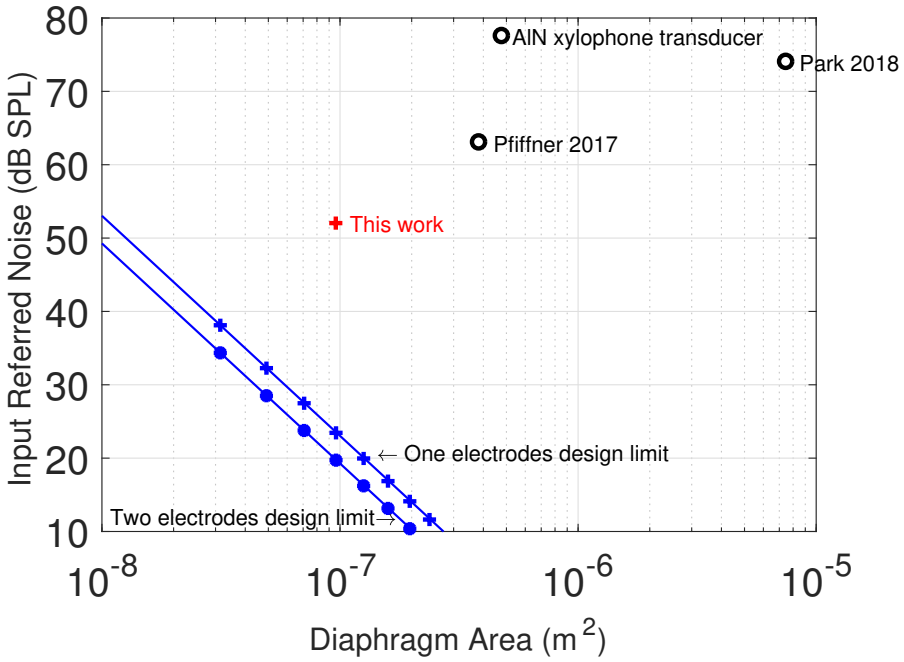

Figure 4.18: IRN for the intracochlear acoustic sensors, estimated at 1 kHz.

The RMS noise in 0-1000 Hz of this diaphragm sensor is 1 Pa, even with the circuit noise in the low frequency range. This noise is lower than the pressure resolution of the existing cardiovascular pressure sensors reported [43, 108, 109, 107, 110]. This sensor is expected to be functional up to at least $\sim$ 200 kPa. Therefore the dynamic range is 1 - 200000 Pa, which is broader than the blood pressure dynamic range ($\sim$ 100-27000 kPa) [107]. Therefore, it could be implemented to a cardiovascular pressure sensing unit to sense the dynamic blood pressure.

This transducer can also be used for other applications including Piezoelectric Micromachined Ultrasonic Transducers (PMUT) [115], micro actuator[80], etc.

4.9 Conclusion

We have designed and fabricated a series of diaphragm transducers with one-electrode and two-electrode designs and varying diaphragm and MEMS die sizes. Also, systematic tests were conducted on a ring design transducer with a radius of

175 μm on a individual MEMS die (size = 400·500·500 μm^3), which verified the design. The frequency bandwith is limited by its resonances (343 kHz acoustical resonance in air, and 133 kHz underwater resonance in water). The sensitivity is -111 dBV/Pa (2.78 μV/Pa) for both in air and in water. The IRN at 1 kHz of this diaphragm transducer is 52 dB SPL, which is less than the existing intracochlear acoustic sensors [25, 26] while using a smaller diaphragm area. The MDP at 100 Hz of this ring design 175 μm sensor is slightly higher than the existing piezoelectric diaphragm acoustic sensors [104, 114, 46] due to high residual stress and low d_{31}, but improvements can be made to achieve a MDP lower than these sensors [104, 114, 46] by having a better AlN film quality. The figure-of-merit MDP·$\text{Area}^{1.5}$ of this work is lower than other piezoelectric diaphragm acoustic sensors [104, 114, 46]. Due to the small size, large frequency bandwith, low noise, and high dynamic range, this sensor meet all the requirements for cardiovascular pressure sensing applications and potentially other biomedical dynamic pressure sensing applications [107].

CHAPTER V

Conclusions and Future Work

5.1 Summary

This thesis presents the ultraminiature acoustic transducers developed for biomedical applications like hearing and cardiovascular applications. An FEA model is developed to design and understand the frequency behavior of the the acoustic transducers. Two generations of devices are designed and fabricated. The first generation device is a xylophone transducer with a flexible parylene-gold cable connection. Benchtop actuation and sensing tests confirmed the functionality for both in air and in water. The xylophone transducer is further coated with Al_2O_3 and parylene and implanted in a living cochlea of a guinea pig to sense the local intracochlear acoustic pressure. The second generation device is a diaphragm AlN unimorph with an encapsulated back cavity. Details of the contributions are summarized as below.

5.2 Contributions

The contributions of this thesis are mainly aimed to developing ultraminiature acoustic transducers for implantable hearing and cardiovascular devices. This thesis presents a systematic way to design, model, fabricate and test the ultraminiature piezoelectric acoustic transducers. Firstly, a full 3D FEA model was built to study

and analyze the frequency behavior of the cantilever transducer both in air and in water. Secondly, a two-wafer MEMS process was used to fabricate the xylophone transducer with flexible cable connection. Thirdly, the *in vivo* test was conducted with the transducer implanted inside a living guinea pig's cochlea, which demonstrated the functionality of using the transducer as a sensor for the fully implantable cochlear implants. Finally, a second generation (ultraminiature diaphragm transducer) was designed, fabricated, and tested. Compared with the first generation transducer, this diaphragm transducer had a much higher sensitivity, especially in the low frequency range. Hence, cardiovascular applications, which focus more on low frequency signals, were also investigated. This diaphragm transducer was smaller than the xylophone transducer/PIAT and other existing piezoelectric diaphragm sensors, more importantly, it was designed to have the smallest MDP. More details about the contributions of this thesis have been summarized below.

1. Fabricated a xylophone transducer with flexible cable connection using a two-wafer process
    - The two-wafer process increased the yield and reduced the fabrication time
    - The wire-epoxy bonding technique was developed to bond the transducer and the flexible cable connection, which were fabricated separately
2. Developed an FEA model to study the frequency behavior for the piezoelectric cantilever transducer in a viscous fluid media (air and water)
    - The model can accurately predict the frequency response of the transducer both in air and in water
3. Piezoelectric voltage output in response to external acoustic stimuli was measured with the PIAT implanted inside a living cochlea of a guinea pig

- The measured voltage amplitude had clear peaks near the resonances under fluid loading
- The voltage amplitude were linear regarding the input sound pressure level
- The phase indicated clear acoustic delay

4. The second generation devices (ultraminiature diaphragm transducers) were designed, fabricated, and tested
    - A 2D axial-symmetric FEA model was built to design the transducer
    - The designed transducer was smaller in size, but it had higher sensitivity and lower input referred noise compared to the first generation xylophone transducer and other existing piezoelectric diaphragm transducers
    - The application for cardiovascular sound sensor application was investigated
    - The diaphragm transducers were fabricated and tested
    - The model and design were validated experimentally

5.3 Future Work

Further improvements on the transducer performance can be done by using a AlN bimorph, instead of a unimorph. In this way, the MDP can be even lowered by 3 dB. A better quality AlN can be deposited to increase the d_{31} and decrease the residual stress, which are the current major issues that limits the current batch, as demonstrated in the previous chapter. In addition, scandium (Sc) can be doped in the AlN to create AlScN film to even increase the piezoelectric coefficients [116]. Future work should also be focusing on using this high performance diaphragm acoustic transducer for a variety of applications. The application-specific integrated circuit (ASIC) can be developed to buffer and amplify the signal. Some bonding or packaging

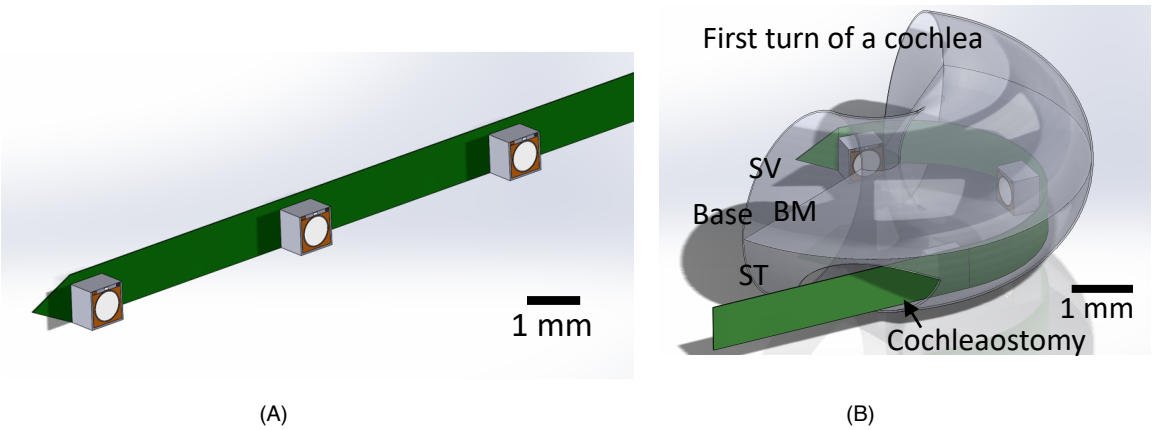

Figure 5.1: Ultraminiature Acoustic Transducer Array on a fPCB.

might be necessary depending on the applications. Both acute and chronic *in vivo* animal tests can be conducted.

An intracochlear microphone can be developed using this ultraminiature acoustic transducer. An array of this ultraminiature transducers can be mounted and wire-bonded on a flexible printed circuit board (fPCB), as shown in Figure 5.1 (A). The ASIC can be implemented on the fPCB to buffer and amplify the sensed signals. This fPCB is stiff enough to maintain its shape during insertion, and flexible enough to be able to curve once it hits the constraint of the cochlea or blood vessel. Figure 5.1 (B) shows an example of using this transducer array on a fPCB for use as a intracochlear microphone while implanted in the scala tympani ST through a cochleaostomy.

A completely implantable cochlear implant (CICI) can be developed by printing the intracochlear electrodes on this fPCB using biocompatible metal. In this way, the intracochlear acoustic pressure can be sensed by ultraminiature acoustic transducer array in the ST, and then the sensed electrical signals can be buffered and processed through a processor outside the cochlea and send it back to the intracochlear electrodes array on the fPCB. An intracardiac dynamic pressure sensor can be developed by using the same principal as the intracochlear microphone. Silicone might be used to coat the diaphragm to increase the robustness. Additional packaging can also be

implemented to protect the electronics. After the packaging, *in vivo* test can be done by using a dog model [44].

BIBLIOGRAPHY

BIBLIOGRAPHY

[1] John Borwick. *Loudspeaker and headphone handbook*. CRC Press, 2012.

[2] G. M. Sessler. Acoustic sensors. *Sensors and Actuators: A. Physical*, 26(1-3):323–330, 1991.

[3] P. R. Scheeper, A. G.H. van der Donk, W. Olthuis, and P. Bergveld. A review of silicon microphones. *Sensors and Actuators: A. Physical*, 1994.

[4] Karl Grosh and Robert J. Littrell. Piezoelectric MEMS microphone. *U.S. Patent*, page No. 8896184, 2014.

[5] Yuan Wu Jiang, Dan Ping Xu, and Sang Moon Hwang. Electromagnetic-Mechanical Analysis of a Balanced Armature Receiver by Considering the Nonlinear Parameters as a Function of Displacement and Current. *IEEE Transactions on Magnetics*, 99:1–4, 2018.

[6] Bolajoko O Olusanya, Katrin J Neumann, and James E Saunders. The global burden of disabling hearing impairment: a call to action. *Bulletin of the World Health Organization*, 92(5):367–373, 5 2014.

[7] F G Zeng, S Rebscher, W Harrison, X Sun, and H Feng. Cochlear implants: system design, integration, and evaluation. *IEEE Reviews in Biomedical Engineering*, 1:115–142, 2008.

[8] T Francart and H McDermott. Psychophysics, fitting, and signal processing for combined hearing aid and cochlear implant stimulation. *Ear and Hearing*, 34(6):685–700, 2013.

[9] M Yip, Jin Rui, H H Nakajima, K M Stankovic, and A P Chandrakasan. A fully-implantable cochlear implant SoC with piezoelectric middle-ear sensor and arbitrary waveform neural stimulation. *Solid-State Circuits, IEEE Journal of*, 50(1):214–229, 2015.

[10] Fan-Gang Zeng. Cochlear implants: why don't more people use them? *The Hearing Journal*, 60(3):48–49, 2007.

[11] M Bachman, F G Zeng, T Xu, and G P Li. Micromechanical resonator array for an implantable bionic ear. *Audiology and Neurotology*, 11:95–103, 2006.

[12] H P Zenner and H Leysieffer. Total implantation of the implex TICA hearing amplifier implant for high frequency sensorineural hearing loss: the Tubingen University experience. *Otolaryngologic clinics of North America*, 2001.

[13] Luca Bruschini, Francesca Forli, Susanna Passetti, Paolo Bruschini, and Stefano Berrettini. Fully implantable otologics MET Carina device for the treatment of sensorineural and mixed hearing loss: audio-otological results. *Acta Oto-Laryngologica*, 130(10):1147–1153, 10 2010.

[14] Janaina Oliveira Bentivi Pulcherio, Aline Gomes Bittencourt, Patrick Rademaker Burke, Rafael Da Costa Monsanto, Rubens De Brito, Robinson Koji Tsuji, and Ricardo Ferreira Bento. Carina® and Esteem®: A systematic review of fully implantable hearing devices. *PLoS ONE*, 2014.

[15] Robert J S Briggs, Helmut C Eder, Peter M Seligman, Robert S C Cowan, Kerrie L Plant, James Dalton, David K Money, James F Patrick, J Patrick., and James F Patrick. Initial clinical experience with a totally implantable cochlear implant research device. *Otology & Neurotology*, 29(2)(2):114–119, 2008.

[16] David S. Haynes, Jadrien A. Young, George B. Wanna, and Michael E. Glasscock. Middle ear implantable hearing devices: an overview. *Trends in Amplification*, 2009.

[17] J. M. Gerard, M. P. Thill, G. Chantrain, M. Gersdorff, and N. Deggouj. Esteem 2 middle ear implant: our experience. *Audiology and Neurotology*, 2012.

[18] Seong Tak Woo, Dong Ho Shin, Hyung Gyu Lim, Ki Woong Seong, Peter Gottlieb, Sunil Puria, Kyu Yup Lee, and Jin Ho Cho. A new trans-tympanic microphone approach for fully implantable hearing devices. *Sensors*, 15(9):22798–22810, 2015.

[19] H Leysieffer, J W Baumann, R Mayer, D Muller, G Muller, T Schon, A Volz, and H P Zenner. [A totally implantable hearing aid for inner ear deafness: TICA LZ 3001]. *Ein vollstandig implantierbares Horsystem fur Innenohrschwerhorige: TICA LZ 3001.*, 1998.

[20] Elizabeth S Olson. Observing middle and inner ear mechanics with novel intracochlear pressure sensors. *The Journal of the Acoustical Society of America*, 103(6):3445–3463, 1998.

[21] Elizabeth S Olson. Direct measurement of intra-cochlear pressure waves. *Nature*, 402(6761):526–529, 12 1999.

[22] E S Olson. Intracochlear pressure measurements related to cochlear tuning. *J. Acoust. Soc. Am*, 110(1)(March 2001):349–367, 2001.

[23] A Dancer and R Franke. Intracochlear sound pressure measurements in guinea pigs. *Hearing Research*, 2:191–205, 1980.

[24] Francis (Pete) X. Creighton, Xiying Guan, Steve Park, Ioannis (John) Kymissis, Hideko Heidi Nakajima, and Elizabeth S. Olson. An Intracochlear Pressure Sensor as a Microphone for a Fully Implantable Cochlear Implant. *Otology & Neurotology*, 37(10):15961600, 2016.

[25] Flurin Pfiffner, Lukas Prochazka, Dominik Peus, Ivo Dobrev, Adrian Dalbert, Jae Hoon Sim, Rahel Kesterke, Joris Walraevens, Francesca Harris, Christof Roosli, Dominik Obrist, and Alexander Huber. A MEMS condenser microphone-based intracochlear acoustic receiver. *IEEE Transactions on Biomedical Engineering*, 64(10):2431–2438, 2017.

[26] Steve Park, Xiying Guan, Youngwan Kim, Francis Pete X Creighton, Eric Wei, Ioannis John Kymissis, Hideko Heidi Nakajima, and Elizabeth S Olson. PVDF-based piezoelectric microphone for sound detection inside the cochlea : toward totally implantable cochlear implants. *Trends in Hearing*, 22:1–11, 2018.

[27] W Hemmert, U Durig, M Despont, U Drechsler, G Genolet, P Vettiger, and D M Freeman. A life-sized hydromechanical, micromechanical inner ear. *Biophysics of the Cochlea: From Molecules to Models.*, pages 409–416, 2003.

[28] F Chen, H I Cohen, T G Bifano, J Castle, J Fortin, C Kapusta, D C Mountain, A Zosuls, and A E Hubbard. A hydromechanical biomimetic cochlea: experiments and models. *J. Acoust. Soc. Am*, 119(1):394–405, 2006.

[29] M J Wittbrodt, C R Steele, and S Puria. Developing a physical model of the human cochlea using microfabrication methods. *Audiology and Neurotology*, 11:104–112, 2006.

[30] R White and K Grosh. Microengineered hydromechanical cochlear model. *Proc. National Academy of Sciences*, 102(5):1296–1301, 2005.

[31] H Shintaku, T Nakagawa, D Kitagawa, H Tanujaya, S Kawano, and J Ito. Development of a piezoelectric acoustic sensor with frequency selectivity for artificial cochlea. *Sensors Actuators A*, 158:183–192, 2010.

[32] T Inaoka, H Shintaku, T Nakagawa, S Kawano, H Ogita, T Sakamoto, S Hamanishi, H Wada, and J Ito. Piezoelectric materials mimic the function of the cochlear sensory epithelium. *Proceedings of the National Academy of Sciences*, 108(45):18390–18395, 2011.

[33] D Haronian and N MacDonald. A microelectromechancis based artificial cochlea (MEMBAC). *IEEE Transducers*, pages 708–711, 1995.

[34] S Ando, K Tanaka, and M Abe. Fishbone architecture: an equivalent mechanical model of cochlea and its application to sensors and actuators. *IEEE Transducers*, pages 1027–1030, 1997.

[35] S Hur, S Q Lee, and H S Choi. Fabrication and characterization of PMN-PT single crystal cantilever array for cochlear-like acoustic sensor. *Jour. Mech. Sci. Tech.*, 24:181–184, 2010.

[36] Jongmoon Jang, Sangwon Kim, David J Sly, Stephen J Oleary, and Hongsoo Choi. MEMS piezoelectric artificial basilar membrane with passive frequency selectivity for short pulse width signal modulation. *Sensors and Actuators A: Physical*, 203:6–10, 2013.

[37] Jongmoon Jang, JangWoo Lee, Seongyong Woo, David J Sly, Luke J Campbell, Jin-Ho Cho, Stephen J OLeary, Min-Hyun Park, Sungmin Han, Ji-Wong Choi, Jeong Hun Jang, and Hongsoo Choi. A microelectromechanical system artificial basilar membrane based on a piezoelectric cantilever array and its characterization using an animal model. *Scientific Reports*, 5(January):12447, 2015.

[38] Tatsuo Tagawa, Toshiyo Tamura, and P. Ake Oberg. Pressure Measurement. In 2, editor, *Biomedical sensors and instruments*. CRC Press: Boca Raton, FL, 2011.

[39] Anh L Bui, Tamara B Horwich, and Gregg C Fonarow. Epidemiology and risk profile of heart failure. *Nature reviews. Cardiology*, 8(1):30–41, 2011.

[40] Sven Poeggel, Daniele Tosi, DineshBabu Duraibabu, Gabriel Leen, Deirdre McGrath, and Elfed Lewis. Optical Fibre Pressure Sensors in Medical Applications. *Sensors*, 15(7):17115–17148, 2015.

[41] Koen D. Reesink, Theo Van Der Nagel, Jan Bovelander, J. R C Jansen, Frederik H. Van Der Veen, and Jan J. Schreuder. Feasibility study of a fiber-optic system for invasive blood pressure measurements. *Catheterization and Cardiovascular Interventions*, 57(2):272–276, 2002.

[42] C Pramanik, H Saha, and U Gangopadhyay. Design optimization of a high performance silicon MEMS piezoresistive pressure sensor for biomedical applications. *Journal of Micromechanics and Microengineering*, 16(10):2060–2066, 2006.

[43] Nader Najafi and Achiau Ludomirsky. Initial animal studies of a wireless, batteryless, MEMS implant for cardiovascular applications. *Biomedical Microdevices*, 6(1):61–65, 2004.

[44] Robert L. Hammond, Kenny Hanna, Catherine Morgan, Peter Perakis, Nader Najafi, Graham W. Long, and Charles J. Shanley. A Wireless and Battery-Less Miniature Intracardiac Pressure Sensor. *ASAIO Journal*, 58(1):83–87, 2012.

[45] Chuming Zhao, Katherine E. Knisely, and Karl Grosh. Design and fabrication of a piezoelectric MEMS xylophone transducer with a flexible electrical connection. *Sensors and Actuators A: Physical*, 275:29–36, 2018.

[46] Matthew D. Williams, Benjamin A. Griffin, Tiffany N. Reagan, James R. Underbrink, and Mark Sheplak. An AlN MEMS piezoelectric microphone for aeroacoustic applications. *Journal of Microelectromechanical Systems*, 21(2):270–283, 2012.

[47] Li Peng Wang, Richard A. Wolf, Yu Wang, Ken K. Deng, Lichun Zou, Robert J. Davis, and Susan Trolier-McKinstry. Design, fabrication, and measurement of high-sensitivity piezoelectric microelectromechanical systems accelerometers. *Journal of Microelectromechanical Systems*, 12(4):433–439, 2003.

[48] Sang Choon Ko, Yong Chul Kim, Seung Seob Lee, Seung Ho Choi, and Sang Ryong Kim. Micromachined piezoelectric membrane acoustic device. *Sensors and Actuators, A: Physical*, 103(1-2):130–134, 2003.

[49] D Ozevin, D W Greve, I J Oppenheim, and S P Pessiki. Resonant capacitive MEMS acoustic emission transducers. *Smart Materials and Structures*, 15(6):1863–1871, 2006.

[50] H B Fang, J Q Liu, Z Y Xu, L Dong, L Wang, D Chen, B C Cai, and Y Liu. Fabrication and performance of MEMS-based piezoelectric power generator for vibration energy harvesting. *Microelectronics Journal*, 37:1280–1284, 2006.

[51] Tianying Ren. Longitudinal pattern of basilar membrane vibration in the sensitive cochlea. *Proceedings of the National Academy of Sciences of the United States of America*, 99(26):17101–6, 2002.

[52] Peter Dallos, Arthur N. Popper, and Richard R. Fay. The Cochlea. In *Springer Handbook of Auditory Research Vol. 8*. 1996.

[53] Gene Hou, Jin Wang, and Anita Layton. Numerical Methods for Fluid-Structure Interaction A Review. *Communications in Computational Physics*, 12(2):337–377, 2012.

[54] John Elie Sader. Frequency response of cantilever beams immersed in viscous fluids with applications to the atomic force microscope. *J. Appl. Phys.*, 84(1):64–76, 1998.

[55] T Naik, E K Longmire, and S C Mantell. Dynamic Response of a Cantilever in Liquid Near a Solid Wall. *Sensors Actuators*, 102A:240–254, 2003.

[56] C Vancura, I Dufour, S M Heinrich, F Josse, and A Heirlemann. Analysis of resonanting microcantilevers operating in a viscous liquid environment. *Sensors and Actuators*, A 141:43–51, 2008.

[57] Katherine E Knisely. *The Application of a Piezoelectric MEMS Cantilever Array as a Completely Implantable Cochlear Implant.* PhD thesis, Ph.D. Thesis, The University of Michigan, 2014.

[58] Jinhong Qu, Clark B. Teeple, and Kenn R. Oldham. Modeling Legged Microrobot Locomotion Based on Contact Dynamics and Vibration in Multiple Modes and Axes. *Journal of Vibration and Acoustics*, 139(3):031013, 2017.

[59] Sudipta Basak, Arvind Raman, and Suresh V. Garimella. Hydrodynamic loading of microcantilevers vibrating in viscous fluids. *Journal of Applied Physics*, 99(11), 2006.

[60] Chuming Zhao, Katherine E Knisely, and Karl Grosh. Modeling, fabrication, and testing of a MEMS multichannel AlN transducer for a completely implantable cochlear implant. In *Solid-State Sensors, Actuators and Microsystems (TRANSDUCERS)*, Kaohsiung, 2017.

[61] Robert John Littrell. *High Performance Piezoelectric MEMS Microphones*. PhD thesis, Ph.D. Thesis, The University of Michigan, 2010.

[62] B A Murphy. and Brian A Murphy. *A biocompatibility study of aluminum nitride packaging for cortical implants.* PhD thesis, Wayne State University, 2008.

[63] Yoonho Seo, Daniel Corona, and Neal A. Hall. On the theoretical maximum achievable signal-to-noise ratio (SNR) of piezoelectric microphones. *Sensors and Actuators, A: Physical*, 264:341–346, 2017.

[64] Kristie Brock, Laura Gallaugher, Valerie K. Bergdall, and Robert C. Dysko. *The Laboratory Rabbit, Guinea Pig, Hamster, and Other Rodents*. 2012.

[65] E. Bruce; Goldstein and James Brockmole. *Sensation and Perception*. tenth edit edition, 2016.

[66] COMSOL Inc. COMSOL Multiphysics 5.2a, 2016.

[67] J Meyer, T Stieglitz, O Scholz, W Haberer, and J Beutel. High density interconnects and flexible hybrid assemblies for active biomedical implants. *IEEE Trans. Adv. Packag*, 24(3):366–374, 2001.

[68] Robert Littrell and Karl Grosh. Modeling and characterization of cantilever-based MEMS piezoelectric sensors and actuators. *Journal of Microelectromechanical Systems*, 21(2):406–413, 2012.

[69] K Tsubouchi and N Mikoshiba. Zero-Temperature-Coefficient SAW Devices on AlN Epitaxial Films. *IEEE Trans. Sonics Untrason*, 32:634–644, 1985.

[70] F Martin, P Muralt, M A Dubois, and A Pezous. Thickness Dependence of the Properties of Highly C-Axis Textured {AlN} Thin Films. *J. Va. Sci. Technol A*, 22:361–365, 2004.

[71] F Martin, P Muralt, and M A Dubois. Process Optimization for the Sputter Deposition of Molybdenum Thin Films as Electrode for AlN Thin Films. *J. Vac. Sci. Technol A*, 24:946–952, 2006.

[72] Joseph C Doll, Bryan C Petzold, Biju Ninan, Ravi Mullapudi, Beth L Pruitt, Ravi Mullapudi And, and Beth L Pruitt1. Aluminum nitride on titanium for CMOS compatible piezoelectric transducers. *Journal of Micromechanics and Microengineering*, 20(2):025008, 2009.

[73] Meng Zhang, Jian Yang, Chaowei Si, Guowei Han, Yongmei Zhao, and Jin Ning. Research on the piezoelectric properties of AlN thin films for MEMS applications. *Micromachines*, 6(9):1236–1248, 2015.

[74] Katherine Knisely, Chuming Zhao, and Karl Grosh. A MEMS AlN transducer array with flexible interconnections for use as a cochlear implant. In *Proceedings of the 12th International Workshop on the Mechanics of Hearing*, page Vol. 1703. No. 1, 2015.

[75] Chuming Zhao, Katherine E. Knisely, Deborah. J. Colesa, Bryan. E. Pfingst, Yehoash Raphael, and Karl. Grosh. Intracochlear sound sensor-electrode system for fully implantable cochlear implant. In *The Journal of the Acoustical Society of America*, pages 3377–3377, 2016.

[76] Angelique C. Johnson and Kensall D. Wise. An active thin-film cochlear electrode array with monolithic backing and curl. *Journal of Microelectromechanical Systems*, 23(2):428–437, 2014.

[77] John P Seymour, Fan Wu, Kensall D Wise, and Euisik Yoon. State-of-the-art MEMS and microsystem tools for brain research. *Microsystems & Nanoengineering*, 3:16066, 2017.

[78] K D Wise, P T Bhatti, J Wanga, and C R Friedrich. High-density cochlear implants with position sensing and control. *Hearing Research*, 242:22–30, 2008.

[79] Chuan Luo, G.Z. Cao, and I.Y. Shen. Development of a lead-zirconate-titanate (PZT) thin-film microactuator probe for intracochlear applications. *Sensors and Actuators A: Physical*, 201:1–9, 2013.

[80] C. Luo, I. Omelchenko, R. Manson, C. Robbins, E. C. Oesterle, G. Z. Cao, I. Y. Shen, and C. R. Hume. Direct intracochlear acoustic stimulation using a PZT microactuator. *Trends in Hearing*, 19(0):1–14, 2015.

[81] Xiaochen Zhao, Gongmin Liu, Chuming Zhao, and Karl Grosh. Broadband noise attenuation using a variable locally reacting impedance. *The Journal of the Acoustical Society of America*, 141(1):147–158, 2017.

[82] Xiaochen Zhao, Karl Grosh, Gongmin Liu, and Chuming Zhao. Experimental study of broadband noise attenuation using variable locally reacting impedance. In *INTER-NOISE and NOISE-CON Congress and Conference Proceedings*, volume 255, pages 4029–4038, Hong Kong, 2017. Institute of Noise Control Engineering.

[83] Alison Hake, Chuming Zhao, and Karl Grosh. Miniature accelerometers for sensing middle ear motion. In *The Journal of the Acoustical Society of America*, pages 4016–4016, 2017.

[84] Alison Hake, Chuming Zhao, Wang-Kyung Sung, and Karl Grosh. Experimental assessment of miniature accelerometers designed for sensing middle ear motion. In *The Journal of the Acoustical Society of America*, pages 1804–1804, Minneapolis, MN, 2018.

[85] Ioanna G. Mina, Hyunsoo Kim, Insoo Kim, Sung Kyu Park, Kyusun Choi, Thomas N. Jackson, Richard L. Tutwiler, and Susan Trolier-McKinstry. High frequency piezoelectric MEMS ultrasound transducers. In *IEEE Transactions on Ultrasonics, Ferroelectrics, and Frequency Control*, volume 54, pages 2422–2429, 2007.

[86] Rashed Mahameed, Nipun Sinha, Marcelo B Pisani, and Gianluca Piazza. Dual-beam actuation of piezoelectric AlN RF MEMS switches monolithically integrated with AlN contour-mode resonators. *J Micromech. Microeng.*, 18(10):1–11, 2008.

[87] Katherine Knisely and Karl Grosh. A MEMS AlN transducer array for use as a cochlear implant. *2013 Joint IEEE International Symposium on Applications of Ferroelectric and Workshop on Piezoresponse Force Microscopy, ISAF/PFM 2013*, 100004(2015):240–243, 2013.

[88] Xianzong Xie, Loren Rieth, Ryan Caldwell, Mohit Diwekar, Prashant Tathireddy, Rohit Ritu Sharma, and Florian Solzbacher. Long-term bilayer encapsulation performance of atomic layer deposited Al2O3 and parylene c for biomedical implantable devices. *IEEE Transactions on Biomedical Engineering*, 60(10):2943–2951, 2013.

[89] Xianzong Xie, Loren Rieth, Layne Williams, Sandeep Negi, Rajmohan Bhandari, Ryan Caldwell, Rohit Sharma, Prashant Tathireddy, and Florian Solzbacher. Long-term reliability of Al2O3 and parylene C bilayer encapsulated Utah electrode array based neural interfaces for chronic implantation. *Journal of neural engineering*, 11(2):026016, 2014.

[90] Anders Fridberger, Jacques Boutet De Monvel, Jiefu Zheng, Ning Hu, Yuan Zou, Tianying Ren, and Alfred Nuttall. Organ of Corti potentials and the motion of the basilar membrane. *The Journal of Neuroscience*, 24(45):10057–10063, 2004.

[91] Nils D. Hoivik, Jeffrey W. Elam, Ryan J. Linderman, Victor M. Bright, Steven M. George, and Y. C. Lee. Atomic layer deposited protective coatings for micro-electromechanical systems. *Sensors and Actuators, A: Physical*, 103(1-2):100–108, 2003.

[92] David C. Miller, Ross R. Foster, Shih-Hui Jen, Jacob a. Bertrand, Shawn J. Cunningham, Arthur S. Morris, Yung-Cheng Lee, Steven M. George, and Martin L. Dunn. Thermo-mechanical properties of alumina films created using the atomic layer deposition technique. *Sensors and Actuators A: Physical*, 164(1-2):58–67, 2010.

[93] B. Ilic, S. Krylov, and H. G. Craighead. Young's modulus and density measurements of thin atomic layer deposited films using resonant nanomechanics. *Journal of Applied Physics*, 108(4), 2010.

[94] Oili M E Ylivaara, Xuwen Liu, Lauri Kilpi, Jussi Lyytinen, Dieter Schneider, Mikko Laitinen, Jaakko Julin, Saima Ali, Sakari Sintonen, Maria Berdova, Eero Haimi, Timo Sajavaara, Helena Ronkainen, Harri Lipsanen, Jari Koskinen, Simo Pekka Hannula, and Riikka L. Puurunen. Aluminum oxide from trimethylaluminum and water by atomic layer deposition: The temperature dependence of residual stress, elastic modulus, hardness and adhesion. *Thin Solid Films*, 552:124–135, 2014.

[95] Luis Robles and Mario A Ruggero. Mechanics of the mammalian cochlea. *Physiol. Rev.*, 81(3)(3):1305–1352, 2001.

[96] Sushrut S. Kale and Elizabeth S. Olson. Intracochlear Scala Media Pressure Measurement: Implications for Models of Cochlear Mechanics. *Biophysical Journal*, 109(12):2678–2688, 2015.

[97] Hideko Heidi Nakajima, Wei Dong, Elizabeth S. Olson, Saumil N. Merchant, Michael E. Ravicz, and John J. Rosowski. Differential intracochlear sound pressure measurements in normal human temporal bones. *J Assoc Res Otolaryngol*, 10(1):23–36, 2016.

[98] N Mukherjee and R D Roseman. Considerations in the development of a piezoelectric transducer cochlear implant. *Mat. Res. Soc. Symp. Proc.*, 604:79–84, 2000.

[99] Martin Grosshomichen, Rolf Salcher, Hans-heinrich Heinrich Kreipe, Thomas Lenarz, Hannes Maier, Martin Grossöhmichen, Rolf Salcher, Hans-heinrich Heinrich Kreipe, Thomas Lenarz, and Hannes Maier. The Codacs direct acoustic cochlear implant actuator: Exploring alternative stimulation sites and their stimulation efficiency. *PLoS ONE*, 10(3):1–20, 2015.

[100] Sebastian P. Schraven, Robert Mlynski, Ernst Dalhoff, Daniela Wildenstein, Balint Alkonyi, Anthony W. Gummer, and Rudolf Hagen. Vibro-EAS: a proposal for electroacoustic stimulation. *Otology & Neurotology*, 36(October):22–27, 2014.

[101] Tianying Ren, Wenxuan He, and Peter G. Barr-Gillespie. Reverse transduction measured in the living cochlea by low-coherence heterodyne interferometry. *Nature Communications*, 7:10282, 2016.

[102] Hee Yoon Lee, Patrick D. Raphael, Jesung Park, Audrey K. Ellerbee, Brian E. Applegate, and John S. Oghalai. Noninvasive in vivo imaging reveals differences between tectorial membrane and basilar membrane traveling waves in the mouse cochlea. *Proceedings of the National Academy of Sciences*, 112(10):3128–3133, 2015.

[103] W He and T Ren. Basilar membrane vibration is not involved in the reverse propagation of otoacoustic emissions. *Scientific reports*, 3:1874, 2013.

[104] Woon Seob Lee and Seung S. Lee. Piezoelectric microphone built on circular diaphragm. *Sensors and Actuators, A: Physical*, 144(2):367–373, 2008.

[105] Sungjoon Choi, Haksue Lee, and Wonkyu Moon. A micro-machined piezoelectric hydrophone with hydrostatically balanced air backing. *Sensors and Actuators, A: Physical*, 158(1):60–71, 2010.

[106] Jinghui Xu, Xiaolin Zhang, Sanchitha N. Fernando, Kevin Tshunchuan Chai, and Yuandong Gu. AlN-on-SOI platform-based micro-machined hydrophone. *Applied Physics Letters*, 109(3):3–8, 2016.

[107] Lawrence Yu, Brian J Kim, and Ellis Meng. Chronically Implanted Pressure Sensors: Challenges and State of the Field. *Sensors*, 14(11):20620–20644, 2014.

[108] H. Fassbender, W. Mokwa, M. Görtz, K. Trieu, U. Urban, T. Schmitz-Rode, T. Göttsche, and P. Osypka. Fully implantable blood pressure sensor for hypertonic patients. *Proceedings of IEEE Sensors*, pages 1226–1229, 2008.

[109] Nina J. Cleven, Jutta A. Müntjes, Holger Fassbender, Ute Urban, Michael Görtz, Holger Vogt, Maik Gräfe, Thorsten Göttsche, Tobias Penzkofer, Thomas Schmitz-Rode, and Wilfried Mokwa. A novel fully implantable wireless sensor system for monitoring hypertension patients. *IEEE Transactions on Biomedical Engineering*, 59(12 PART2):3124–3130, 2012.

[110] P. Shasha Liu and Hung Fat Tse. Implantable sensors for heart failure monitoring. *Journal of Arrhythmia*, 29(6):314–319, 2013.

[111] Matthew D. Williams. *Development of a MEMS Piezoelectric Microphone for Aeroacoustic Application*. PhD thesis, University of Florida, 2011.

[112] Chuming Zhao, Alison Hake, Wang-Kyung Sung, and Karl Grosh. Miniature implantable low noise piezoelectric diaphragm sound sensor. In *The Journal of the Acoustical Society of America*, pages 1804–1804, Minneapolis, MN, 2018.

[113] F. Schloss and M. Strasberg. Hydrophone calibration in a vibrating column of liquid. *Journal of the Acoustical Society of America*, 34(7):958–960, 1962.

[114] Haksue Lee, Sungjoon Choi, and Wonkyu Moon. A micro-machined piezoelectric flexural-mode hydrophone with air backing: Benefit of air backing for enhancing sensitivity. *The Journal of the Acoustical Society of America*, 128(3):1033, 2010.

[115] Xiaoyue Jiang, Yipeng Lu, Hao-Yen Tang, Julius M. Tsai, Eldwin J. Ng, Michael J. Daneman, Bernhard E. Boser, and David A. Horsley. Monolithic ultrasound fingerprint sensor. *Microsystems & Nanoengineering*, 3(May):17059, 2017.

[116] Wenbo Wang, Patrick M. Mayrhofer, Xingli He, Manuel Gillinger, Zhi Ye, Xiaozhi Wang, Achim Bittner, Ulrich Schmid, and J. K. Luo. High performance AlScN thin film based surface acoustic wave devices with large electromechanical coupling coefficient. *Applied Physics Letters*, 105(13), 2014.